# Search for Bosonic Stop Decays
# in $R$-Parity Violating Supersymmetry
# in $e^+p$ Collisions at HERA

vorgelegt von

Diplom–Physikerin
Anja Vest

aus Mönchengladbach

# Abstract

A search for scalar top quarks in $R$–parity violating supersymmetry is performed in $e^+p$ collisions at HERA using the H1 detector. The data, taken at $\sqrt{s} = 319\,\text{GeV}$ and $\sqrt{s} = 301\,\text{GeV}$, correspond to an integrated luminosity of $106\,\text{pb}^{-1}$. The resonant production of scalar top quarks, $\tilde{t}$, in positron quark fusion via an $R$–Parity violating Yukawa coupling $\lambda'$ is considered with the subsequent bosonic stop decay $\tilde{t} \to \tilde{b}W$. The $R$–parity violating decay of the sbottom quark $\tilde{b} \to d\bar{\nu}_e$ and leptonic and hadronic $W$ decays are considered. No evidence for stop production is found in the search for bosonic stop decays nor in a search for the direct $R$–parity violating decay $\tilde{t} \to eq$. Mass dependent limits on $\lambda'$ are obtained in the framework of the Minimal Supersymmetric Standard Model. Stop quarks with masses up to $275\,\text{GeV}$ can be excluded at the $95\%$ confidence level for a Yukawa coupling of electromagnetic strength.

# Kurzzusammenfassung

In $e^+p$ Kollisionen bei HERA werden mit dem H1 Detektor skalare Top Quarks in $R$–paritätsverletzender Supersymmetrie gesucht. Die Daten, die mit einer Schwerpunktsenergie von $301\,\text{GeV}$ und $319\,\text{GeV}$ aufgezeichnet wurden, korrespondieren zu einer integrierten Luminosität von $106\,\text{pb}^{-1}$. In der Positron Quark Fusion wird die resonante Produktion von skalaren Top Quarks über die $R$–paritätsverletzende Yukawa Kopplung $\lambda'$ mit dem anschließenden bosonischen Zerfall des Stop Quarks untersucht, $\tilde{t} \to \tilde{b}W^+$. Unter Berücksichtigung des $R$–paritätsverletzenden Zerfalls des Sbottom Quarks $\tilde{b} \to d\bar{\nu}_e$ werden leptonische und hadronische $W$ Boson Zerfälle analysiert. Weder im bosonischen Stop Zerfall noch im direkten $R$–paritätsverletzenden Zerfall $\tilde{t} \to eq$ ist ein eindeutiger Hinweis auf eine Stop Produktion beobachtbar. Im Rahmen des minimal supersymmetrischen Standardmodells werden deshalb massenabhängige Ausschlussgrenzen auf $\lambda'$ bestimmt. Stop Quarks mit Massen bis $275\,\text{GeV}$ können für eine Yukawa Kopplung elektromagnetischer Stärke mit $95\%$ Confidence Level ausgeschlossen werden.

# Contents

# 1
# Introduction

The Standard Model (SM) of particle physics describes the structure of matter and has been confirmed in numerous experiments in the past decades. Within this theoretical framework, three of the four fundamental forces are unified: the electromagnetic, the weak and the strong interaction. Nevertheless, the Standard Model cannot explain among other things the nature of gravity, the unification of forces and the hierarchy between the electroweak and the gravity scale. Thus, the SM is assumed to be an effective low–energy theory of a superior and more fundamental theory. One of the diverse extensions of the SM is the concept of supersymmetry (SUSY) which comprises several models and scenarios. This symmetry fundamentally connects fermions and bosons by assigning a new supersymmetric particle as a partner to each SM particle. Such particles have not been discovered so far – likely because they might occur at the $\mathcal{O}(\text{TeV})$ scale – although they have been searched for for about twenty years.

One essential quantum number in supersymmetric models is the $R$–parity $R_P$ which ensures lepton number and baryon number conservation. The most general supersymmetric theory is $R_P$ violating. However, in most searches for SUSY particles performed at colliders it is assumed that $R_P$ is conserved. No significant deviation from the SM has been observed in these searches. Therefore, lower limits on the SUSY particles masses have been derived. The most stringent results from LEP and Tevatron allude that presumably no SUSY particle is lighter than the $Z^0$ boson.

Supersymmetric models in which $R$–parity violation ($\not{R}_p$) is allowed are even more interesting since lepton number violation has become attractive, supported by the observation of neutrino mixing and masses [1, 2, 3]. Moreover, with $\not{R}_p$ it is possible to produce resonantly single SUSY particles at colliders. Hence, deep inelastic collisions at HERA[1] are ideally suited to the search for squarks, the scalar supersymmetric partners of quarks, which couple to an electron[2]–quark

---

[1]Hadron–Elektron–Ring–Anlage
[2]In the following, the term *electron* refers to both electrons and positrons, if not otherwise stated.

pair. In most SUSY scenarios, the squarks of the third generation, stop ($\tilde{t}$) and sbottom ($\tilde{b}$), are the lightest squarks.

In the present analysis, a search is presented for stop quarks which are produced resonantly, $e^+q \rightarrow \tilde{t}$. Under the assumption that the sbottom mass is smaller than the stop mass, $M_{\tilde{b}} < M_{\tilde{t}}$, the bosonic decay $\tilde{t} \rightarrow \tilde{b}W$ is investigated. The subsequent sbottom decay into SM particles, $\tilde{b} \rightarrow \bar{\nu}_e d$, is also $R$–parity violating. This particular SUSY scenario is complementary to previous $\not{R}_p$ SUSY searches in squark production by H1 [4,5] and the decay mode is experimentally investigated for the first time. The analysis includes both leptonic and hadronic $W$ decays. A scenario is investigated, in which decays of the light squarks into neutralinos and charginos are kinematically not possible. In order to cover all decay modes, the direct $\not{R}_p$ decay $\tilde{t} \rightarrow e^+d$ is also considered. At HERA, stop quarks with masses close to the kinematic limit of $\sim 300\,\text{GeV}$, which is in the order of the centre–of–mass energy, can be produced. Such high masses are kinematically inaccessible at LEP and the bosonic stop decay modes considered are difficult to observe at the Tevatron.

The study presented here is particularly interesting following the observation of events with isolated electrons or muons and missing transverse momentum [6]. The dominant Standard Model source for such events is the production of real $W$ bosons. Some of these events have a hadronic final state with large transverse momentum and are not typical of SM $W$ production. These striking events may indicate a production mechanism involving processes beyond the Standard Model, such as the production of a scalar top quark and its decays as proposed in [7].

This analysis uses the data collected with the H1 detector in positron–proton scattering in the years 1994–1997 at a centre–of–mass energy of $\sqrt{s} = 301\,\text{GeV}$ and in 1999 and 2000 at $\sqrt{s} = 319\,\text{GeV}$. The data samples correspond to integrated luminosities of $37.9\,\text{pb}^{-1}$ and $67.9\,\text{pb}^{-1}$, respectively.

This thesis is structured as described in the following:

In chapter 2, a short overview of the SM and its physics in electron–proton ($ep$) collisions is given. The concept of SUSY is introduced and the phenomenology of resonant squark production in $ep$ scattering is described. The last section of this chapter discusses the analysis strategy.

The H1 detector at the HERA collider is briefly described in chapter 3.

Chapter 4 explains the basic data analysis, including data quality requirements, and the identification criteria for electrons, muons, jets and missing transverse momentum.

These objects are needed for the analysis of the final states of the bosonic stop decay; its results are presented in chapter 5.

An interpretation of the results is given in chapter 6. Furthermore, the limit derivation method is introduced and the resulting exclusion limits are presented for the investigated SUSY scenario.

Chapter 7 gives a summary of the results. Finally, a short outlook is presented.

# 2
# Theoretical Overview

In this introductory chapter, a short review of the Standard Model (for details see *e.g.* [8]) and its extensions is given. After the discussion of SM processes in electron–proton scattering, the main focus is on supersymmetry, which could give an elegant solution to the problems and deficiencies of the SM.

The concept of $R$–parity violation is introduced and the phenomenology of supersymmetric models with $\not{R}_p$ in electron–proton scattering is discussed, since $ep$ collisions are ideally suited to look for these SUSY models. In particular, the resonant production of stop quarks and their experimental signatures in $ep$ collisions are described. Finally, the Monte Carlo (MC) simulation of SM background processes and the SUSY signal is discussed and an outline of the analysis strategy is given.

## 2.1 The Standard Model

The Standard Model, based on the gauge principle, describes the three fundamental interactions of elementary particles: the electromagnetic, weak and strong interaction. SM particles are represented in the symmetry group

$$SU(3)_C \times SU(2)_{I_{3,L}} \times U(1)_Y, \tag{2.1}$$

where $C$ denotes the colour and $Y$ denotes the weak hypercharge. The subscript $I_{3,L}$ indicates that the weak isospin current only couples to left–handed fermions. The exchange of gauge fields of the corresponding local symmetry group mediate the forces of the SM.

The three parts which form the field content of the SM are described in the following.

## The fermion sector

Fermions – quarks and leptons (charged leptons and neutrinos) of three generations – are spin $1/2$ particles which describe matter and are associated to the fundamental representation of the gauge group of equation 2.1. The weak interaction is parity violating which leads to a left–right asymmetry of the SM. Thus, the left–handed fermions have quantum numbers which differ from those of the right–handed fermions. The representations of left–handed components of the fermion fields are isodoublets while the right–handed fermions are singlets:

$$
\text{Quarks} \quad \left\{ \begin{array}{ccc} \begin{pmatrix} u \\ d \end{pmatrix}_L & \begin{pmatrix} c \\ s \end{pmatrix}_L & \begin{pmatrix} t \\ b \end{pmatrix}_L \\[2ex] u_R & c_R & t_R \\ d_R & s_R & b_R \end{array} \right. \tag{2.2}
$$

$$
\text{Leptons} \quad \left\{ \begin{array}{ccc} \begin{pmatrix} \nu_e \\ e^- \end{pmatrix}_L & \begin{pmatrix} \nu_\mu \\ \mu^- \end{pmatrix}_L & \begin{pmatrix} \nu_\tau \\ \tau^- \end{pmatrix}_L \\[2ex] e_R^- & \mu_R^- & \tau_R^- \end{array} \right. \tag{2.3}
$$

Neutrinos only have a left–handed representation since they are assumed to be massless.

## The gauge boson sector

Gauge bosons are vector particles which mediate the interactions. The adjoint representation of the SM gauge group contains eight massless gluons $g_\mu^i$ with $i = 1...8$ which append to the $SU(3)_C$ symmetry group, three massive intermediate weak bosons $W_\mu^\pm, W_\mu^0$ belonging to the $SU(2)_{I_3,L}$ group and the boson $B_\mu$ associated to the $U(1)_Y$ group. Here, the index $\mu$ indicates the four–vector. The exchange of these gauge bosons between the matter particles with coupling constants $g_1, g_2$ and $g_3$ generates the forces of the SM. Since a mixing between the two neutral fields $W_\mu^0$ and $B_\mu$ produces the mass eigenstates $Z^0$ and $\gamma$, the gauge field content of the SM can be assigned to the interactions:

- The electromagnetic interaction is mediated by the massless photon $\gamma$.

- The weak interaction is mediated by the the heavy bosons $W^\pm$ and $Z^0$.

- The strong interaction is mediated by eight massless gluons $g_\mu^i$.

## The Higgs sector

Higgs bosons are scalar particles which generate the masses of SM particles by spontaneous symmetry breaking. The $SU(2)$ Higgs doublet (four states) which is composed of two scalar

Higgs fields with spin 0,

$$\Phi = \begin{pmatrix} \Phi^+ \\ \Phi^0 \end{pmatrix}, \tag{2.4}$$

is introduced to give masses to the intermediate weak gauge bosons by a spontaneous breaking of the symmetry $SU(2)_{I_{3,L}} \times U(1)_Y$. Moreover, the Yukawa couplings between a SM fermion and the scalar Higgs boson give masses to quarks and leptons. An additional term in the Lagrangian,

$$V(\Phi) = \mu^2 \Phi^\dagger \Phi + \lambda(\Phi^\dagger \Phi), \quad \text{with } \lambda > 0 \text{ and } \mu^2 < 0 \tag{2.5}$$

causes a non–vanishing vacuum expectation value $v = 246\,\text{GeV}$. Only one massive neutral Higgs boson $H^0$ appears if a particular choice of the vacuum is made. This Higgs boson couples to the weak gauge bosons and to fermions with coupling strength proportional to their masses. With this choice of the vacuum, the photon remains massless. The longitudinal polarisation of the vector bosons $W^\pm$ and $Z^0$ and the Higgs boson, occupy the four remaining scalar degrees of freedom.

The Higgs boson with mass

$$M_H = 2\lambda v^2, \tag{2.6}$$

which is a free parameter of the theory, is not yet discovered. A lower limit of $M_H > 114.4\,\text{GeV}$ at the $95\%$ confidence level results of a direct search [9], whereas an indirect search gives an upper limit of $M_H \lesssim 204\,\text{GeV}$ [10]. At tree–level and the on–shell scheme, the masses of the heavy vector bosons are related by

$$\sin^2 \theta_W = 1 - \frac{M_{W^\pm}^2}{M_{Z^0}^2}, \tag{2.7}$$

with $\theta_W$ being the Weinberg angle, a free parameter of the SM. This angle has experimentally been determined to $\sin^2 \theta_W = 0.23113(15)$ [10] in the $\overline{MS}$ renormalisation scheme.

## 2.2 Standard Model processes in electron–proton scattering

### Kinematics

In electron–proton scattering at HERA, a high centre–of–mass energy is available. Deep inelastic scattering (DIS) of the beam electron with a parton of the proton proceeds via the exchange of a gauge boson. A photon or a $Z^0$ boson is exchanged in neutral current (NC) DIS, while a $W^\pm$ is exchanged in charged current (CC) DIS processes. In the latter case, a neutrino $\nu_e$ is contained in the final state. In figure 2.1, electron–proton scattering and its kinematics is illustrated. Here, the quantity $P$ denotes the four–momentum of the incoming proton and $k$ and $k'$ are the four–momenta of the incoming and outgoing electron, respectively. The character $X$ indicates the recoiling system. The following Lorentz–invariant variables are commonly used:
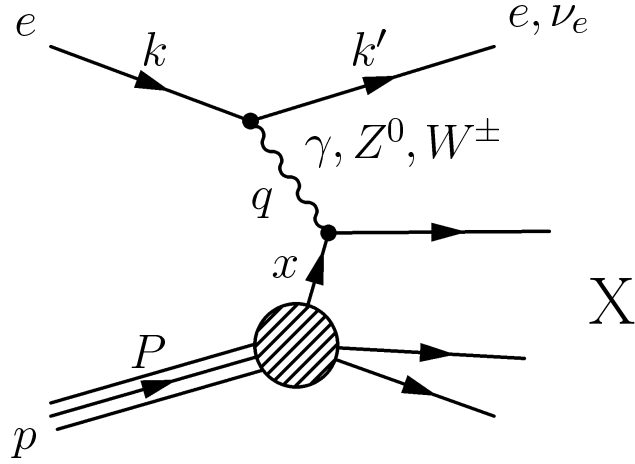
**Figure 2.1:** *An illustration of deep inelastic electron–proton scattering.*

- The negative of the four–momentum which is transfered to the proton by the exchanged particle is

$$Q^2 = -q^2 = (k - k')^2,\tag{2.8}$$

corresponding to the virtuality of the exchanged gauge boson.

- The electron–proton centre–of–mass energy squared,

$$s = (k + P)^2 = 4E_e^0 E_p^0.\tag{2.9}$$

Here, $E_e^0$ is the energy of the incoming electron and $E_p^0$ is the energy of the incoming proton.

- The two dimensionless variables

$$x = \frac{Q^2}{2P \cdot q} \quad \text{and} \quad y = \frac{P \cdot q}{P \cdot k}\tag{2.10}$$

which vary in the range $0 \leq x \leq 1$ and $0 \leq y \leq 1$, respectively. The variable $x$ is the Bjorken scaling variable and $y$ is the *inelasticity* of the scattering process. The latter corresponds to the relative energy transfer to the proton in its rest frame.

In the Quark–Parton–Model (QPM) [11] it is assumed that the proton is made of point–like constituents, the partons, which can be quarks and anti–quarks or gluons. Among these partons, the hadron momentum is distributed and the interacting parton carries a fraction $x$ of the proton four–momentum.

Due to energy and momentum conservation, these four introduced kinematic variables are not independent of each other. If the electron and proton masses are negligible, they are related via

$$Q^2 = sxy.\tag{2.11}$$

## Inclusive DIS cross sections

The cross section for the NC DIS reactions $e^{\pm}p \rightarrow e^{\pm}X$ can be written in terms of the variables $x$ and $Q^2$ as

$$\frac{d^2\sigma_{NC}(e^{\pm}p)}{dxdQ^2} = \frac{2\pi\alpha^2}{xQ^4}\phi_{NC}^{\pm}\left(1 + \Delta_{NC}^{\pm,weak}\right), \tag{2.12}$$

$$\text{with} \quad \phi_{NC}^{\pm} = Y_+\tilde{F}_2 \mp Y_-x\tilde{F}_3 - y^2\tilde{F}_L,$$

where $\alpha$ is the fine structure constant. The $\Delta_{NC}^{\pm,weak}$ corrections are defined in [12]. They are typically smaller than $1\%$ [13]. The NC structure function term $\phi_{NC}^{\pm}$ is expressed in terms of the generalised structure functions $\tilde{F}_2$, $x\tilde{F}_3$ and $\tilde{F}_L$. The terms $Y_{\pm} = 1 \pm (1-y)^2$ contain the helicity dependencies of the electroweak interaction. The structure function $\tilde{F}_2$ accounts for the dominant contribution from pure $\gamma$ exchange, the contributions from pure $Z$ exchange and the contributions from $\gamma Z$ interference. The structure function $x\tilde{F}_3$ only takes into account contributions from pure $Z$ exchange and $\gamma Z$ interference. Because the contributions from $Z$ boson exchange are only important at $Q^2 \gtrsim M_Z^2$, with $M_Z^2$ being the $Z$ boson mass, they are negligible in the region $Q^2 << M_Z^2$. Here, $\tilde{F}_2$ reduces to the electromagnetic structure function $F_2$.

The contribution of the longitudinal structure function $\tilde{F}_L$ is significant only at high $y$. The function $\tilde{F}_L$ is of the order of the strong coupling $\alpha_s$. In the QPM (where $\tilde{F}_L = 0$), the structure function $\tilde{F}_2$ can be expressed as a sum, and $\tilde{F}_3$ as a difference of the quark anti–quark densities in the proton.

The cross section for the CC DIS reactions $e^{\pm}p \rightarrow \bar{\nu}X$ can be expressed with the same notation as

$$\frac{d^2\sigma_{CC}(e^{\pm}p)}{dxdQ^2} = \frac{G_F^2}{2\pi x}\left(\frac{M_W^2}{M_W^2 + Q^2}\right)^2\phi_{CC}^{\pm}\left(1 + \Delta_{CC}^{\pm,weak}\right), \tag{2.13}$$

$$\text{with} \quad \phi_{CC}^{\pm} = \frac{1}{2}(Y_+W_2^{\pm} \mp Y_-xW_3^{\pm} - y^2W_L^{\pm}),$$

with $G_F$ being the Fermi constant. The term $\Delta_{CC}^{\pm,weak}$ represents the CC weak radiative corrections. The CC structure function term $\phi_{CC}^{\pm}$ is expressed in terms of the structure functions $W_2^{\pm}$, $xW_3^{\pm}$ and $W_L^{\pm}$, defined similar to the NC structure functions [14]. In the QPM (where $W_L^{\pm} = 0$), $W_2^{\pm}$ and $xW_3^{\pm}$ may be interpreted as lepton–beam charge dependent sums and differences of quark and anti–quark distributions. For example, for the charged current process $e^+p \rightarrow \bar{\nu}X$ and for an unpolarised lepton beam they are given by

$$W_2^+ = \sum_i 2x(d_i + \bar{u}_i)$$

$$xW_3^+ = \sum_i 2x(d_i - \bar{u}_i), \tag{2.14}$$

where the sum extends over all active down–type and anti–up–type quark densities. The quark flavour mixing is neglected. For the process $e^-p \rightarrow \nu X$, the CC structure functions are given by an interchange of the up– and down–type quark densities, respectively.
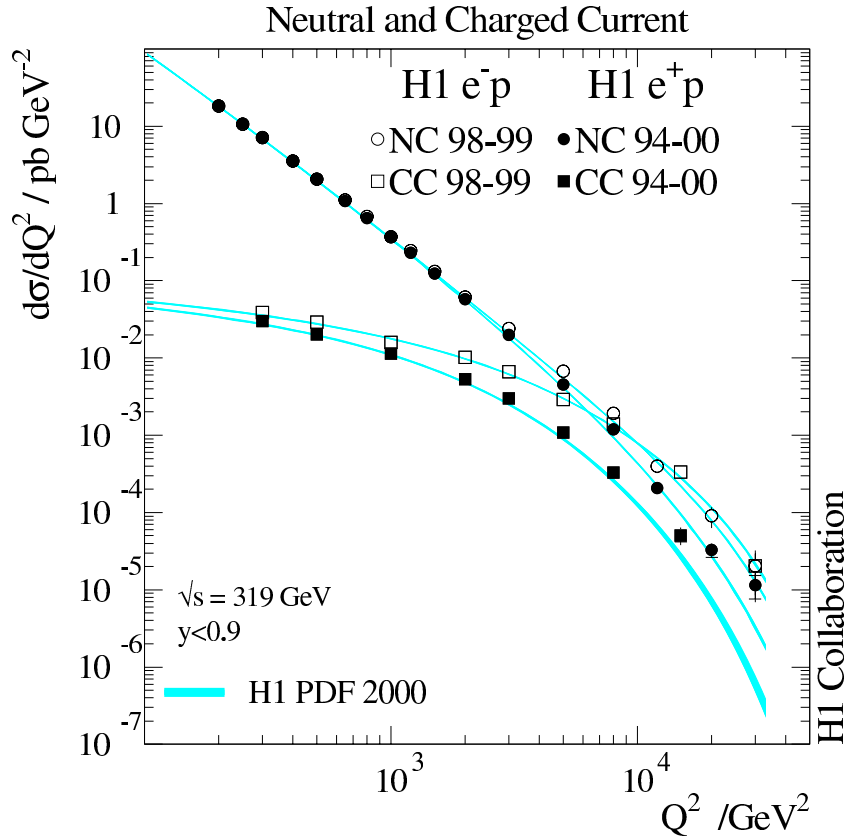
**Figure 2.2:** *The HERA measurements of the NC (circles) and CC (squares) cross sections as a function of $Q^2$ and the corresponding SM expectations (error bands).*

The cross sections given in equations 2.12 and 2.13 are suppressed by the propagator terms $P_{Z^0,W^\pm}(Q^2)$ which have the typical form

$$P_{Z^0,W^\pm}(Q^2) \sim \frac{Q^2}{Q^2 + M^2_{Z^0,W^\pm}}. \qquad (2.15)$$

Thus, interactions which comprise the exchange of the heavy gauge bosons $Z^0$ (NC) and $W^\pm$ (CC) only contribute at high $Q^2$. Below values of $Q^2 = \mathcal{O}(10^4\,\text{GeV}^2)$, which is about the vector boson masses squared, the CC cross section ($W^\pm$ exchange) is largely suppressed with respect to the NC cross section ($Z^0$ exchange). At high $Q^2$ values, the cross sections for the NC and CC DIS processes are of the same order of magnitude. The measurements of these NC and CC cross sections from HERA are shown in figure 2.2 as a function of $Q^2$. The shaded bands indicate the corresponding theoretical expectations.
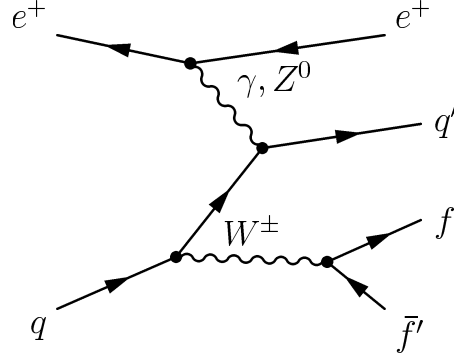
**Figure 2.3:** *An example for $W^\pm$ production: initial state $W$ radiation.*

## $W$ production

The most important SM background for the leptonic channels investigated in this analysis (see chapter 5.1) is the production of real $W^\pm$ bosons. In $ep$ collisions, they are dominantly produced by the process $ep \rightarrow eWX$. The dominant Feynman diagram which corresponds to initial state $W$ radiation is shown in figure 2.3. When both the photon and the $u$–channel quark are close to the mass shell, this process is the main contribution to the $ep \rightarrow eWX$ cross section [15].

# 2.3 Theories beyond the Standard Model

The Standard Model is an exceedingly successful theory. In diverse experiments, electroweak predictions of the SM can be confirmed at high precision. Nevertheless, the SM cannot explain the nature of gravity which gets important at the *Planck scale*

$$M_{Pl} = \sqrt{\frac{\hbar c}{G_F}} \approx 10^{19}\,\text{GeV}, \tag{2.16}$$

corresponding to a *Planck length* $l_{Pl} \approx 10^{-35}$m. At these small distances or high scales, the SM is no more capable of making any predictions. Thus, the SM cannot be accounted for as a complete theory.

Altogether, the SM needs $18$ parameters, including the fermion masses and the coupling constants of the electromagnetic, the strong and the weak interaction, in order to make theoretical predictions. Regarding this huge amount of free parameters and arbitrary choice of gauge groups, the SM is rather an effective low–energy theory of a superior theory. Such a theory could be a grand unified theory (GUT), in which the particles are represented in a $SU(5)$, $SO(10)$ or $E_6$ group containing the product $SU(3)_C \times SU(2)_{I_{3,L}} \times U(1)_Y$ (for reviews on GUT see [16]). Or it might be a string theory which also comprises gravity.
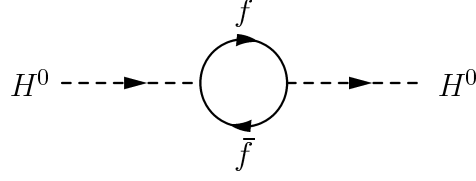
**Figure 2.4:** *The Feynman diagram for the fermion one–loop correction to the Higgs mass.*

## The hierarchy problem

Another theoretical problem of the SM is caused by the Higgs field. Since corrections to the bare masses of fundamental scalar fields have quadratic divergencies, a cut–off parameter $\Lambda$ is introduced. This parameter regulates the divergent one–loop correction to the Higgs mass shown in figure 2.4. Its contribution to the Higgs mass is [17]

$$\delta M_{Hf}^2 = \frac{|\lambda_f|^2}{16\pi^2}\left(-2\Lambda^2 + 6m_f^2 \ln(\Lambda/m_f) + ...\right), \tag{2.17}$$

where $M_f$ denotes the fermion mass and $\lambda_f$ is the coupling of the fermion to the Higgs field. The divergency is caused by the quadratic dependence of the Higgs mass on the cut–off scale $\Lambda$. It can be absorbed by renormalising the theory and redefining the Higgs mass. The parameter $\Lambda$ is assumed to be the GUT scale or the Planck scale if the SM is considered as an effective low–energy theory. This leads to the *hierarchy problem* [18,19]: the natural value of the Higgs mass and its value around the electroweak scale differ by a factor of $10^{14}$. Furthermore, the hierarchy $M_{EW} \ll M_{Pl}$ or $M_{GUT}$ is not stable under the radiative conditions given above.

Requiring that the Higgs mass $M_H$ is of the same order of magnitude as the electroweak scale, the bare Higgs mass $M_{Hb}$ in the SM has to be adjusted:

$$M_H^2 = M_{Hb}^2 + \delta M_{Hf}^2. \tag{2.18}$$

Here, the precision of the cancellation between $M_{Hb}$ and $\delta M_{Hf}$ must be of the order $10^{-12}$. This requires a fine–tuning of the parameters contained in the Lagrangian. The problem is called *fine–tuning problem* of the Standard Model.

## 2.4   Supersymmetry

The concept of *supersymmetry* [20, 21] is an elegant way to solve the hierarchy and the fine–tuning problem by introducing a superior symmetry. Assuming a scalar field $S$ coupling to the Higgs field, an additional contribution to the Higgs mass is given by [17]

$$\delta M_{HS}^2 \sim \frac{\lambda_S}{16\pi^2}\left(\Lambda^2 - 2m_S^2 \ln(\Lambda/m_S) + ...\right). \tag{2.19}$$

The corresponding loop is illustrated in figure 2.5. The $\Lambda^2$ contributions of equation 2.17 and
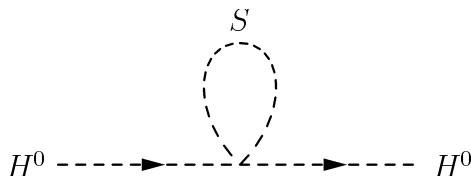
**Figure 2.5:** *The Feynman diagram for the boson one–loop correction to the Higgs mass.*

equation 2.19 annihilate if to each of the SM quarks and leptons two complex scalars with $\lambda_S = |\lambda_f|^2$ are assigned [17, 22].

Assuming that a symmetry exists which relates fermions and bosons gives the conditions for cancelling the contributions to scalar masses. These supersymmetric partners are generated by a transformation $Q$, which converts a fermionic state into a bosonic state and vice versa:

$$
\begin{aligned}
Q|\text{fermion}\rangle &= |\text{boson}\rangle \\
Q|\text{boson}\rangle &= |\text{fermion}\rangle.
\end{aligned}
\tag{2.20}
$$

A theory is called supersymmetric, if it is invariant under this transformation.

SUSY is a broken symmetry and thus, the hierarchy problem can be solved if supersymmetric particles with masses below $\sim 1\,\text{TeV}$ exist. In addition to the solution of the hierarchy problem and the unification of coupling constants, there are other persuasive arguments for SUSY. For example, SUSY can predict accurately the electroweak mixing parameter $\sin^2 \theta_W$ at the per mill level and the lightest supersymmetric particle (LSP) might be a candidate for cold dark matter, being substantial in cosmology. Furthermore, SUSY gives an indication for including gravity.

## 2.4.1   The Minimal Supersymmetric Standard Model

One of the supersymmetric extensions of the SM is the Minimal[1] Supersymmetric Standard Model (MSSM). In figure 2.6, the running of the coupling constants is illustrated for the SM and the MSSM as a function of the scale. In the MSSM the couplings unify at scales around $10^{16}\,\text{GeV}$. The gradient in their evolution is caused by the fact that SUSY particles contribute only above about $1\,\text{TeV}$. This is assumed to be the effective SUSY scale.

In the MSSM, each particle has to be arranged in a *chiral* or a *gauge* supermultiplet. A chiral supermultiplet comprises a two–component Weyl fermion and a complex scalar field. A gauge supermultiplet is a combination of a vector boson with spin 1 (two states) and a Weyl fermion (two states). Before the spontaneous symmetry breaking, the vector boson is massless.

Quarks and leptons have different gauge transformations. Therefore, they have to be contained in chiral supermultiplets [17]. To each of the left–handed and right–handed SM fermions, a complex scalar SUSY partner must be assigned. These SUSY particles are called *squarks* ($\tilde{q}$) if they are scalar quarks or *sleptons* ($\tilde{l}$) if they are scalar leptons. For example, the $\tilde{e}_{L,R}$ is the

---

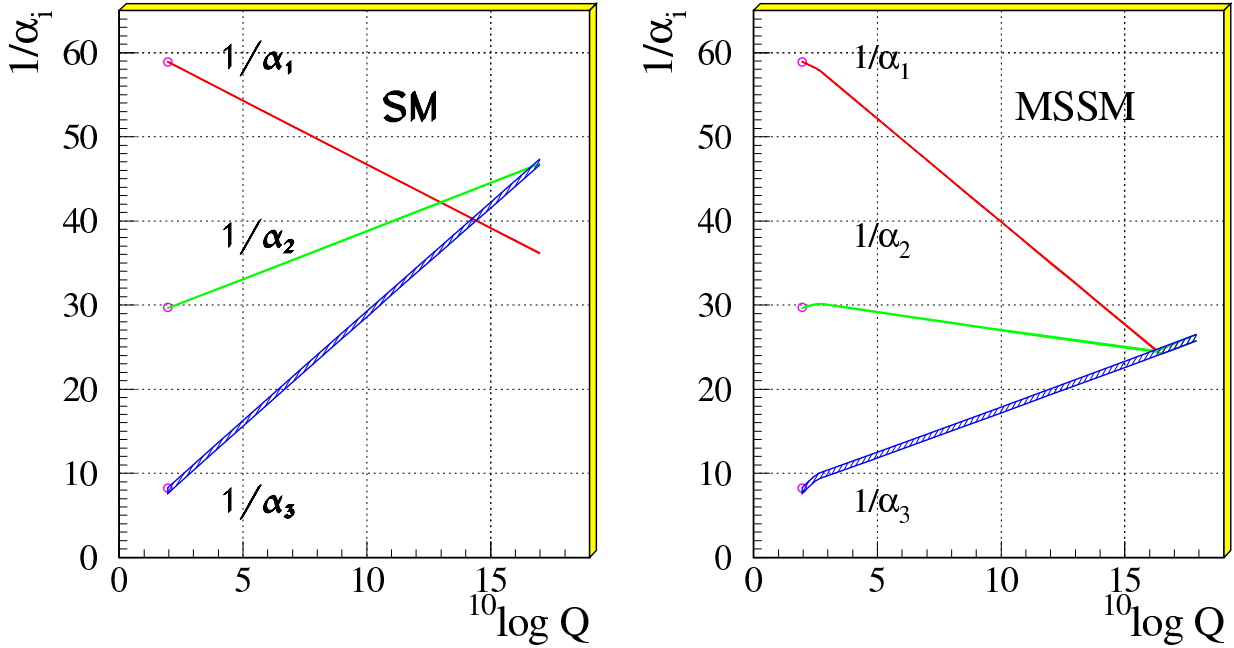[1]*Minimal* because at least two Higgs fields are required.

**Figure 2.6:** *The evolution of the inverse of the three coupling constants in the SM and in the MSSM.*

scalar partner of the left–handed (right–handed) lepton $e_{L,R}$. It is important that the indices $L$ and $R$ do not refer to the helicity of the squark or slepton since they are scalars. The indices $L$ and $R$ only refer to the handedness of the corresponding SM partner (quark or lepton). All SUSY particles are denoted by a tilde.

The scalar Higgs boson is a spin $0$ particle. Thus it must be contained in a chiral supermultiplet as well. In supersymmetric extensions of the Standard Model, the scalar Higgs fields are composed of two complex $SU(2)_L$–doublets $(H_u^+, H_u^0)$ and $(H_d^0, H_d^-)$ in order to avoid triangle gauge anomalies. The chiral supermultiplet $H_u$ with $Y = 1/2$ generates the masses of up–type quarks $(u, c, t)$, whereas the masses of down–type quarks $(d, s, b)$ and of charged leptons $(e, \mu, \tau)$ are generated by the chiral supermultiplet $H_d$ with $Y = -1/2$. The vacuum expectation values $v_u$ and $v_d$ of these Higgs doublets are non–zero and their ratio

$$\tan \beta = \frac{v_u}{v_d} \tag{2.21}$$

is a free parameter of the model.

Breaking the electroweak symmetry, five of the eight degrees of freedom correspond to the Higgs mass eigenstates which are linear combinations of $H_u^+, H_u^0, H_d^0$ and $H_d^-$: $A_0$ ($CP$–odd neutral scalar), $H^+$ (positive charged scalar), $H^-$ (its conjugate scalar), $H^0$ and $h^0$ ($CP$–even neutral scalars). The $h^0$ is associated to the neutral scalar SM Higgs boson. A superpartner with spin $1/2$ is denoted by appending "-ino" to the name of the corresponding SM particle. Thus, the SUSY partners of Higgs bosons are called *higgsinos*. The residual three degrees of freedom get occupied by the longitudinal modes of the vector bosons $W^{\pm}$ and $Z^0$.

| SM particles | | spin | SUSY partners | | spin |
|---|---|---|---|---|---|
| quark | $q_{L,R}$ | $\frac{1}{2}$ | squark | $\tilde{q}_L$, $\tilde{q}_R$ | $0$ |
| lepton | $l_{L,R}$ | $\frac{1}{2}$ | slepton | $\tilde{l}_L$, $\tilde{l}_R$ | $0$ |
| Higgs bosons | $H_u^0$, $H_u^+$ | $0$ | higgsinos | $\tilde{H}_u^0$, $\tilde{H}_u^+$ | $\frac{1}{2}$ |
| | $H_d^0$, $H_d^-$ | $0$ | | $\tilde{H}_d^0$, $\tilde{H}_d^-$ | $\frac{1}{2}$ |
| gluon | $g$ | $1$ | gluino | $\tilde{g}$ | $\frac{1}{2}$ |
| W bosons | $W^{\pm,0}$ | $1$ | winos | $\tilde{W}^{\pm,0}$ | $\frac{1}{2}$ |
| B boson | $B$ | $1$ | bino | $\tilde{B}$ | $\frac{1}{2}$ |

**Table 2.1:** *The particle content of the supermultiplets in the MSSM.*

The vector bosons of the SM ($W^\pm$, $W^0$ and $B^0$) are contained in a gauge supermultiplet. Their SUSY partners are the winos $\tilde{W}^\pm$ and $\tilde{W}^0$ and the bino ($\tilde{B}^0$). All superpartners of SM gauge bosons are called *gauginos*. The SUSY partner of the gluon ($g$) is the gluino $\tilde{g}$.

The particle content of all supermultiplets in the MSSM is listed in table 2.1.

The mass eigenstates of the MSSM originate from a mixing of the superpartners, which is caused by electroweak symmetry breaking effects:

- The two neutral gauginos ($\tilde{W}^0$, $\tilde{B}^0$) and the two neutral higgsinos ($\tilde{H}_u^0$, $\tilde{H}_d^0$) mix to four *neutralinos*, $\tilde{\chi}_i^0$ with $i = 1...4$, the neutral mass eigenstates.

- The two charged gauginos ($\tilde{W}^-$, $\tilde{W}^+$) and the two charged higgsinos ($\tilde{H}_u^+$, $\tilde{H}_d^-$) mix to two *charginos*, $\tilde{\chi}_i^\pm$ with $i = 1, 2$, the mass eigenstates with charge $\pm 1$.

By convention, the neutralinos are ordered in mass, as well as the charginos:

$$M_{\tilde{\chi}_1^0} < M_{\tilde{\chi}_2^0} < M_{\tilde{\chi}_3^0} < M_{\tilde{\chi}_4^0} \quad \text{and}$$
$$M_{\tilde{\chi}_1^\pm} < M_{\tilde{\chi}_2^\pm}. \tag{2.22}$$

In large parts of the SUSY parameter space the $\tilde{\chi}_1^0$ is the LSP.

## Supersymmetry breaking

None of the SUSY particles has been observed yet. Therefore, SUSY must be a broken symmetry. In the MSSM, supersymmetry breaking is introduced explicitly.

The MSSM contains more than $140$ parameters, but in the radical approach of minimal supergravity (mSUGRA), the number of parameters is reduced to $5$:

$$M_1 = M_2 = M_3 = m_{1/2} \text{ at the GUT scale,}$$
$$m_0, \tan\beta, \mu \text{ and } A_0 \tag{2.23}$$

where $M_1$ is the bino ($\tilde{B}^0$) mass parameter, $M_2$ is the wino ($\tilde{W}^0$) mass parameter and $M_3$ is the mass parameter of the gluino ($\tilde{g}$). The parameters $m_{1/2}$ and $m_0$ denote the common gaugino mass and the common mass of all sfermions and Higgs bosons, respectively, at the GUT scale. The parameter $\mu$ corresponds to the Higgs boson mass parameter in the SM and $A_0$ is the soft SUSY breaking trilinear coupling between Higgs scalars and sfermions at the GUT scale.

Assuming that the coupling constants unify at the GUT scale (see figure 2.6), in these minimal supergravity models the one–loop renormalisation group (RG) equations for the three gaugino mass parameters in the MSSM lead to the relation [17]

$$\frac{M_1}{\alpha_1} = \frac{M_2}{\alpha_2} = \frac{M_3}{\alpha_3} \tag{2.24}$$

at any RG scale. In models which satisfy this relation (equation 2.24), $M_2$ is related to $M_1$ via

$$M_1 = \frac{5}{3}\tan^2\theta_W M_2 \tag{2.25}$$

at the electroweak scale.

The gluino mass parameter $M_3$ is related to the bino and wino mass parameters $M_1$ and $M_2$ by [17]

$$M_3 = \frac{\alpha_s}{\alpha}\sin^2\theta_W M_2 = \frac{3}{5}\frac{\alpha_s}{\alpha}\cos^2\theta_W M_1. \tag{2.26}$$

at any RG scale in models which follow from minimal supergravity or gauge mediated boundary conditions. With the values $\alpha_s = 0.118$, $\alpha = 1/128$ and $\sin^2\theta_W = 0.23$, the relation $M_3 : M_2 : M_1 \approx 7 : 2 : 1$ can be predicted at the electroweak scale [17]. Hence, the gluino is expected to be much heavier than the neutralinos and charginos.

In the present analysis, a different approach is used. Here, a Minimal Supersymmetric Standard Model is assumed in which all sfermion masses are free parameters, as well as the squark mixings, the soft SUSY breaking trilinear couplings and the couplings between any two SUSY particles and a standard model fermion or boson.

In the model which is investigated here, the slepton masses and the squark masses of the first two generations are chosen to be 1 TeV. Furthermore, the relations between $M_1$, $M_2$ and $M_3$ given in equations 2.25 and 2.26 at the electroweak scale are assumed to hold. Thus, only the parameter $M_2$ is arbitrary and chosen to be $1000\,\text{GeV}$ at the electroweak scale. The masses and the composition of neutralinos and charginos are given by the three SUSY parameters $\mathbf{\tan\beta}$, $\boldsymbol{\mu}$ and $\mathbf{M_2}$ only.

The parameters investigated in this work are

$$M_2, \tan\beta, \mu$$
$$M_{\tilde{t}_1}, M_{\tilde{b}_1}, \theta_{\tilde{t}}, \theta_{\tilde{b}}, A_t \text{ and } A_b. \tag{2.27}$$

In addition, the Yukawa coupling $\lambda'_{131}$ which describes the coupling of a lepton and a quark of the first generation to a squark of the third generation (see section 2.4.4) is analysed. The mass parameters $M_{\tilde{t}_1}$ and $M_{\tilde{b}_1}$ are the masses of the lighter stop and sbottom states, respectively. The angle $\theta_{\tilde{t}}$ is the stop mixing angle and $\theta_{\tilde{b}}$ is the sbottom mixing angle (see section 2.4.3). The parameters $A_t$ and $A_b$ are soft SUSY breaking trilinear couplings. The masses of the heavier stop and sbottom states, $M_{\tilde{t}_2}$ and $M_{\tilde{b}_2}$, are determined by the relation between the stop and sbottom mixing angles and masses and the SUSY parameters $A_t$, $A_b$, $\tan\beta$ and $\mu$ as explained in section 2.4.3.

## 2.4.2 Sparticles decays

The common decay modes of supersymmetric particles in the MSSM with $R_p$ conservation (see section 2.4.4) are briefly described in this section. All decay chains end up in final states containing a LSP.

- Squarks decay into a quark and a gaugino,

$$\tilde{q} \to q\tilde{g} \qquad \tilde{q} \to q\tilde{\chi}_i^0 \qquad \tilde{q} \to q'\tilde{\chi}_i^\pm. \tag{2.28}$$

The decay into a gluino has a strong coupling strength and will therefore dominate, if kinematically allowed. Otherwise, the direct decay to the LSP $\tilde{q} \to q\tilde{\chi}_1^0$ is always kinematically favoured.

The handedness of the SM partner of the squark has a strong influence on the couplings of a squark to charginos: the couplings of the SUSY partner of a right–handed quark ("right" squark) $\tilde{q}_R$ to charginos are suppressed, whereas the SUSY partner of a left–handed quark ("left" squark) $\tilde{q}_L$ couples to both neutralinos and charginos. Since "right" squarks do not couple to winos, the coupling also depends on the mixing parameters of neutralinos and charginos.

Squarks can also decay into a lighter squark and a SM gauge boson or a Higgs boson, but these decays are largely suppressed as soon as the decays in equation 2.28 are kinematically allowed. Therefore, the light stop quarks could undergo a bosonic decay into a sbottom and a $W$ boson, $\tilde{t} \to \tilde{b}W$, as far as the sbottom is lighter than the stop and if the decays into quarks and gauginos are kinematically suppressed [7]. This process is the subject of the present analysis and is described in detail in section 2.5.2.

- Sleptons decay into leptons and neutralinos or charginos with electroweak strength,

$$\tilde{l} \to l\tilde{\chi}_i^0 \qquad \tilde{l} \to \nu\tilde{\chi}_i^\pm \qquad \tilde{\nu} \to \nu\tilde{\chi}_i^0 \qquad \tilde{\nu} \to l\tilde{\chi}_i^\pm, \tag{2.29}$$

due to the gaugino content of neutralinos and charginos [17].

- Neutralinos and charginos can decay into a fermion and a sfermion,

$$\tilde{\chi}_i^0 \rightarrow l\tilde{l}, \nu\tilde{\nu}, q\tilde{q} \quad \text{and} \quad \tilde{\chi}_i^0 \rightarrow l\tilde{\nu}, \nu\tilde{l}, q\tilde{q}', \tag{2.30}$$

if kinematically allowed. In addition, neutralinos and charginos inherit the gaugino–higgsino–Higgs and gaugino–gaugino–vector boson couplings of their components [17]. Thus, they can decay into a lighter neutralino or chargino and an electroweak gauge boson or a scalar Higgs,

$$\tilde{\chi}_i^0 \rightarrow Z^0\tilde{\chi}_j^0, W^\pm\tilde{\chi}_j^\mp, h^0\tilde{\chi}_j^0 \quad [A^0\tilde{\chi}_j^0, H^0\tilde{\chi}_j^0, H^\pm\tilde{\chi}_j^\mp]$$

$$\tilde{\chi}_i^\pm \rightarrow W^\pm\tilde{\chi}_j^0, Z^0\tilde{\chi}_1^\pm, h^0\tilde{\chi}_1^\pm \quad [A^0\tilde{\chi}_1^\pm, H^0\tilde{\chi}_1^\pm, H^\pm\tilde{\chi}_j^0]. \tag{2.31}$$

The final states in brackets are kinematically suppressed since the $h^0$ is assumed to be the lightest Higgs boson. If the two–body decay modes are kinematically forbidden, the neutralinos and charginos can undergo three–body decays into two fermions and a lighter $\tilde{\chi}_j^0$ or $\tilde{\chi}_j^\pm$

$$\tilde{\chi}_i^0 \rightarrow f f \tilde{\chi}_j^0 \qquad \tilde{\chi}_i^0 \rightarrow f f' \tilde{\chi}_j^\pm \qquad \tilde{\chi}_i^\pm \rightarrow f f' \tilde{\chi}_j^0 \qquad \tilde{\chi}_2^\pm \rightarrow f f' \tilde{\chi}_1^\pm \tag{2.32}$$

via the off–shell gauge bosons, Higgs scalars and sfermions which appeared in equation 2.31.

- Gluinos decay via the strong coupling, $\tilde{g} \rightarrow q\tilde{q}$. If this dominant two–body decay is kinematically forbidden, the gluino decays in three–body reactions into quarks and neutralinos or charginos via off–shell squarks [17].

## 2.4.3   Masses and mixing in the third generation

In general, any scalars with the same charge and color quantum numbers can mix. Thus, there is also a mixing between squarks[2]. Due to the large top Yukawa coupling, large mixings between $\tilde{t}_L$ and $\tilde{t}_R$ are conceivable and one of the stop mass eigenstates can be much lighter than the other squarks. The bottom Yukawa coupling can also be quite large if $\tan\beta \gtrsim 10$ [23]. Therefore, also the mixing between $\tilde{b}_L$ and $\tilde{b}_R$ is considered.

Calculated from the Lagrangian of the MSSM, the mass matrices for the stop and sbottom system in the $(\tilde{t}_L, \tilde{t}_R)$ or $(\tilde{b}_L, \tilde{b}_R)$ basis, respectively, can be expressed as [24, 25, 26, 27]

$$\mathcal{M}_{\tilde{t}}^2 = \begin{pmatrix} M_{\tilde{t}_L}^2 & a_t M_t \\ a_t M_t & M_{\tilde{t}_R}^2 \end{pmatrix} \quad \text{and} \quad \mathcal{M}_{\tilde{b}}^2 = \begin{pmatrix} M_{\tilde{b}_L}^2 & a_b M_b \\ a_b M_b & M_{\tilde{b}_R}^2 \end{pmatrix}, \tag{2.33}$$

---

[2]Sleptons can mix as well, but their mixing is not relevant to the present analysis and thus not described here.

where $M_t$ denotes the top mass and $M_b$ is the bottom mass. The parameters $a_t$ and $a_b$ are given by [24]

$$
\begin{aligned}
a_t M_t &= M_t(A_t - \mu \cot \beta) \\
a_b M_b &= M_b(A_b - \mu \tan \beta),
\end{aligned}
\tag{2.34}
$$

where the parameters $A_t$ and $A_b$ denote the soft SUSY breaking trilinear couplings of Higgs scalars and sfermions. As can be seen from equation 2.34, the sbottom mixing can be as important as the stop mixing leading to a large mass splitting also in the sbottom system, if $\tan \beta$ is large. The mass eigenvalues following from the mass matrices of equation 2.33 are:

$$
M^2_{\tilde{t}_1,\tilde{t}_2} = \frac{1}{2}\left(M^2_{\tilde{t}_L} + M^2_{\tilde{t}_R}\right) \mp \frac{1}{2}\sqrt{(M^2_{\tilde{t}_L} - M^2_{\tilde{t}_R})^2 + (2a_t M_t)^2}
\tag{2.35}
$$

$$
M^2_{\tilde{b}_1,\tilde{b}_2} = \frac{1}{2}\left(M^2_{\tilde{b}_L} + M^2_{\tilde{b}_R}\right) \mp \frac{1}{2}\sqrt{(M^2_{\tilde{b}_L} - M^2_{\tilde{b}_R})^2 + (2a_b M_b)^2}
\tag{2.36}
$$

with the convention $M_{\tilde{t}_1} < M_{\tilde{t}_2}$ and $M_{\tilde{b}_1} < M_{\tilde{b}_2}$. The difference between these mass eigenstates is large because the top and sbottom masses are large. For the first two generations, the mass splitting is negligible because here the corresponding quark masses are small, *i.e.* the scalars are quasi degenerate in mass.

The mixing angles $\theta_{\tilde{t}}$ and $\theta_{\tilde{b}}$ parameterise the mass eigenstates and the lightest stop and sbottom mass eigenstates, $\tilde{t}_1$ and $\tilde{b}_1$, are obtained by diagonalising the stop and sbottom mass matrices of equation 2.33:

$$
\begin{aligned}
\tilde{t}_1 &= \tilde{t}_L \cos\theta_{\tilde{t}} + \tilde{t}_R \sin\theta_{\tilde{t}} \\
\tilde{t}_2 &= -\tilde{t}_L \sin\theta_{\tilde{t}} + \tilde{t}_R \cos\theta_{\tilde{t}} \\[2mm]
\tilde{b}_1 &= \tilde{b}_L \cos\theta_{\tilde{b}} + \tilde{b}_R \sin\theta_{\tilde{b}} \\
\tilde{b}_2 &= -\tilde{b}_L \sin\theta_{\tilde{b}} + \tilde{b}_R \cos\theta_{\tilde{b}}.
\end{aligned}
\tag{2.37}
$$

The mixing angles $\theta_{\tilde{t}}$ and $\theta_{\tilde{b}}$, derived from equation 2.33, can now be expressed as

$$
\cos\theta_{\tilde{t}} = \frac{-a_t M_t}{\sqrt{(M^2_{\tilde{t}_L} - M^2_{\tilde{t}_1})^2 + a_t^2 M_t^2}} \qquad \sin\theta_{\tilde{t}} = \sqrt{\frac{(M^2_{\tilde{t}_L} - M^2_{\tilde{t}_1})^2}{(M^2_{\tilde{t}_L} - M^2_{\tilde{t}_1})^2 + a_t^2 M_t^2}}
\tag{2.38}
$$

$$
\cos\theta_{\tilde{b}} = \frac{-a_b M_b}{\sqrt{(M^2_{\tilde{b}_L} - M^2_{\tilde{b}_1})^2 + a_b^2 M_b^2}} \qquad \sin\theta_{\tilde{b}} = \sqrt{\frac{(M^2_{\tilde{b}_L} - M^2_{\tilde{b}_1})^2}{(M^2_{\tilde{b}_L} - M^2_{\tilde{b}_1})^2 + a_b^2 M_b^2}}.
\tag{2.39}
$$

As can be seen from equations 2.38 and 2.39, the mixing angles are dependent on the masses of the corresponding quarks. Squarks of the first two generations have a very small mixing angle since the masses of the corresponding quarks are small (see above).

Expressed in terms of the mass eigenstates, *i.e.* following from equations 2.34, 2.35 and 2.36 and using equations 2.38 and 2.39, the squark mixing parameters and masses of the third generation and the SUSY parameters $A_t$, $A_b$, $\tan\beta$ and $\mu$ are related by

$$M_{\tilde{t}_1}^2 - M_{\tilde{t}_2}^2 = \frac{2M_t\left(A_t - \mu\cot\beta\right)}{\sin 2\theta_{\tilde{t}}} \quad \text{and} \tag{2.40}$$

$$M_{\tilde{b}_1}^2 - M_{\tilde{b}_2}^2 = \frac{2M_b\left(A_b - \mu\tan\beta\right)}{\sin 2\theta_{\tilde{b}}}. \tag{2.41}$$

All sfermion masses are free parameters in the model, as well as the squark mixings $\theta_{\tilde{t}}$ and $\theta_{\tilde{b}}$ and the soft SUSY breaking trilinear couplings $A_t$ and $A_b$. Because of the large top mass $M_t$ the stop is likely to be the lightest squark. Nevertheless, the sbottom could be lighter than the stop, depending on the specific choice of the SUSY parameter space.

## 2.4.4   $R$-parity and $R$-parity violation

The interactions and masses of all particles are described by *superpotentials* in the notation which is used for the description of supersymmetric models (for details see *e.g.* [28, 29]). The form of these superpotentials is given by gauge invariance. Single objects which contain all bosonic and fermionic fields within the corresponding supermultiplets of table 2.1 as components, are called *superfields*.

The most general supersymmetric theory which is gauge invariant with respect to the Standard Model gauge group allows Yukawa couplings between two SM fermions and a squark or a slepton. The corresponding part of the superpotential consists of terms in which either lepton number or baryon number conservation is violated, can be expressed as [30, 31]

$$W_{\not{R}_p} = \frac{1}{2}\lambda_{ijk}L_iL_j\bar{E}_k + \lambda'_{ijk}L_iQ_j\bar{D}_k + \frac{1}{2}\lambda''_{ijk}\bar{U}_i\bar{D}_j\bar{D}_k. \tag{2.42}$$

Here, the subscripts $i, j, k$ are generation indices. The $L_i$ denote the lepton $SU(2)$–doublet superfields, $\bar{E}_i$ the $SU(2)$–singlet charge–conjugated lepton superfields, $Q_i$ the quark $SU(2)$–doublet superfields and $\bar{D}_i$ and $\bar{U}_i$ the $SU(2)$–singlet charge–conjugated down– and up–type quark fields. The dimensionless Yukawa couplings $\lambda_{ijk}$, $\lambda'_{ijk}$ and $\lambda''_{ijk}$ are free parameters of the model. Figure 2.7 shows the diagrams corresponding to the terms described by equation 2.42. For a review on $R$–parity violating supersymmetry see [32].

In the present analysis, the emphasis is placed on the second term of equation 2.42, $\lambda'_{ijk}L_iQ_j\bar{D}_k$, since it describes a quark–lepton–squark vertex (figure 2.7 b)). This vertex is of particular interest in electron–proton scattering at HERA because it allows for the resonant production of single squarks (see section 2.5). In particular, the resonant production of single stop quarks is possible which is the focus of this analysis.
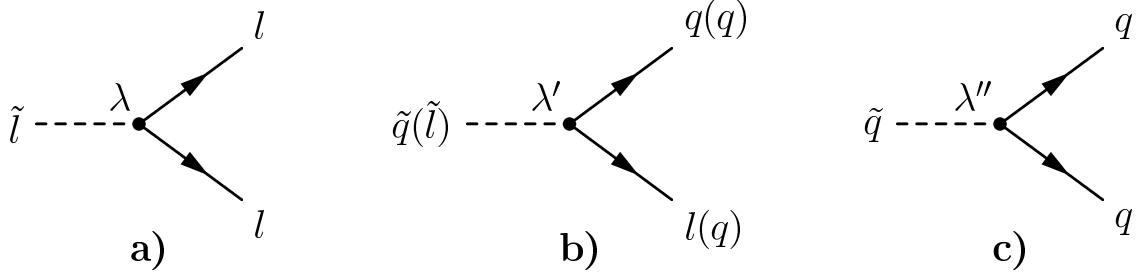
**Figure 2.7:** *The diagrams corresponding to the terms described by equation 2.42. a)* $\lambda_{ijk} L_i L_j \bar{E}_k$*; b)* $\lambda'_{ijk} L_i Q_j \bar{D}_k$*; c)* $\lambda''_{ijk} \bar{U}_i \bar{D}_j \bar{D}_k$*. Process b) is of particular interest in electron–proton scattering.*

The new couplings introduced in equation 2.42 induce violation of the *R–parity*, defined as [33]

$$R_p = (-1)^{3B+L+2S} \tag{2.43}$$

which is a multiplicative conserved quantum number. Here, $B$ is the baryon number, $L$ is the lepton number and $S$ is the spin of a particle. According to equation 2.43, ordinary SM particles carry $R_p = +1$, while SUSY particles have $R_p = -1$. With the definition of this new quantum number, the first two terms in equation 2.42 violate lepton number conservation, while the last term violates baryon number conservation.

If $R$–parity is conserved all terms in equation 2.42 are zero. The main effects for the phenomenology in $R_p$ conserving models are: the LSP is stable[3] and each SUSY particle – apart from the LSP – decays to a final state which contains an odd number of LSPs. In addition, at colliders sparticles are produced in pairs since the initial state consists only of SM particles.

At HERA, the dominant $R_p$ conserving MSSM process is the selectron–squark production via a t–channel neutralino exchange, $eq \rightarrow \tilde{e}\tilde{q}$. The subsequent decays $\tilde{e} \rightarrow e\tilde{\chi}_1^0$ and $\tilde{q} \rightarrow q\tilde{\chi}_1^0$ lead to signatures with an electron with high transverse momentum, a jet and large missing energy. Analyses at the HERA collaborations have set limits of $(M_{\tilde{e}} + M_{\tilde{q}})/2 > 77\,\text{GeV}$ [34, 35] which cannot compete with new results from LEP or Tevatron any longer.

## *R*–parity violation

In the MSSM, $R_p$ is assumed to be conserved, although $R_p$ conservation is not motivated at a fundamental level in supersymmetric theories. Thus, also $R_p$ violating SUSY models are accounted for. If both Yukawa couplings $\lambda'$ and $\lambda''$ are non–zero, the proton–lifetime would be shorter than experimentally observed. The usual assumption is that only one term in equation 2.42 has a non–zero coupling constant. This leads to essential changes of the SUSY phenomenology with the following consequences:

---

[3]If the only weakly interacting $\tilde{\chi}_1^0$ is the LSP, the *golden signature* in collider experiments is missing energy.

- The LSP can decay into SM particles. Hence, the $\not{R}_p$ neutralino decays $\tilde{\chi}_1^0 \to \nu \bar{q} q$ and $\tilde{\chi}_1^0 \to e \bar{q} q$ are possible. Moreover, in $\not{R}_p$ models the signatures in collider experiments are final states containing leptons and/or jets instead of the missing energy signature of $R_p$ conserving models.

- At colliders, it is possible to resonantly produce single SUSY particles since two Standard Model fermions can produce a squark or a slepton via a $\not{R}_p$ coupling. In particular, at HERA single squarks can be produced resonantly via the $\not{R}_p$ coupling $\lambda'_{ijk}$.

In this analysis, the approach of single SUSY particle production is studied, in particular the single stop production, followed by $\not{R}_p$ decays which also proceed via the term $\lambda'_{ijk} L_i Q_j \bar{D}_k$.

# 2.5    Phenomenology of $\not{R}_p$ SUSY in electron–proton scattering

The electron–proton collider HERA is a unique facility to search for new particles which couple to an electron and a quark. In $\not{R}_p$ SUSY models where $\lambda'$ is non–zero, a lepton–quark vertex (see figure 2.7) allows for resonant squark production in electron–proton scattering [36]. The part of the Lagrangian which corresponds to the term $\lambda'_{ijk} L_i Q_j \bar{D}_k$ of the superpotential (see equation 2.42) is given by expanding the superfields of this term in their components,

$$
\begin{aligned}
\mathcal{L}_{L_i Q_j \overline{D}_k} = \lambda'_{ijk} \Big[ &-\tilde{e}_L^i u_L^j \bar{d}_R^k - e_L^i \tilde{u}_L^j \bar{d}_R^k - (\bar{e}_L^i)^c u_L^j \tilde{d}_R^{k*} \\
&+ \tilde{\nu}_L^i d_L^j \bar{d}_R^k + \nu_L^i \tilde{d}_L^j \bar{d}_R^k + (\bar{\nu}_L^i)^c d_L^j \tilde{d}_R^{k*} \Big] + c.c.,
\end{aligned}
\tag{2.44}
$$

where the superscripts $c$ indicate the charge conjugate spinors and $*$ the complex conjugate of scalar fields. In $e^\pm p$ scattering, nine possible couplings $\lambda'_{ijk}$ lead to the squark production processes given in table 2.2. With an initial $e^+$ beam, HERA is most sensitive to the couplings $\lambda'_{1j1}$ ($j = 1, 2, 3$) since in the proton there are mainly quarks. Thus, in $e^+ p$ collisions, mainly $\tilde{u}_L^j$ type squarks ($\tilde{u}_L, \tilde{c}_L, \tilde{t}_L$) are produced, whereas mainly down–type squarks are produced in $e^- p$ collisions. Here, with an initial $e^-$ beam HERA is most sensitive to the couplings $\lambda'_{11k}$ ($k = 1, 2, 3$). The latter processes are not considered in this analysis since only the production of stop quarks is of particular interest.

The invariant mass of the squark resonantly produced in electron–proton scattering can be expressed as

$$
m = \sqrt{xs}, \tag{2.45}
$$

where $\sqrt{s}$ is the centre–of–mass energy calculated as in equation 2.9 and $x$ is the fraction of the proton four–momentum as given in equation 2.10.

| $\lambda'_{ijk}$ | $e^+p$ | | $e^-p$ | |
|---|---|---|---|---|
| 111 | $e^+ + d \longrightarrow \tilde{u}_L$ | $e^+ + \bar{u} \longrightarrow \bar{\tilde{d}}_R$ | $e^- + u \longrightarrow \tilde{d}_R$ | $e^- + \bar{d} \longrightarrow \bar{\tilde{u}}_L$ |
| 112 | $e^+ + s \longrightarrow \tilde{u}_L$ | $e^+ + \bar{u} \longrightarrow \bar{\tilde{s}}_R$ | $e^- + u \longrightarrow \tilde{s}_R$ | $e^- + \bar{s} \longrightarrow \bar{\tilde{u}}_L$ |
| 113 | $e^+ + b \longrightarrow \tilde{u}_L$ | $e^+ + \bar{u} \longrightarrow \bar{\tilde{b}}_R$ | $e^- + u \longrightarrow \tilde{b}_R$ | $e^- + \bar{b} \longrightarrow \bar{\tilde{u}}_L$ |
| 121 | $e^+ + d \longrightarrow \tilde{c}_L$ | $e^+ + \bar{c} \longrightarrow \bar{\tilde{d}}_R$ | $e^- + c \longrightarrow \tilde{d}_R$ | $e^- + \bar{d} \longrightarrow \bar{\tilde{c}}_L$ |
| 122 | $e^+ + s \longrightarrow \tilde{c}_L$ | $e^+ + \bar{c} \longrightarrow \bar{\tilde{s}}_R$ | $e^- + c \longrightarrow \tilde{s}_R$ | $e^- + \bar{s} \longrightarrow \bar{\tilde{c}}_L$ |
| 123 | $e^+ + b \longrightarrow \tilde{c}_L$ | $e^+ + \bar{c} \longrightarrow \bar{\tilde{b}}_R$ | $e^- + c \longrightarrow \tilde{b}_R$ | $e^- + \bar{b} \longrightarrow \bar{\tilde{c}}_L$ |
| 131 | $e^+ + d \longrightarrow \tilde{t}_L$ | $e^+ + \bar{t} \longrightarrow \bar{\tilde{d}}_R$ | $e^- + t \longrightarrow \tilde{d}_R$ | $e^- + \bar{d} \longrightarrow \bar{\tilde{t}}_L$ |
| 132 | $e^+ + s \longrightarrow \tilde{t}_L$ | $e^+ + \bar{t} \longrightarrow \bar{\tilde{s}}_R$ | $e^- + t \longrightarrow \tilde{s}_R$ | $e^- + \bar{s} \longrightarrow \bar{\tilde{t}}_L$ |
| 133 | $e^+ + b \longrightarrow \tilde{t}_L$ | $e^+ + \bar{t} \longrightarrow \bar{\tilde{b}}_R$ | $e^- + t \longrightarrow \tilde{b}_R$ | $e^- + \bar{b} \longrightarrow \bar{\tilde{t}}_L$ |

**Table 2.2:** *The squark production processes in $e^{\pm}p$ scattering.*

## 2.5.1 Resonant $\not{R}_p$ stop production

In this analysis, a search is performed for stop quarks which are produced resonantly in electron–proton scattering,

$$e^+ q \xrightarrow{\lambda'} \tilde{t}. \tag{2.46}$$

Here, $\lambda'$ indicates the $\not{R}_p$ process. At HERA, stop quarks with masses up to $\sim 290\,\text{GeV}$ can be produced which is close to the kinematical limit given by the centre–of–mass energy. According to equation 2.44, the resonant production of stop quarks and the $\not{R}_p$ decay of stop and sbottom quarks via a non–vanishing coupling $\lambda'_{131}$ are described by the Lagrangian

$$\mathcal{L}_{\not{R}_p} = -\lambda'_{131} e_L \tilde{t}_L \bar{d}_R + \lambda'_{131} \nu_{e,L} \tilde{b}_L \bar{d}_R + h.c., \tag{2.47}$$

where the indices $L$ and $R$ denote the left and right states of the fermionic fields and their corresponding scalar superpartners.

Since the $\not{R}_p$ stop interaction involves only the $\tilde{t}_L$ component of the fields (see equations 2.38 and 2.39), the production cross sections of the stop quarks $\tilde{t}_1$ and $\tilde{t}_2$ scale as [7]

$$\sigma_{\tilde{t}_1} \sim \lambda'^2_{131} d\left(x = \frac{M^2_{\tilde{t}_1}}{s}\right) \cos^2 \theta_{\tilde{t}} \quad \text{and} \tag{2.48}$$

$$\sigma_{\tilde{t}_2} \sim \lambda'^2_{131} d\left(x = \frac{M^2_{\tilde{t}_2}}{s}\right) \sin^2 \theta_{\tilde{t}}, \tag{2.49}$$

$d(x)$ being the probability of finding a $d$ quark in the proton with a momentum fraction $x = M^2_{\tilde{t}_{1,2}}/s$, where $M_{\tilde{t}_{1,2}}$ denotes the stop masses. The lighter state does not necessarily have the largest production cross section. However, in the SUSY parameter space investigated in this analysis, $M_{\tilde{t}_2}$
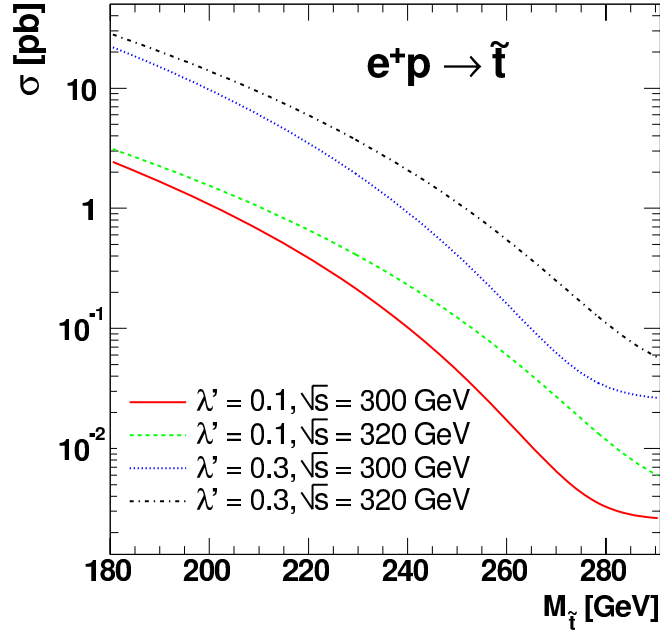
**Figure 2.8:** *The stop production cross sections for $\lambda'_{131} = 0.1$ and $\lambda'_{131} = 0.3$ at $\sqrt{s} = 301$ GeV and $\sqrt{s} = 319$ GeV as a function of the stop mass.*

is large enough to ensure that the resonant production of $\tilde{t}_2$ can be neglected. Therefore, in the following the notation $\tilde{t}$ will indicate the $\tilde{t}_1$. Figure 2.8 shows the stop production cross sections as a function of the stop mass for the example values $\lambda'_{131} = 0.1$ and $\lambda'_{131} = 0.3$ at the centre–of–mass energies $\sqrt{s} = 301$ GeV and $\sqrt{s} = 319$ GeV. The cross sections decrease with the stop mass. At one specific centre–of–mass energy, the cross sections for $\lambda'_{131} = 0.1$ and $\lambda'_{131} = 0.3$ differ by a factor of $9$ due to the $\sim \lambda'^2_{131}$ behaviour of the cross section (see equations 2.48 and 2.49).

## 2.5.2   Stop decays

Stop quarks can decay via their usual gauge couplings into neutralinos, charginos or gluinos, as described in section 2.4.2:

$$\tilde{t} \to t\tilde{g}$$
$$\tilde{t} \to t\tilde{\chi}^0_i \qquad\qquad\qquad (2.50)$$
$$\tilde{t} \to b\tilde{\chi}^\pm_i.$$

The decays into a top and a gluino or a neutralino are kinematically suppressed due to the high top mass $M_t \approx 174$ GeV. Searches for fermionic squark decays via their usual gauge couplings into neutralinos, charginos or gluinos are presented in [5]. In the present complementary analysis
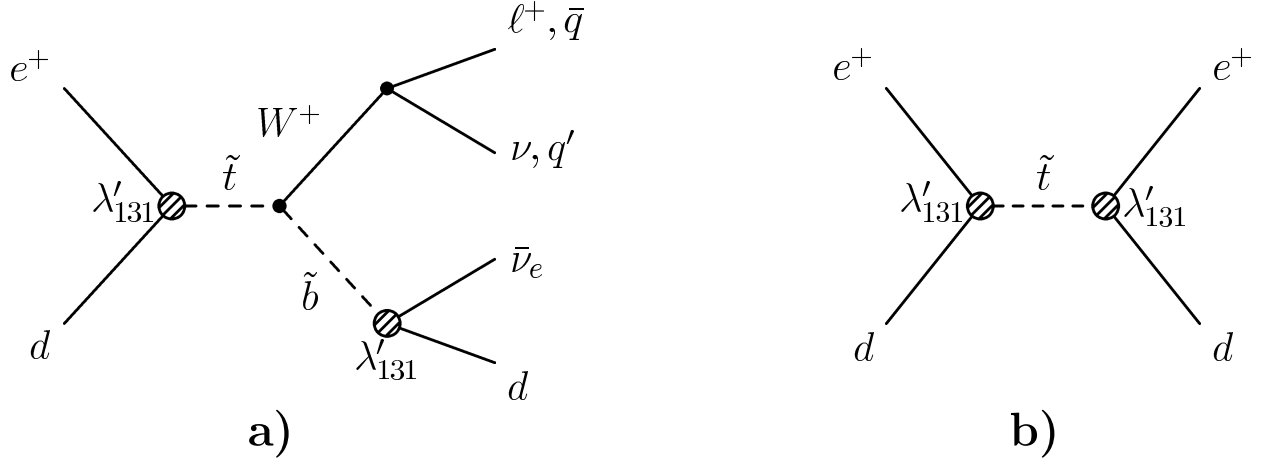
**Figure 2.9:** *The lowest order s–channel diagram for $\mathcal{R}_p$ stop production at HERA followed by a) the bosonic decay of the stop and b) the $\mathcal{R}_p$ decay of the stop.*
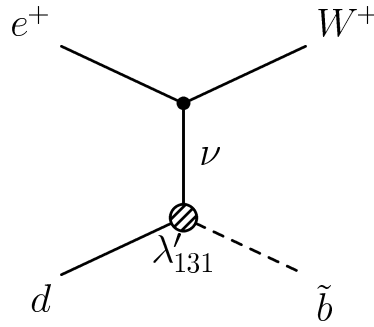


**Figure 2.10:** *The neutrino t–channel exchange for $\mathcal{R}_p$ stop production at HERA.*

the SUSY parameter space is chosen such that these decays are kinematically forbidden. It is moreover assumed that the sbottom quark $\tilde{b}_1$ (denoted by $\tilde{b}$) is lighter than the lightest stop, $M_{\tilde{b}} < M_{\tilde{t}}$, such that the only possible $R_p$ conserving decay mode is the *bosonic* stop decay

$$\tilde{t} \rightarrow \tilde{b}W^+ \tag{2.51}$$

with $W \rightarrow f\bar{f}'$ [7]. The corresponding diagram is shown in figure 2.9 a). The process $e^+d \rightarrow \tilde{b}W^+$ may also arise from the neutrino t–channel exchange illustrated in figure 2.10. Although the neutrino exchange is strongly suppressed with respect to the s–channel diagram, it is in principle taken into account in the present analysis.

Under the assumption that squark gauge decays into fermions are kinematically suppressed, the sbottom will subsequently undergo the $\mathcal{R}_p$ decay

$$\tilde{b} \xrightarrow{\lambda'} \bar{\nu}_e d. \tag{2.52}$$

| Channel | Decay process | Signature |
|---------|---------------|-----------|
| | $\tilde{t} \to \tilde{b}\, W$ $\overset{\lambda'}{\hookrightarrow} d\bar{\nu}_e$ | |
| $je\not{P}_\perp$ | $W \to e\nu_e$ $\to \tau\nu_\tau \to e\nu\nu\nu$ | jet $+\, e\, +\, \not{P}_\perp$ |
| $j\mu\not{P}_\perp$ | $W \to \mu\nu_\mu$ $\to \tau\nu_\tau \to \mu\nu\nu\nu$ | jet $+\, \mu\, +\, \not{P}_\perp$ |
| $jjj\not{P}_\perp$ | $W \to q\bar{q}'$ | 3 jets $+\, \not{P}_\perp$ |
| $ed$ | $\tilde{t} \overset{\lambda'}{\to} ed$ | jet $+$ high $P_T\, e$ |

**Table 2.3:** *The analysed stop decay channels in $\not{R}_p$ SUSY. The $\not{R}_p$ processes are indicated by the coupling $\lambda'$.*

In order to cover all $\not{R}_p$ decay modes in this particular scenario, in which decays of the light squarks into neutralinos and charginos are kinematically not possible, the $\not{R}_p$ decay into SM fermions,

$$\tilde{t} \overset{\lambda'}{\to} e^+ d, \tag{2.53}$$

is also considered. The corresponding diagram is shown in figure 2.9 b).

The four signatures considered in this analysis are given in table 2.3, with the corresponding diagrams shown in figure 2.9. The analysis includes both leptonic and hadronic $W$ decays and several final states can be investigated depending on the $W$ decay mode. Subsequent $\tau$ decays into leptons ($\tau\nu_\tau \to e\nu\nu\nu$ and $\tau\nu_\tau \to \mu\nu\nu\nu$) have a branching ratio of approximately 17% and are accounted for in the $je\not{P}_\perp$ channel and $j\mu\not{P}_\perp$ channel, respectively. The $W$ decay into $\tau\nu_\tau$, where $\tau \to$ hadrons $+\, \nu$ is not considered. The decay mode $\tilde{t} \to \tilde{b}W$ with $\tilde{b} \to \nu_e d$ and $W \to f\bar{f}'$ is experimentally investigated for the first time.

In figure 2.11, the stop decay widths $\Gamma(\tilde{t} \to \tilde{b}W)$, $\Gamma(\tilde{t} \to \tilde{b}\mu\nu)/10.8\%$ and $\Gamma(\tilde{t} \to ed)$ at $\lambda'_{131} = 0.1$ are illustrated for different sbottom masses as a function of the stop mass. The width $\Gamma(\tilde{t} \to \tilde{b}\mu\nu)$ is divided by $10.8\%$ to account for the branching ratio of the process $W \to \mu\nu$. Figure 2.12 shows the ratios of the stop decay widths $\Gamma(\tilde{t} \to \tilde{b}W^*)$ and $\Gamma(\tilde{t} \to ed)$ for different sbottom masses and $\not{R}_p$ couplings $\lambda'_{131}$, again as a function of the stop mass. Here, $W^*$ denotes a virtual $W$ boson. It is verified that the three–body decays via an off–shell $W$ ($M_{\tilde{t}} \lesssim M_{\tilde{b}} + 80\,\text{GeV}$) can be neglected compared with the $\not{R}_p$ decay of the stop. Thus, in this analysis only the mass region

$$M_{\tilde{t}} > M_{\tilde{b}} + M_W \tag{2.54}$$

is investigated, where the stop can decay into a sbottom and a real $W$ boson. Taking into account the lower bound from LEP on the sbottom mass, $M_{\tilde{b}} \gtrsim 90\,\text{GeV}$ [37], the mass range investigated
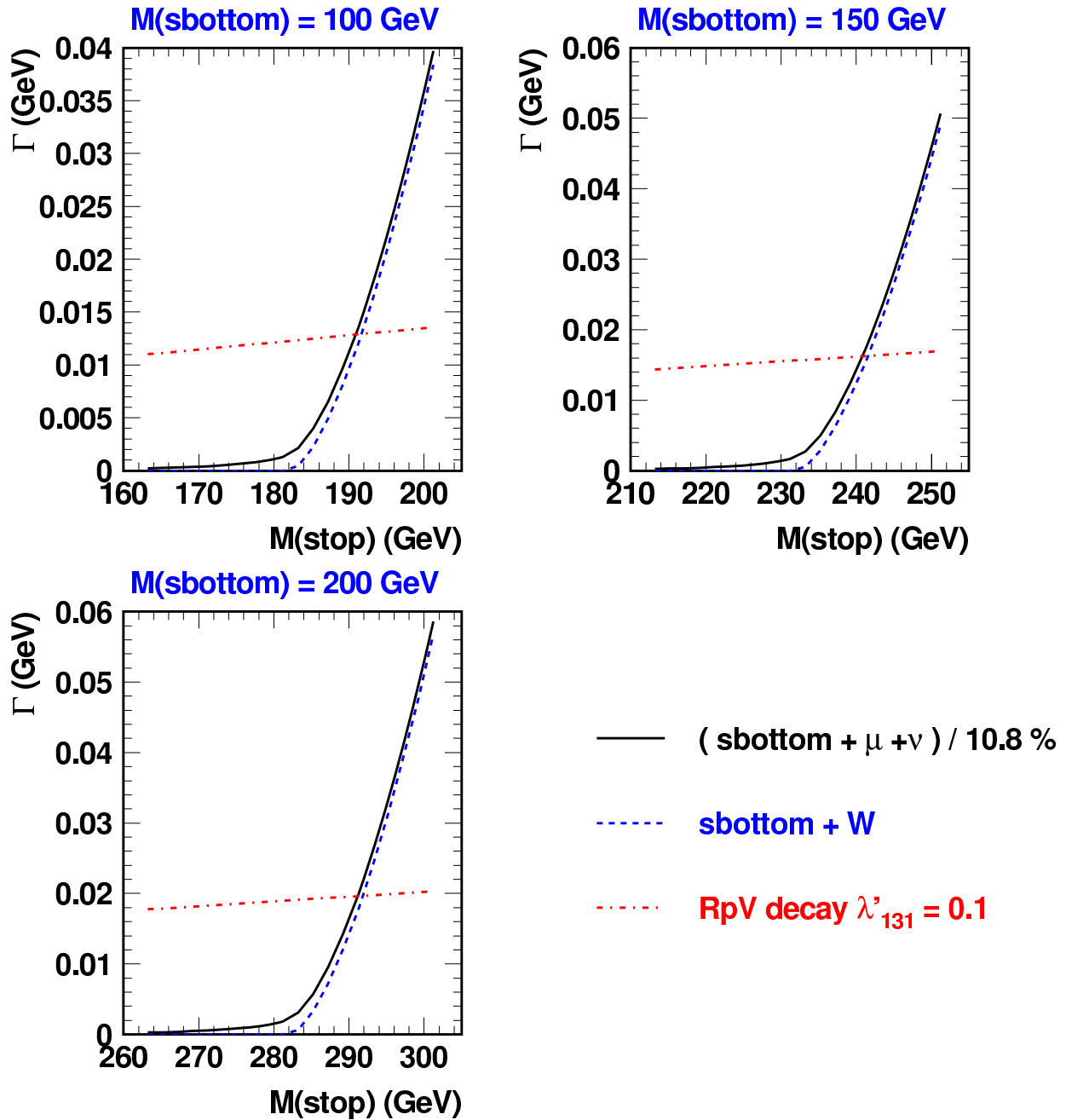
**Figure 2.11:**  *The stop decay widths for $M_{\tilde{b}} = 100\,GeV$ (top left), $M_{\tilde{b}} = 150\,GeV$ (top right) and $M_{\tilde{b}} = 200\,GeV$ (bottom left) as a function of the stop mass.*
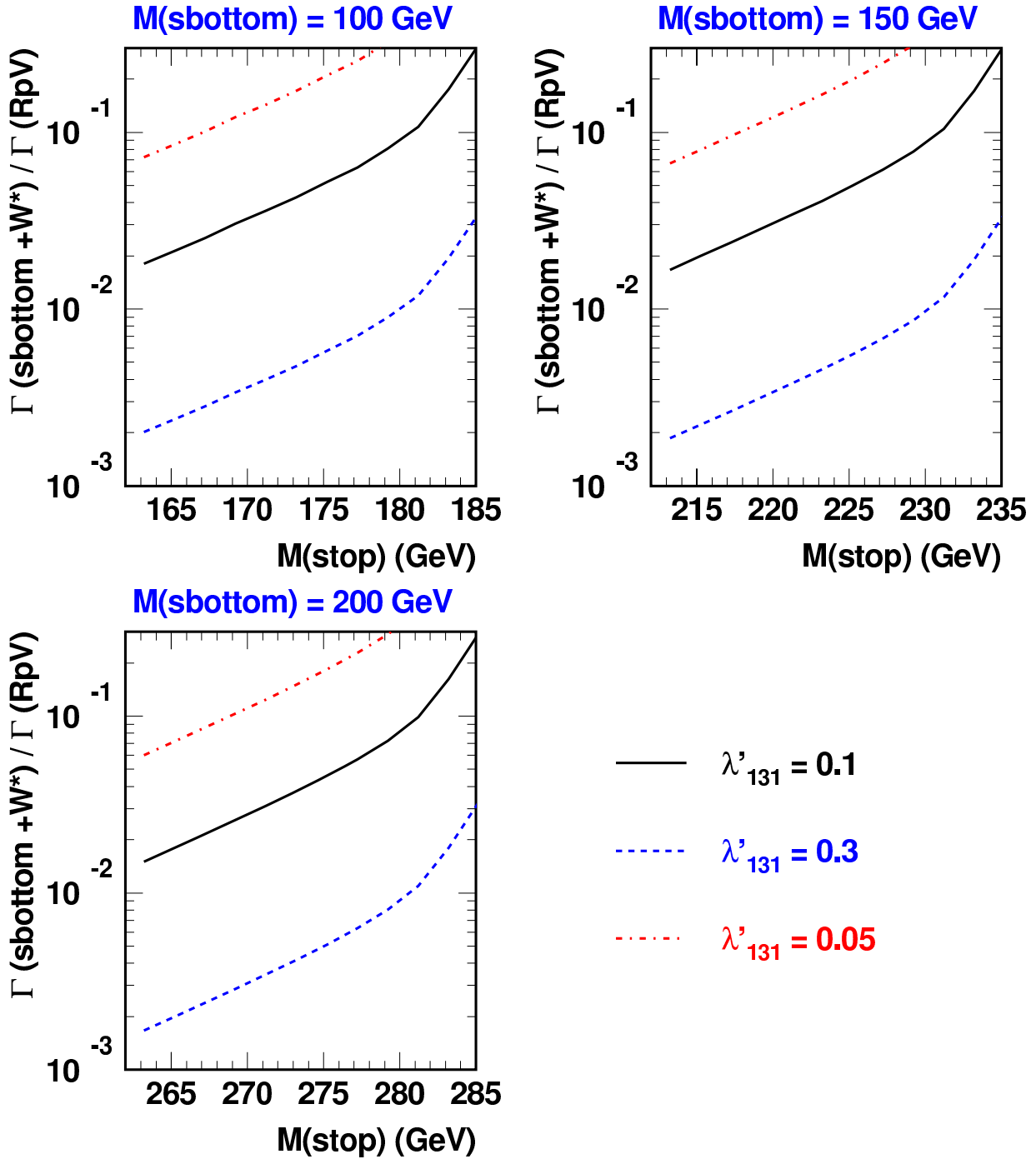
**Figure 2.12:** *The ratios of the bosonic and the $\not{R}_p$ stop decay widths for $M_{\tilde{b}} = 100$ GeV (top left), $M_{\tilde{b}} = 150$ GeV (top right), $M_{\tilde{b}} = 200$ GeV (bottom left) and different $\not{R}_p$ couplings $\lambda'_{131}$ as a function of the stop mass.*
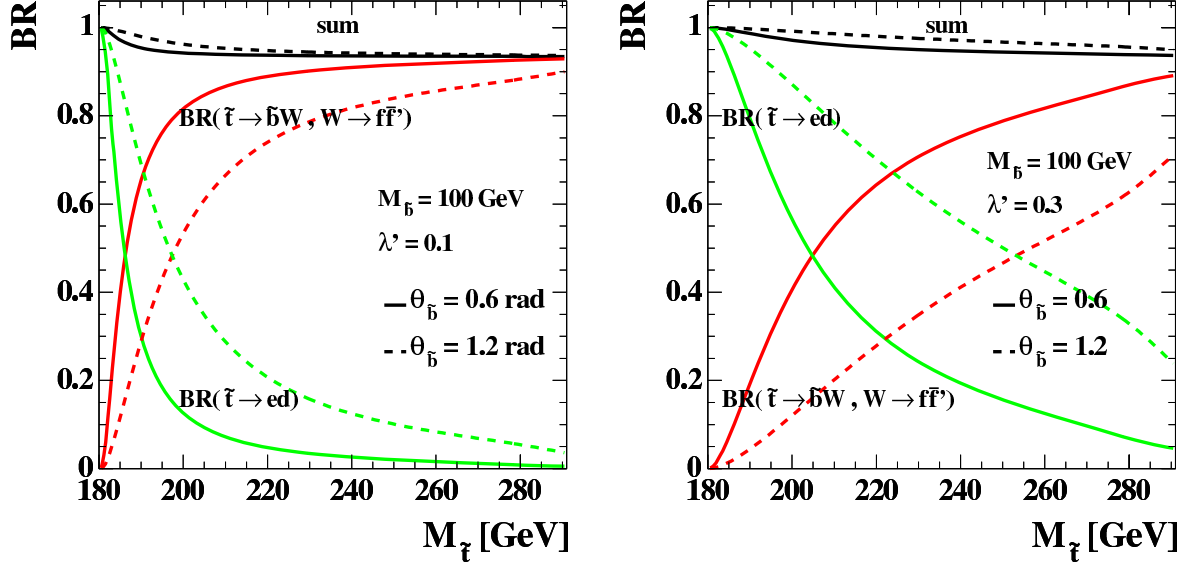
**Figure 2.13:** *Examples of the stop branching ratios as a function of the stop mass for $M_{\tilde{b}} = 100\,GeV$ at $\lambda'_{131} = 0.1$ (left) and $\lambda'_{131} = 0.3$ (right), when the fermionic decay modes of the stop via their usual gauge coupling are kinematically suppressed. The solid lines show the branching ratios for $\theta_{\tilde{b}} = 0.6\,rad$ and the dashed lines for $\theta_{\tilde{b}} = 1.2\,rad$. The dark lines indicate the branching ratios for the $\mathcal{R}_p$ stop decay, whereas the bright lines are the bosonic stop decay branching ratios. The sum of the branching ratios is less than one, since hadronic $\tau$ decays following $W \to \tau\nu_\tau$ are not considered here.*

in the present analysis is

$$180\,\text{GeV} \quad < M_{\tilde{t}} \quad < 290\,\text{GeV} \quad \text{and}$$
$$100\,\text{GeV} \quad < M_{\tilde{b}} \quad < 210\,\text{GeV}. \tag{2.55}$$

Moreover, it has been checked that the loop decay into a charm quark and a neutralino, when kinematically allowed, is negligible compared with the $\mathcal{R}_p$ stop decay for the values of $\lambda'_{131}$ which can currently be probed at HERA.

The branching ratio $BR_{\tilde{t}\to\tilde{b}W,W\to f\bar{f}'}$ for this decay mode depends only on the masses of the squarks involved, the $\mathcal{R}_p$ coupling $\lambda'_{131}$ and the mixing angle $\theta_{\tilde{b}}$. It is proportional to $\cos^2\theta_{\tilde{b}}$. This branching ratio is shown in figure 2.13 for example values of $\lambda'_{131}$ as a function of the stop mass. The sbottom mass is set to $M_{\tilde{b}} = 100\,\text{GeV}$ in these examples. For $\lambda'_{131} = 0.1$, the branching ratio $BR_{\tilde{t}\to\tilde{b}W,W\to f\bar{f}'}$ is large over a wide stop mass range, whereas for higher $\mathcal{R}_p$ couplings the branching ratio $BR_{\tilde{t}\to ed}$ gets more and more important. However, at high stop masses the bosonic stop decay is still the dominant process.

# 2.6 Monte Carlo event generation and simulation

In order to evaluate the SM expectation in all investigated selection channels, for each possible SM background source a detailed Monte Carlo simulation of the H1 detector response is performed. All processes are generated with an integrated luminosity much higher than that of the data (see table 2.4) and are described in the following.

- To determine the contribution of neutral current deep inelastic scattering events $ep \rightarrow ejX$, where $j$ indicates a jet, the RAPGAP [38] event generator is used. It includes the Born, QCD Compton and boson gluon fusion matrix elements. Higher order QCD radiative corrections are modelled using leading logarithmic parton showers [39]. The QED radiative effects arising from real photon emission and virtual electroweak corrections are simulated using HERACLES [40]. The parton density functions (PDF) in the proton are taken from the CTEQ5L [41] parameterisation.

- An important SM background for the bosonic stop decay channels is charged current deep inelastic scattering, which is simulated using DJANGO [42]. QCD radiation is implemented to first order via matrix elements, while higher orders are modelled by parton shower cascades generated using the colour–dipole model, as implemented in ARIADNE [43, 44]. Again, HERACLES is used for simulating first order electroweak corrections, as explained in the previous paragraph, and the CTEQ5L parameterisation is chosen to be the source for the proton PDFs.

- For the simulation of the direct and resolved photoproduction of jets, $ep \rightarrow (e)jjX$, the PYTHIA 6.1 [45] program is used, which includes light and heavy quark flavours. It contains the QCD Compton and boson gluon fusion matrix elements and radiative QED corrections. By calculating leading logarithmic parton showers, higher order QCD effects are considered. The photon PDFs are taken from [46], whereas the proton PDFs are taken from the CTEQ5L parameterisation.

- The most important SM background to the leptonic $W$ decay channels is the production of $W$ bosons, $ep \rightarrow eWX$, calculated in leading order (LO) using EPVEC [15]. Next–to–leading order (NLO) QCD corrections [47] are taken into account by reweighting the events as a function of transverse momentum and rapidity of the $W$ boson [48].

- The production of multi–lepton events, $ep \rightarrow \ell\ell X$, may also contribute to the SM background for the leptonic $W$ decay channels when one lepton is undetected and some fake missing transverse momentum is reconstructed. This process is generated with the GRAPE [49] program. In GRAPE, the cross section is calculated with the exact matrix elements at tree level.

- QED Compton scattering processes $ep \rightarrow e\gamma X$ are simulated with WABGEN [50], where the Monte Carlo package BASES [51] numerically calculates the cross section. The deep inelastic contribution of this processes is already included in RAPGAP.

In all models, processes with additional jets are taken into account by using leading logarithmic parton showers as a representation of higher order QCD radiation [52]. The predictions of the RAPGAP and PYTHIA models are scaled by a factor of $1.2$ for cases where three jets are required, *i.e.* in the $jjj\slashed{P}_\perp$ channel. This factor accounts for inadequacies in the parton shower model for multi–jet production and is obtained by comparison with data [53]. All SM Monte Carlo sets used in this analysis are listed in table 2.4.

For the SUSY signal simulation and the calculation of its cross section SUSYGEN [54, 55] is used. It relies on the LO amplitudes for $ed \rightarrow \tilde{b}W$ given in [7] and takes the stop width into account. The parton densities are taken from the CTEQ5L parameterisation and evaluated at the scale of the stop mass. In SUSYGEN, initial and final state parton showers are modelled using the DGLAP [56] evolution equations. For the non–perturbative part of the hadronisation, string fragmentation [57] is used.

All bosonic stop decay topologies are simulated for a wide range of stop and sbottom masses in a grid with steps of typically $20\,\mathrm{GeV}$. For the $\slashed{R}_p$ stop decay, only the stop mass is varied. A total of $1000$ events is simulated for each topology (and coupling). The events are passed through a detailed simulation of the H1 detector. These simulations allow the determination of signal detection efficiencies as a function of the stop (and sbottom) masses in the entire phase space since the mass steps are sufficiently small for linear interpolations to be used. The variation of the efficiencies with the coupling $\lambda'_{131}$, when the stop mass and width are both large, is also taken into account.

# 2.7  Analysis strategy

All four final state topologies listed in table 2.3 are investigated in order to exploit the sensitivity of HERA for the resonant production of stop quarks and their bosonic decays. The event selection of these final state channels is described in chapter 5. The selection is performed in order to maximise the signal sensitivity; events which could arise from bosonic stop decays are selected, whereas the SM background is suppressed. The error on the SM expectation is defined by experimental and theoretical uncertainties (see section 4.8).

To avoid double counting of a hypothetical signal, for the limit derivation (chapter 6.4) the selection of all topologies must be exclusive. Although the selection cuts are not explicitly exclusive, it is ensured by these cuts that double counting occurs in less than $0.1\%$ of the events and is therefore negligible.

The spectra of the reconstructed or – in case of more than one neutrino in the final state – the transverse stop mass of data and SM Monte Carlo are differentially compared. No significant

| Process(es) | Model | Phase space | Subprocess | $\mathcal{L}_{\mathrm{MC}}/\mathcal{L}_{\mathrm{data}}$ |
|---|---|---|---|---|
| Photoproduction | PYTHIA61 | $\hat{P}_T > 10\,\mathrm{GeV}$ | | 1.5 |
| | | $\hat{P}_T > 15\,\mathrm{GeV}$ | | 15 |
| | | $\hat{P}_T > 25\,\mathrm{GeV}$ | | 150 |
| | | $\hat{P}_T > 40\,\mathrm{GeV}$ | | 150 |
| | | $\hat{P}_T > 75\,\mathrm{GeV}$ | | 2200 |
| | | $\hat{P}_T > 95\,\mathrm{GeV}$ | | 75000 |
| Prompt Photon | PYTHIA61 | $\hat{P}_T > 76\,\mathrm{GeV}$ | | 75 |
| | | $\hat{P}_T > 20\,\mathrm{GeV}$ | | 500 |
| | | $\hat{P}_T > 40\,\mathrm{GeV}$ | | 20000 |
| NC | RAPGAP | $Q^2 > 4\,\mathrm{GeV}^2$ | | 10 |
| | | $Q^2 > 100\,\mathrm{GeV}^2$ | | 7 |
| | | $Q^2 > 400\,\mathrm{GeV}^2$ | | 40 |
| | | $Q^2 > 1000\,\mathrm{GeV}^2$ | | 12 |
| | | $Q^2 > 2500\,\mathrm{GeV}^2$ | | 27 |
| | | $Q^2 > 5000\,\mathrm{GeV}^2$ | | 100 |
| | | $Q^2 > 10000\,\mathrm{GeV}^2$ | | 540 |
| | | $Q^2 > 20000\,\mathrm{GeV}^2$ | | 9600 |
| CC | DJANGOH12 | $Q^2 > 100\,\mathrm{GeV}^2$ | | 245 |
| | | $Q^2 > 10000\,\mathrm{GeV}^2$ | | 13000 |
| Lepton Pair Production | GRAPE | | $ee$ | 450 |
| | | | $\mu\mu$ | 750 |
| | | | $\tau\tau$ | 1500 |
| QED Compton | WABGEN | $M_{e\gamma} > 10\,\mathrm{GeV}$ | | 10 |
| | | $M_{e\gamma} > 50\,\mathrm{GeV}$ | | 340 |
| | | $M_{e\gamma} > 100\,\mathrm{GeV}$ | | 5000 |
| W Production | EPVEC | | | 1500 |

**Table 2.4:** *The Monte Carlo samples used in the presented analysis. All processes are simulated separately for proton energies of* $820\,GeV$ *and* $920\,GeV$*. For the ratio* $\mathcal{L}_{\mathrm{MC}}/\mathcal{L}_{\mathrm{data}}$*, the smallest value found is given.*

deviation from the SM is observed (see chapter 6.1). Hence, the results of the event selections are used to set constraints on the parameters of the MSSM.

In order to obtain these exclusion limits, the stop signal selection efficiencies must be determined for each considered stop decay mode separately as a function of the stop (and sbottom) mass and the $\mathrm{R}_p$ coupling $\lambda'_{131}$. Furthermore, the branching ratios of the stop decay modes and the stop masses are calculated for each set of variables in the SUSY parameter space. The number of observed and expected events, the branching ratios and the selection efficiencies are used to calculate an upper limit on the number of events which might arise from a stop signal. Finally, a multi–dimensional scan of the SUSY parameter space is performed. This scan accounts for the fact that several SUSY parameters are relevant for the limit derivation.

# 3

# The H1 Experiment at HERA

This chapter gives a short overview of the electron–proton collider HERA at the DESY[1] [58] laboratory in Hamburg. Moreover, the H1 detector components which are relevant to the present analysis are briefly described here.

## 3.1   The HERA collider

The HERA collider is a facility built to study the nature of high energy electron–proton scattering. HERA consists of one storage ring for electrons and one for protons. Both rings have a circumference of $6.3$ km and are located in a tunnel $10$ m $- 15$ m under ground.

Circulating in opposite directions in the rings, the beam particles (electrons and protons) collide at two interaction regions. This offers the possibility of studying electron–proton collisions with the detectors H1 [59] and ZEUS [60] which have been constructed for this purpose. In addition, the fixed target experiment HERMES [61] makes use of the electron beam only. The HERA–B [62] experiment has been operated using the proton beam only. The HERA collider, its pre–accelerator facilities and the location of the experiments are illustrated in figure 3.1.

The electrons and protons are stored in up to $220$ bunches. Each bunch contains about $10^{10}$ to $10^{11}$ particles. The bunch crossing frequency of $10.4$ MHz leads to a time interval of $96$ ns between two subsequent bunch crossings. The electron ring consists of superconducting cavities and conventional magnets, whereas the proton ring is made of normal conducting radio frequency cavities and superconducting magnets.

Between 1994 and 1997, HERA was operated with positrons of energy $E_e^0 = 27.5$ GeV and protons of energy $E_p^0 = 820$ GeV. In 1998, the proton energy was increased to $E_p^0 = 920$ GeV and until the beginning of 1999, HERA ran with electrons. From summer 1999 until autumn

---
[1]Deutsches Elektronen–Synchrotron
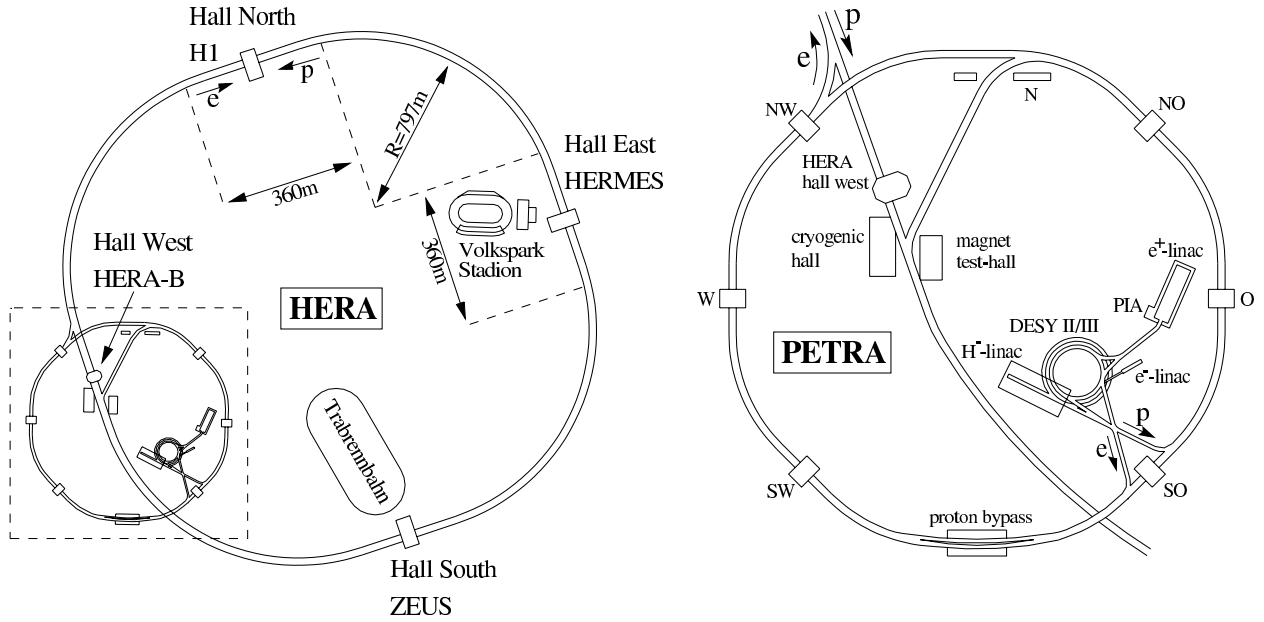
**Figure 3.1:** *A schematic overview of the electron–proton collider HERA at DESY with an enlarged view of the pre–accelerator system (right).*

2000, HERA was again operated with positrons. This has been the last data taking period of HERA I. According to Equation 2.9, the centre–of–mass energy of the colliding electrons and protons at HERA is

$$\sqrt{s} = \sqrt{4E_e^0 E_p^0} = \begin{cases} 319\,\text{GeV} & \text{for } E_p^0 = 920\,\text{GeV} \\ 301\,\text{GeV} & \text{for } E_p^0 = 820\,\text{GeV.} \end{cases} \tag{3.1}$$

In this analysis, all data collected with the H1 detector in positron–proton scattering in the years 1994 − 1997 and 1999/2000 are used.

## 3.2   The H1 detector

The H1 detector is located in the north interaction region of the HERA collider. It is a multi–purpose apparatus designed to study the complete final state in high energy $ep$ collisions. An isometric view of the H1 detector is illustrated in figure 3.2.

The centre–of–mass of the incoming beam particles is boosted in the proton direction due to the imbalance of the beam energies. Therefore, the H1 detector is constructed asymmetrically. Moreover, almost the total solid angle ($4\pi$) around the beam axis is covered by H1 detector components, except for the lead–through of the beam pipe. The H1 detector is described in detail in [59, 63, 64].

**HERA Experiment H1**

| | | | | |
|---|---|---|---|---|
| [1] | Beam pipe and beam magnets | | [9] | Muon chambers |
| [2] | Central tracking chambers | | [10] | Instrumented Iron (iron stabs + streamer tube detectors) |
| [3] | Forward tracking and Transition radiators | | [11] | Muon toroid magnet |
| [4] | Electromagnetic Calorimeter (lead) | } Liquid Argon | [12] | SpaCal |
| [5] | Hadronic Calorimeter (stainless steel) | | [13] | Plug calorimeter (Cu, Si) |
| [6] | Superconducting coil (1.2T) | | [14] | Concrete shielding |
| [7] | Compensating magnet | | [15] | Liquid Argon cryostat |
| [8] | Helium cryogenics | | | |

**Figure 3.2:** *The H1 detector.*

## The coordinate system

The right–handed coordinate system used is centred on the nominal interaction point ($z = 0$) with the positive $z$–direction defined to be along the incident proton beam. The positive $x$–axis is the direction towards the HERA ring centre and the positive $y$–axis is the upward direction. The $(x, y)$–plane corresponds to the *transverse* plane.

The polar angle $\theta$ is defined according to the $z$–direction such that $\theta = 0°$ points to the proton direction and $\theta = 180°$ to the electron direction. The azimuthal angle $\phi = 0°$ is defined according to the positive $x$–direction.

## 3.2.1   Tracking

The tracking system builds the innermost part of the H1 detector and covers the angular range $7° < \theta < 177.5°$ with full azimuthal acceptance. It consists of the central tracking detector and the forward tracking detector. These detector components are used to measure charged particle trajectories, to reconstruct the interaction vertex and to supplement the measurement of the hadronic energy (see section 3.2.2). This central part of the detector is surrounded by a superconducting magnetic coil with a strength of $1.15$ Tesla. The magnetic field is provided homogeneously along the $z$–axis and is used for momentum measurement.

## The central tracking system

The central tracking system covers the polar angle range $15° < \theta < 165°$. It consists of concentric cylindrical drift and proportional chambers with their axis being the beam–axis.

- The innermost part of the tracking system is build by the central silicon tracker (CST). The two layers of silicon strip detectors have a radius of $r = 5.75$ cm and $r = 9.75$ cm, respectively. They are able to provide a high precision measurement of track trajectories which is exploited to obtain precise information about the track quantities and the vertex position.

- The track measurements in the two central jet chambers, CJC1 and CJC2, have spatial resolutions which differ in the $r-\phi$ –plane and the $z$–direction. The resolution is $\sigma_{r\phi} = 140\,\mu$m in the $r-\phi$ –plane, whereas the precision of the measurement of the $z$–coordinate is only $\sigma_z = 2.2$ cm. In the magnetic field, the curvature of charged tracks gives their transverse momentum $P_T$. It is measured with a resolution of $\sigma(P_T)/P_T = 0.01 \cdot P_T$ GeV.

- A more precise measurement of the $z$–coordinate is provided by the two thin drift chambers CIZ and COZ. These $z$–chambers consist of sense wires fixed perpendicular to the $z$–direction. The resolution of their measurement is $\sigma_z \approx 350\,\mu$m.

- The multi wire proportional chambers CIP and COP complement the $z$–chambers. They provide fast trigger signals with a resolution of $21$ ns.

## The forward tracking system

The forward tracking detector consists of three *supermodules* which are located around the $z$–coordinate in the polar angle range $7° < \theta < 25°$. Each supermodule consists of four sub-detectors: three planar drift chambers which provide a precise measurement of $\theta$, the forward multiwire proportional chamber, a transition radiation detector and a radial drift chamber which also deliver a good $r - \phi$ measurement.

## 3.2.2 Calorimetry

The tracking system of the H1 detector (see section 3.2.1) is surrounded by the calorimetry system. The liquid argon calorimeter (LAr) is used to identify jets and electrons and covers the polar angle range $4° < \theta < 154°$ with full azimuthal acceptance. Furthermore, it measures the energies of electromagnetic and hadronic objects. The energy measurement is complemented by a calorimeter in the backward region, the spaghetti calorimeter (SPACAL). Before the 1994/1995 shutdown, the LAr calorimeter was complemented with the backward electromagnetic calorimeter (BEMC) which was then replaced by the SPACAL calorimeter. The tail catcher is able to supplement the energy measurement on the outside of the inner calorimeters. It is implemented in the iron return yoke.

## The liquid argon calorimeter

The LAr calorimeter is a sampling calorimeter which provides a good electron recognition. Its position inside the superconducting magnetic coil minimises the passive material in front of the calorimeter. Along the $z$–direction, the LAr calorimeter is divided into eight *wheels*. These wheels are labelled as BBE, CB1, CB2, CB3, FB1, FB2, OF and IF and each of them is subdivided in $\phi$ into eight *octants*.

Moreover, the LAr calorimeter is divided into an electromagnetic and an hadronic section:

- The electromagnetic energy is measured in the inner section of the LAr calorimeter.

  The absorbing material of this calorimeter section is lead and the active material filled into the gaps is liquid argon. The total depth of the electromagnetic LAr section is dependent on $\theta$ and varies between $20$ and $30$ radiation lengths. It has an energy resolution of $\sigma(E)/E \approx 12\%/\sqrt{E/\,\mathrm{GeV}} \oplus 1\%$, as obtained in test beam measurements [65, 66, 67]. The electromagnetic energy scale uncertainty of the LAr calorimeter varies between $0.7\%$ and $3\%$ (see chapter 4.5).

- The hadronic energy is measured in the outer section of the LAr calorimeter.

  Here, steel is used as absorbing material and again the active material filled into the calorimeter section is liquid argon. The total depth of this calorimeter section varies between $5$ and $8$ hadronic interaction lengths. The response of the LAr calorimeter to hadrons is

approximately $30\%$ smaller than to electrons of the same energy. This non–compensating behaviour of the calorimeter is adjusted by an off–line reweighting technique. The hadronic LAr calorimeter section has an energy resolution of $\sigma(E)/E \approx 50\%/\sqrt{E/\,\mathrm{GeV}} \oplus 2\%$ for hadrons. The hadronic energy scale uncertainty amounts to $2\%$ (see chapter 4.6).

## The SPACAL calorimeter

In the backward region, the LAr calorimeter is complemented by the *spaghetti* calorimeter, SPACAL [68]. It is a scintillating fibre calorimeter which has lead absorbers and covers the angular range $153° < \theta < 177.8°$.

Similar to the LAr calorimeter, the SPACAL consists of an electromagnetic and a hadronic part. It provides an electromagnetic energy resolution of $\sigma(E)/E \approx 7.1\%/\sqrt{E/\,\mathrm{GeV}}$ [69].

## 3.2.3   The muon system

The Muon system of the H1 detector consists of the central and endcap muon detector which situated in the iron return yoke. It is supplemented by the forward muon detector which uses a toroidal magnetic field. With these detectors, the identification of muons is possible. Furthermore, they provide a measurement of the muon direction and momentum.

## The central muon detector

The iron return yoke is the outermost part of the detector and is equipped with streamer tubes to form the central and endcap muon detector in the polar angle range $4° < \theta < 171°$. Some of the up to sixteen tube layers are equipped with pad electrodes which supplement the energy measurement of hadrons not being completely absorbed in the inner calorimeters (*tail catcher*). This means that the instrumented iron could also act as a backing calorimeter. However, the tail catcher is only used for the muon detection (see section 4.3.2) in this analysis.

The central muon detector is segmented into $64$ modules, each being instrumented with $10$ layers of streamer tubes. Three additional streamer tube layers, the *muon boxes*, are mounted at each side of the instrumented iron such that they cover the edges of the central muon detector. Thus, the muon boxes improve the track measurement in these detector regions.

In the central muon detector, the muon position perpendicular to the wires is measured by the signal wires in the streamer tubes. The resolution of the measurement varies between $3$ mm and $4$ mm. The muon position parallel to the wires is measured by strip electrodes. These strip electrodes are situated in five of the streamer tube layers. Their resolution varies between $10$ mm and $15$ mm.

## The forward muon detector

The forward muon detector is situated in the forward direction and covers the polar angle range $3° < \theta < 17°$. Outside the main detector, the toroidal magnet provides a field of $1.6$ Tesla. The

spectrometer consists of six double layers of drift chambers which are located on both sides of the magnet. The orientation of the drift chamber planes is chosen such that four of the layers provide an optimal measurement in $\theta$ and two of the layers measure accurately in $\phi$. Muons can only be identified in the forward muon detector if they have a momentum $P > 5\,\text{GeV}$. Else, the muons cannot be distinguished from energy losses in the inner detectors and the toroid.

## 3.2.4 Luminosity measurement

The luminosity is determined from the rate of the Bethe–Heitler process $ep \rightarrow ep\gamma$ (elastic bremsstrahlung process) which has a large and well known cross section. The filling of new electron and proton bunches into the HERA ring defines a luminosity fill. Each luminosity fill is divided into *runs*[2] and for each run the luminosity is measured separately. For this purpose, the final state photon is detected – in coincidence with the electron – in a calorimeter which is located downstream of the interaction point at $z = -102.9$ m.

## 3.2.5 The H1 trigger system

The H1 trigger system is able to separate events of physics interest from background events. At HERA, the bunch crossing rate is about $10.4$ MHz. In contrast, the H1 data is taken with a rate of only approximately $15$ Hz. The background event rate amounts to about $50$ kHz, dominated by beam–gas or beam–wall events, beam–halo muons and muons coming from cosmic showers. Physics processes have a rate of about $20$ Hz – $30$ Hz; processes with high transverse energies can be observed only very rarely (*e.g.* once a day).

The readout system is not able to record the whole detector information for each bunch crossing. Therefore, a trigger system was designed which reduces the readout rate by providing a fast decision of keeping or rejecting an event at four levels, L1 to L4.

- The L1 trigger level is a dead time free system and filters the physics events within $2.3\,\mu$s. The subdetectors which are used by this first level trigger are called (*trigger elements*). As long as trigger information from some trigger elements is missing, the event information is stored in a pipeline. This procedure is necessary due to the short bunch crossing time of $96$ ns. The trigger elements are combined to $128$ *subtriggers* by the central trigger logic. If the decision of one of these subtriggers is positive, the pipeline is interrupted. The trigger data are then submitted to the second trigger level.

- The L2 trigger level provides a decision within $20\,\mu$s. In this time, the L1 decision can be verified by combining signals from different subdetectors. For this purpose, topological correlations and techniques including neural networks are used. If the L2 trigger level

---

[2]A run can last up to two hours and its quality (good, medium, bad or unknown) is given by the detector status.

accepts an event, the detector readout starts and the data are transfered to the L4 trigger level.

- The trigger level L3 has not been used so far.

- At the L4 trigger level, a fast event reconstruction is performed by a processor farm, using the entire detector information. The events filtered by subsequent decision algorithms are finally written to tape with a data taking rate of approximately $15$ Hz.

# 4
# Data Selection

This analysis uses the data collected with the H1 detector in electron–proton scattering in the years 1994 to 2000 at centre–of–mass energies of $\sqrt{s} = 301\,\text{GeV}$ and $\sqrt{s} = 319\,\text{GeV}$, corresponding to a total integrated luminosity of $105.8$ pb$^{-1}$. Only good or medium quality runs are selected in order to ensure that only events arising from $ep$ collisions are considered. In these runs, all important subsystems were operational. Moreover, several requirements to reject non–$ep$ background are applied. The basic data selection is used in common with the general search for new phenomena in $ep$ scattering at HERA [52, 70, 71].

The data selection for the event topologies considered in this analysis relies on the identification of jets, leptons and missing transverse momentum. Therefore, in this chapter the identification and measurement of these objects is described. Furthermore, the reconstruction methods of kinematics which are needed for the electron energy calibration and the further event selection are summarised. Finally, the trigger efficiencies are given and the treatment of systematic uncertainties are characterised.

## 4.1   Background rejection

In order to significantly reduce background events not coming from electron–proton collisions, several requirements on event topologies and the the event timing are applied. The basic event selection criteria are given in table 4.1.

- The primary interaction vertex has to be reconstructed within $35\,\text{cm}$ in $z$ of the nominal position of the vertex: $-36\,\text{cm} < z_{vtx} < 34\,\text{cm}$ in the 1994–1997 data sample and $-35\,\text{cm} < z_{vtx} < 35\,\text{cm}$ in the 1999/2000 $e^{+}p$ data sample.

- To describe the reconstructed momentum loss in the direction of the incident electron, the

| **1994–1997 and 1999/2000 $e^+p$ reprocessed data, 105.8 pb$^{-1}$** |
|---|
| good and medium runs<br>full functionality of subsystems:<br>LAr, CJC1 and CJC2, luminosity system, SPACAL, central muon detector, COP |
| $-36\,\text{cm} < z_{vtx} < 34\,\text{cm}$ in 1994–1997 data sample<br>$-35\,\text{cm} < z_{vtx} < 35\,\text{cm}$ in $1999e^+/2000$ data sample<br>$\|\Delta T_0\| < 11.4$ ns<br>QBGFMAR bits 0 – 8 false for all channels (except channels containing a $\mu$)<br>QBGFMAR bits 0 – 9 false for channels containing a $\nu$ (except channels containing a $\mu$) |

**Table 4.1:** *The basic event selection criteria.*

observable

$$\sum_i (E_i - P_{z,i}) = \sum_i (E_i(1 - \cos\theta_i)) \tag{4.1}$$

is introduced, where $E_i$ is the energy and $P_{z,i}$ is the $z$ component of the particle momentum. The index $i$ runs over all hadronic and electromagnetic objects and muons. A neutral current DIS event is expected to have twice the energy of the incident electron, $\sum_i (E_i - P_{z,i}) = 2E_e^0 = 55.2\,\text{GeV}$, due to energy and momentum conservation. This value is achieved if all final state particles in $ep$ collisions are detected or if only longitudinal momentum along the positive $z$–direction remains undetected. Because larger values of $\sum_i (E_i - P_{z,i})$ could arise from non–$ep$ background from mismeasurement, it is required that $\sum_i (E_i - P_{z,i}) < 75\,\text{GeV}$. Lower cuts on this observable are dependent on the final state investigated (see sections 4.3.4 and 5.3).

- The H1 software package QBGFMAR [72] comprises 26 background finders which are used to reject non–$ep$ background events. These background finders search for event topologies typical of cosmic ray and beam–induced background [13]. Since in the channels which contain a muon (*i.e.* the $j\mu\rlap{/}{P}_\perp$ channel) the background finders are inefficient [73], they are not considered here.

- The event timing $T_0$ is required to be consistent with the $ep$ bunch crossing. It must satisfy $\|\Delta T_0\| < 11.4$ ns.

| Period | $\mathcal{L}_{int}$ total raw [pb$^{-1}$] | $\mathcal{L}_{int}$ final [pb$^{-1}$] |
|---|---|---|
| 1994 $e^+$ | 3.17 | 2.81 |
| 1995 $e^+$ | 5.88 | 4.39 |
| 1996 $e^+$ | 9.83 | 8.50 |
| 1997 $e^+$ | 27.92 | 22.20 |
| 1999 $e^+$ | 24.78 | 18.89 |
| 2000 $e^+$ | 59.26 | 49.04 |

**Table 4.2:** *The integrated luminosities for the 1994–2000 $e^+p$ data sample. The total and final integrated luminosity amounts to $105.8$ pb$^{-1}$.*
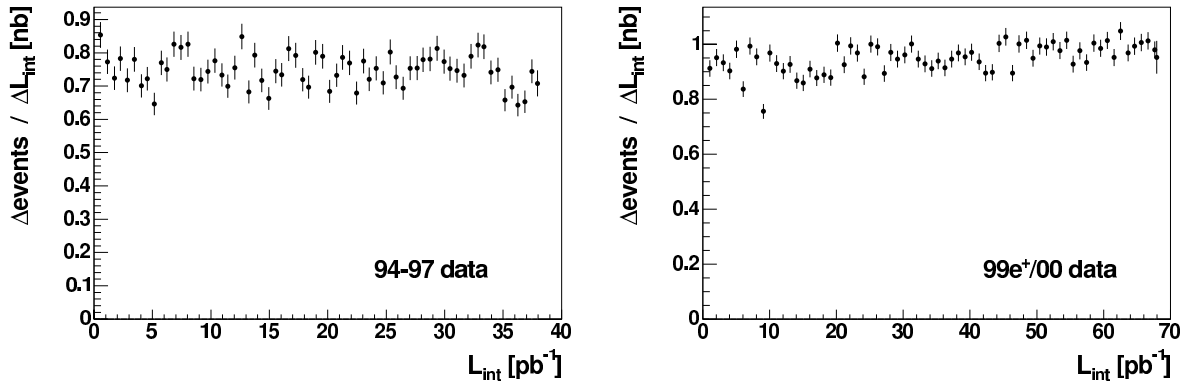


**Figure 4.1:** *The number of selected events per luminosity interval as a function of the accumulated luminosity for the 1994–1997 data sample (left) and the 1999/2000 $e^+p$ data sample (right).*

# 4.2 Luminosity determination

The total raw luminosity is reduced by the requirements on the run quality. Moreover, it is affected by the correction for the functionality of the subsystems (HV correction) and for sattelite bunches ($z_{vtx}$ correction). For the 1994–2000 $e^+p$ data sample, the final total integrated luminosity amounts to $105.8$ pb$^{-1}$. The integrated luminosities as determined for this analysis for the six run periods are listed in table 4.2. In figure 4.1, the number of selected events per luminosity interval is shown as a function of the accumulated luminosity for the 1994–1997 (left) and the 1999/2000 $e^+p$ (right) data samples. The slight drop in the 1999/2000 $e^+p$ data sample distribution around $15$ pb$^{-1}$ to $20$ pb$^{-1}$ is caused by broken CJC wires in the second part of the 1999 $e^+p$ run period. These CJC inefficiencies are taken into account within the MC simulation.

# 4.3  Particle identification

The selection of the event topologies as given in table 2.3 rely on the identification of jets, leptons and missing transverse momentum. Identification criteria for electrons, muons and jets are based on previous analyses performed on specific final states [52, 70, 71, 13] and are described in the following sections. Although the basic data selection is the same as in [52, 70, 71], the definition of the particles is slightly different in order to increase the sensitivity to the stop signal.

## 4.3.1  Electron identification

The electron identification is based on the measurement of a compact and isolated electromagnetic shower in the LAr calorimeter which is associated to a high quality track if $\theta_e > 10°$. Here, $\theta_e$ denotes the electron polar angle. Detailed studies can be found in [71, 74] and references therein. The electron finder QESCAT [75], which is implemented in the physics analysis library H1PHAN [76], contains the search algorithm QECFWD [77]. This algorithm is used in order to identify electron candidates. The requirements on these electron candidate are:

- The electron candidate must have a transverse momentum of at least $10\,\text{GeV}$ and must be found in the polar angle range $5° < \theta_e < 140°$.

- The hadronic energy within a cone defined by $R = \sqrt{(\Delta\eta)^2 + (\Delta\phi)^2} < 0.5$ around the electron is required to be below $2.5\%$ of the electron energy ($E_{R=0.5}/E_e < 2.5\%$). Here, $\eta = -\ln(\tan(\theta/2))$ is the pseudorapidity and $\phi$ denotes the azimuthal angle.

- In the region $10° < \theta_e < 140°$, a high quality track is also required to be associated to the electromagnetic cluster.

  Furthermore, a geometrical matching between the track and the cluster centre–of–gravity is required; their distance of closest approach ($DCA_{cl}^{tk}$) must be less than $12\,\text{cm}$. The BOS [78] banks DTRA and DTNV contain vertex fitted and non–vertex fitted tracks, respectively. Tracks from both banks are considered in this analysis.

- Detector regions, in which the electron candidate measurements are not reliable, such as cracks between calorimeter modules ($\phi$–cracks) or wheels ($z$–cracks) must be excluded from the analysis: $|\phi^e - \phi_{crack}| > 2°$ and $|z^e - z_{crack}| > 2$ cm.

- The starting radius of the electron track, $R_{start}$, is defined as the transverse distance between the first measured point in the central drift chambers and the beam axis. If the electron candidate is detected in the region $20° < \theta_e < 140°$ or if the expected radial track length, $l_{track}$, in the CJC is larger than $10$ cm, $R_{start}$ is required to be below $30\,\text{cm}$. This cut allows efficient rejection of photons which convert late in the central tracker material.

- Due to hardware problems, the CJC was inefficient in the data taking period 1997 $e^+p$ within the interval $230° \lesssim \phi \lesssim 250°$. In the data taking period 1999 $e^+p$ the interval $190° \lesssim \phi \lesssim 280°$ was affected. In these periods and $\phi$–regions, tracks cannot be reconstructed in the CJC. Thus, the affected data samples, corresponding to integrated luminosities of $\sim 21\,\mathrm{pb}^{-1}$ and $\sim 8\,\mathrm{pb}^{-1}$ [71], respectively, are not considered in the electron candidate identification.

The electron selection criteria are listed in table 4.3. The resulting electron identification efficiency is around $85\%$ in the forward region and varies between $92\%$ and $98\%$ in the central region [71].

## 4.3.2   Muon identification

The muon identification is based on the measurement of a track segment or an energy deposit in the instrumented iron associated with a charged particle track in the inner tracking systems. In addition, a track solely measured in the forward muon detector is taken as a muon candidate, if its polar angle is $\theta_\mu < 12.5°$. The muon momentum is measured from the track curvature in the solenoidal or toroidal magnetic field. In the forward and central tracking systems the track selection is based on standard quality requirements which are described in [70]. The main requirements on the muon candidate are:

- The muon candidate must have a transverse momentum of at least $10\,\mathrm{GeV}$ and must be found in the polar angle range $10° < \theta_\mu < 140°$.

- To reduce hadronic background, the distance between the muon candidate and the nearest high quality track is required to be $R^{gtk} > 0.5$.

- A cylinder of radius $R = 0.5$ is centred around the muon direction associated with its track. Within this radius, a muon candidate should not deposit more than $8\,\mathrm{GeV}$ in the LAr calorimeter: $E^{LAr}_{R=0.5} < 8\,\mathrm{GeV}$. This calorimetric isolation again reduces hadronic background.

- Muons with a transverse momentum larger than about $2\,\mathrm{GeV}$ are able to reach the central muon detector and can produce signals in the limited streamer tubes. A pattern recognition program groups these wire and strip hits into associations and via a 2–dimensional mapping, wire and strip track segments are derived. Then a track fit is applied, which provides the final kinematic quantities of the track. After a successful link to a track measured in the central tracker, the tracks reconstructed in the central muon system are used to identify the muon candidates. Furthermore, hits in a minimal number of layers are required as well as a maximal distance of the track extrapolation from the vertex. Details can be found in [73] and references therein.

- The track reconstruction in the central muon detector is limited due to the geometrical acceptance. In the affected regions, the muon finding efficiency is increased by the tail

catcher (see chapter 3.2.3). A track measured with the inner tracking system must match an energy deposit in the instrumented iron within a distance of $R = 0.5$. In the tail catcher calorimeter, the minimum depth of $E_{R=0.5}^{LAr}$ must be larger than $40$ cm which suppresses hadronic showers. At least one LAr cluster is required to contribute to $E_{R=0.5}^{LAr}$. The detailed selection criteria for muons in the tail catcher calorimeter are described in [79].

- If the muon candidate has no track which has been measured in the central tracking system and if its polar angle is $\theta_\mu < 12.5°$, the forward muon detector is used to measure the transverse momentum of the muon candidate. These muon candidates must fulfil a specific track quality [70]. Furthermore, the $z$–position of the first point of the track measured in the forward muon detector must fulfil $-400\,\text{cm} < z < 300\,\text{cm}$.

- For muon pairs, the track opening angle $\alpha_{\mu1,\mu2}$ and the polar angle sum of muon pairs $(\theta^{\mu1} + \theta^{\mu2})$ must fulfil $\alpha_{\mu1,\mu2} < 165°$ and $|\theta^{\mu1} + \theta^{\mu2} - 180°| > 10°$ if $\alpha_{\mu1,\mu2} > 150°$ to reject cosmic muons. For this purpose, information from both the central tracking system and the central muon detector are used. The event timing for muon events must satisfy $|\Delta T_0| < 3.8$ ns. The difference of the event timing in the upper and the lower part of the central muon detector must fulfil $T_{upper}^\mu - T_{lower}^\mu < 3.8$ ns. Moreover it is required that the muons originate from the vertex which rejects beam halo events. These cuts are described in detail in [73].

The muon selection criteria are summarised in table 4.3. The resulting efficiency to identify muons is larger than $90\%$ [6].

## 4.3.3   Jet identification

Jets are reconstructed from energy deposits in the LAr calorimeter combined with well measured tracks using a modified inclusive $k_\perp$ algorithm [80,81] in the laboratory frame with the separation parameter set to $1$. A $P_T$ weighted recombination scheme is used in which jets are treated as massless. Electron candidates are excluded from the algorithm. Moreover, not all particles are assigned to hard jets. The requirements on the jet candidate are:

- Only jets in the polar angle range $7° < \theta_{Jet} < 140°$ are considered to ensure that they are reliably measured. Moreover, the transverse momentum of the jet must be at least $10\,\text{GeV}$. The $P_T$ cut mainly reduces events coming from higher order QCD radiation and non–perturbative effects [53]. The cut on the polar angle also reduces the contribution of fake jets at large polar angles (see below). Besides, for $\theta_{Jet} < 10°$ the MC calculations do not fully confirm the jet energy calibration [70].

- In some detector regions, in particular in regions with a huge amount of dead material, the electron finder is inefficient. Thus, a jet can be faked by the scattered electron or the electron may be a part of a jet. This inefficiency mainly affects multi–jet events, *i.e.* the

$jjj \not{P}_\perp$ channel, especially if the jets have high transverse momenta. To reject electrons which are misidentified as jets, topological criteria for electron–jet separation are applied:

- The invariant mass of a jet is defined as $M^{Jet} = \sqrt{(\sum_i p_i^\mu)^2}$, where the sum extends over the four–momentum $p_i^\mu$ of each object $i$ which is assigned to the jet. The jet energy fraction measured in the electromagnetic part of the LAr calorimeter is denoted as $EM_{frac}^{Jet}$. The invariant mass of the jet divided by its transverse momentum $P_T^{Jet}$ is restricted to $M^{Jet}/P_T^{Jet} > 0.1$ and to $M^{Jet}/P_T^{Jet} > 0.15$ if $EM_{frac}^{Jet} > 0.9$.

- The radial moment of a jet is defined as $\langle R \rangle = \sum_i P_{T,i} R_i^{Jet} / \sum_i P_{T,i}$, where the sum runs over the transverse momentum $P_{T,i}$ of each object $i$ which is assigned to the jet. Here, $R_i^{Jet}$ denotes their distance to the jet axis in the $\eta - \phi$–plane. The radial moment is restricted to $\langle R \rangle > 0.2$ and $\langle R \rangle > 0.4$ if $EM_{frac}^{Jet} > 0.9$. These cuts account for the high collimation of the jets which are faked by electrons, considering the large value of $EM_{frac}^{Jet}$.

A detailed description of these cuts can be found in [70]. About $80\%$ of fake jets and $3\%$ of genuine jets are rejected for the bosonic stop decay channels. In the $ed$ channel (the $\not{R}_p$ stop decay channel; see table 2.3), the fake jet rejection cuts are not applied since they reject only about $30\%$ of events where an electron is misidentified as a jet.

The jet selection criteria are listed in table 4.3. The resulting jet selection efficiency is greater than $95\%$ [52].

### 4.3.4 Missing transverse momentum

The missing transverse momentum $\not{P}_\perp$ is derived from a summation over all identified particles and energy deposits in the event:

$$\not{P}_\perp = \sqrt{\left(\sum_i (E_i \sin\theta_i \cos\phi_i)\right)^2 + \left(\sum_i (E_i \sin\theta_i \sin\phi_i)\right)^2}. \qquad (4.2)$$

In the channels where one or more neutrinos are expected, the missing transverse momentum must exceed at least $12\,\text{GeV}$. In addition, in these channels an event is only accepted if the energy and the momentum in the beam direction fulfil $\sum_i (E_i - P_{z,i}) < 50\,\text{GeV}$. This requirement reduces the contamination due to badly measured NC DIS events in which fake missing transverse momentum is reconstructed.

## 4.4 Reconstruction methods of kinematics

There are four measurable inclusive kinematic quantities: the energy and the angle of the electron and the hadronic final state, respectively. The Lorentz invariant kinematic quantities $Q^2$, $y$ and

| **Electron selection criteria** | $P_T > 10\,\text{GeV}$<br>$5° < \theta_e < 145°$<br>identified with the electron finder QESCAT<br>$E_{R=0.5}/E_e < 2.5\%$<br>not in $\phi$–region and time period affected by CJC failure<br>$|\phi^e - \phi_{crack}| > 2°$, with $\phi_{crack}\{0°, 45°, 90°, 135°, 180°, 225°, 270°, 315°\}$<br>$|z^e - z_{crack}| > 2$ cm, with $z_{crack}\{-64.63\,\text{cm}, 23.17\,\text{cm}\}$<br>$DCA_{cl}^{tk} < 12\,\text{cm}$<br>$R_{start} < 30\,\text{cm}$ if $\theta > 20°$<br>$R_{start} < 30\,\text{cm}$ if $l_{track} > 10$ cm<br>good quality (DTRA) |
|---|---|
| **Muon selection criteria** | basic muon selection criteria<br>$P_T > 10\,\text{GeV}$<br>$10° < \theta_\mu < 140°$<br>$R^{gtk} > 0.5$<br>$E_{R=0.5}^{LAr} < 8\,\text{GeV}$<br>cosmic and beam halo background rejection cuts |
| **Jet selection criteria** | $P_T > 10\,\text{GeV}$<br>$7° < \theta_{jet} < 140°$<br>reconstructed with inclusive $k_\perp$ algorithm<br>$M^{jet}/P_T^{jet} > 0.1$<br>$M^{jet}/P_T^{jet} > 0.15$ if $EM_{frac} > 0.9$<br>$\langle R \rangle > 0.02$<br>$\langle R \rangle > 0.04$ if $EM_{frac} > 0.9$ |

**Table 4.3:** *The main selection criteria for electrons, muons and jets. For electrons, the track conditions apply to both DTRA and DTNV tracks if not otherwise stated.*

$x$ can therefore be reconstructed with different methods which are described below. Here, only the variables needed for this analysis are given.

## The electron method

The electron method uses solely the measurement of the polar angle $\theta_e$, the energy $E_e$ and the transverse momentum $P_{T,e}$ of the electron with the highest $P_T$ in the event:

$$y_e = 1 - \frac{E_e(1 - \cos\theta_e)}{2E_e^0}; \qquad Q_e^2 = \frac{P_{T,e}^2}{1 - y_e}; \qquad x_e = \frac{Q_e^2}{y_e s}. \qquad (4.3)$$

In NC DIS events, these electron quantities are associated to the scattered electron.

## The hadron method

In the hadron method which is the only method to determine $y$ in CC events, all variables are solely calculated from the hadronic energy deposited in the detector. The kinematic quantities are therefore indicated by the index $h$. Here, $y_h$ is calculated by using the Jacquet–Blondel ansatz [82]:

$$y_h = \frac{\sum_h (E_h - p_{z,h})}{2E_e^0}.$$  (4.4)

The inclusive hadron angle $\gamma_h$ is defined by

$$\tan \frac{\gamma_h}{2} = \frac{\sum_h (E_h - P_{z,h})}{P_{T,had}},$$  (4.5)

where $P_{T,had}$ is the total transverse momentum of the hadronic final state.

## The double angle method

The double angle method is based on the measurement of $\theta_e$ and the inclusive hadron angle $\gamma_h$. With these angles, the energy of the scattered electron can be calculated as

$$E_{DA} = \frac{2E_e^0}{1 - \cos\theta_e + \sin\theta_e \tan(\gamma_h/2)}$$  (4.6)

and serves as reference energy to the electron energy $E_e$ which is exploited for the electron energy calibration (see section 4.5).

## The sigma method

The sigma method combines the variables of the electron and the hadronic final state, exploiting energy and momentum conservation of the initial and the final state. This method is independent on the energy $E_e^0$ of the incoming electron and thus not sensitive on radiative effects by initial state radiation. The kinematic variable $y$ can be expressed as

$$y_\Sigma = \frac{\sum_i (E_i - P_{z,i})}{\sum_i (E_i - P_{z,i}) + E_e(1 - \cos\theta_e)}.$$  (4.7)

# 4.5   Electron energy calibration

Since the kinematics can be reconstructed with different independent methods (section 4.4) and thus are over–determined, a calibration of the electron energy is possible. The energy of electrons has been calibrated with a high $Q^2$ NC DIS sample [83], dependent on $z$, the octant and the year. In this analysis, the calibration is revised with a similar NC DIS sample, in which electrons

are selected as described in section 4.3.1. In order to verify the electron energy calibration, the calorimetric energy $E_e$ of the electron candidates is compared with their double angle energy $E_{DA}$. The following requirements on the NC DIS sample must be satisfied:

- The electron must be found with $E_e > 15\,\text{GeV}$ within the angular range $10° < \theta_e < 150°$.

- The selection is restricted to $y_e < 0.9$ and $Q_e^2 > 200\,\text{GeV}$.

- The total missing transverse momentum must satisfy $\not{P}_\perp < 25\,\text{GeV}$.

To ensure a reliable resolution with the double angle method, the following additional quality cuts are applied:

- To reduce initial state radiation, it is required that $45\,\text{GeV} < \sum_i(E_i - P_{z,i}) < 65\,\text{GeV}$.

- The inclusive hadron angle must fulfil $\gamma_h > 8°$ which ensures a complete measurement of the hadronic final state in the calorimeter.

- Furthermore, it is required that $y_\Sigma < 0.3$ for $z < 20\,\text{cm}$ and $y_\Sigma < 0.5$ for $z > 20\,\text{cm}$ which assures a good resolution of the double angle energy $E_{DA}$ [84] (see section 4.4). Here, the lower event rate in the forward region $z > 20\,\text{cm}$ requires the looser $y_\Sigma$ cut.

The comparison of the electron energies $E_e$ and $E_{DA}$ is done dependent on the wheels, the $z$ direction, the polar angle $\theta_e$, the *segments* and the energies $E_e$ and $E_{DA}$. A segment is an octant (1...8) within a wheel (BBE,CB1,CB2,CB3) as described in chapter 3.2.2. The last segment combines the wheels FB1, FB2 and IF. Hence, the LAr calorimeter is divided into a total of $33$ segments. In figure 4.2, the distributions of the electron energy and the double angle energy $E_{DA}$ of electron candidates with the selection criteria given above are shown for the 1994–1997 and the 1999/2000 $e^+p$ data sample. In addition, figure 4.3 shows the distributions of the $z$–position of the electron candidate for both $e^+p$ H1 data samples. The data is described well by the MC simulation in the whole electron energy and double angle energy ranges for both data samples, as well as the $z$–position measurement is confirmed by the NC DIS Monte Carlo.

The ratios $E_{DA}/E_e$ dependent on the variables listed above are shown in figures 4.4 and 4.6 for the 1994–1997 and the 1999/2000 $e^+p$ data sample, respectively. In order to determine the electromagnetic energy scale uncertainty, the ratio $E_{DA}/E_e$ of the data has to be compared with that of the NC DIS Monte Carlo. Figures 4.5 and 4.7 justify that the ratio $R_{data}/R_{MC} = (E_{DA}/E_e)_{data}/(E_{DA}/E_e)_{MC}$ varies between $0.7\%$ and $3\%$, dependent on the $z$–position of the particle's impact on the LAr calorimeter. Except in vicinity of the $z$–cracks, the electromagnetic energy scale uncertainty is largely confirmed to be

- $1\%$ in the backward part, $z < -145\,\text{cm}$,

- $0.7\%$ in the CB1 and CB2 wheels, $-145\,\text{cm} < z < 20\,\text{cm}$,

- $1.5\%$ for $20\,\text{cm} < z < 100\,\text{cm}$ and
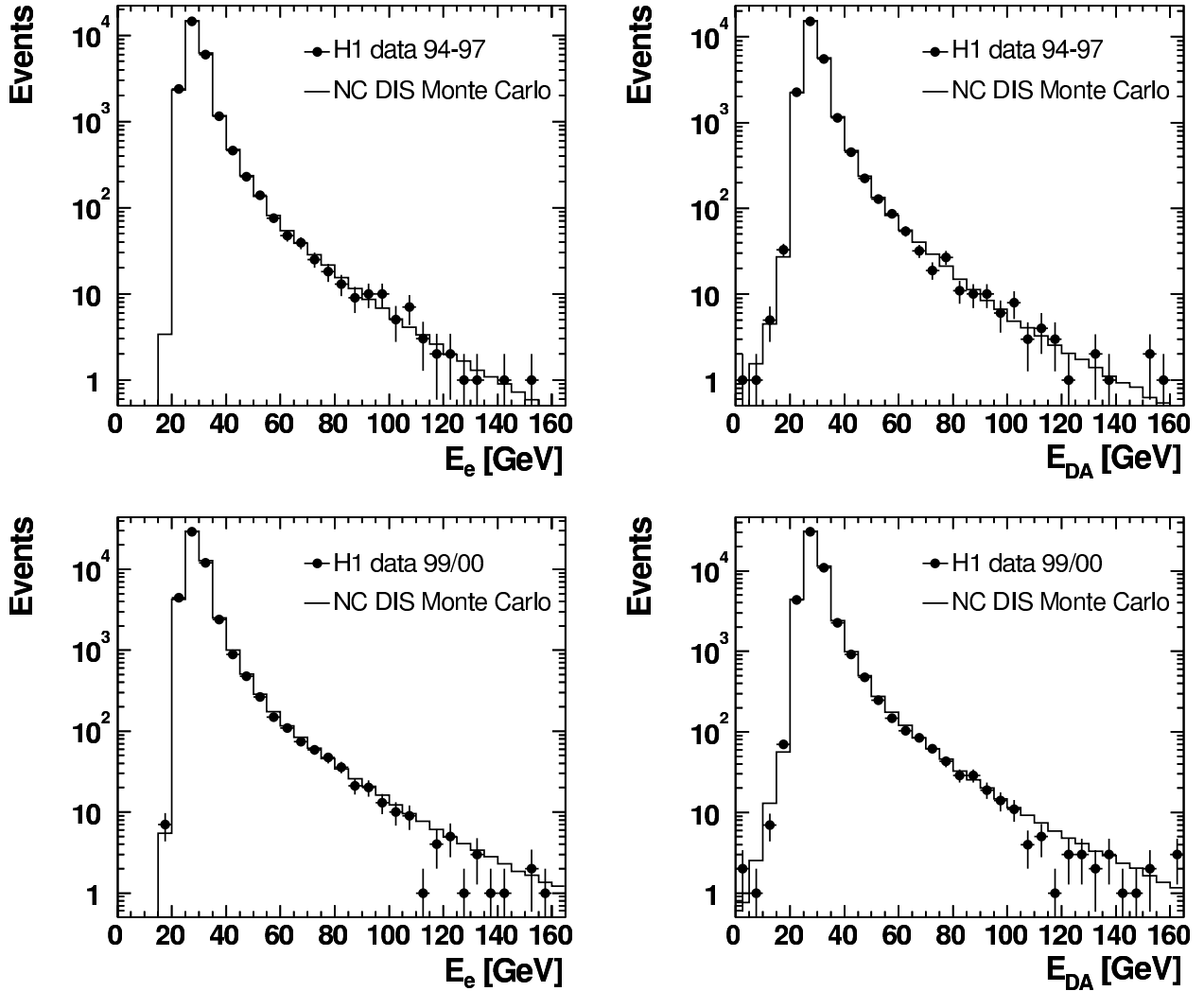
**Figure 4.2:** *The distributions of the electron energy $E_e$ (left) and the energy $E_{DA}$, calculated with the double angle method, (right) of electron candidates with the selection criteria given in section 4.5 for the 1994–1997 (top) and 1999/2000 $e^+p$ (bottom) data sample.*

- $3\%$ in the forward part, $z > 100\,\mathrm{cm}$,

as determined in [83]. Regarding the ratio $R_{data}/R_{MC}$ in dependence of the electron energy or the double angle energy, it is confirmed that the electromagnetic energy scale uncertainty is around $1\%$ in the most part of the NC DIS sample. Even dependent on the segment, the ratio $R_{data}/R_{MC}$ does not exceed $2\%$.
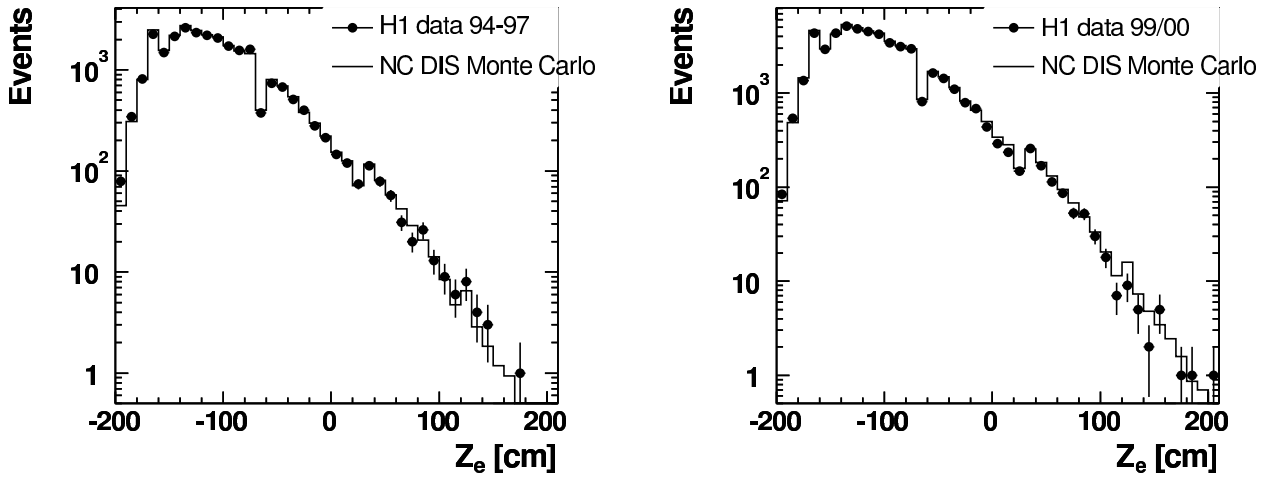
**Figure 4.3:** *The distributions of the $z$–position of the electron for the 1994–1997 (left) and 1999/2000 $e^+p$ (right) data sample.*

# 4.6    The hadronic final state

The hadronic final state is defined as all particles measured in the detector, *i.e.* the LAr calorimeter, the SPACAL, the instrumented iron and the inner tracking system. Only electron candidates are excluded by this definition. The hadronic final state is reconstructed using the software package FSCOMB [85, 86]. This algorithm makes use of the fact that the energy measurement in the calorimeters is the more precise the larger the energy is. In contrast, the precision of the measurement of charged particles with low energy is much better in the central tracking system. As a consequence, *combined objects* are defined by the following procedure: Tracks with a transverse momentum below $2\,\mathrm{GeV}$ pointing to the primary vertex are extrapolated to the calorimeter front face. Concentric to this track, a cylinder of radius $25$ cm is defined in which all energy deposits in the electromagnetic part of the LAr calorimeter are associated to the track. Energy deposits in the hadronic calorimeter section have to be contained in a cylinder of radius $50$ cm to be assigned to the track. The measurement of the calorimetric energy is used if it is larger than the track energy; then the track is rejected. Else, the calorimeter cluster with the smallest distance of closest approach to the track is removed. This procedure is repeated until the cluster energy is sufficiently comparable with that of the track energy.

## Calibration of the hadronic final state

In this analysis, the hadronic final state has been calibrated with an energy weighting scheme of the LAr calorimeter as described in [86] and references therein. In [52, 70], further reweighting factors are applied to the transverse momenta of the jets, investigating a NC DIS sample similar to that in [83]. The uncertainty of the relative hadronic energy scale in the LAr calorimeter turns out to be $2\%$. For details of the hadronic final state calibration see [70].

| Object | Energy scale unc. | $\theta$ unc. | $\phi$ unc. | Identification eff. unc. | Trigger eff. unc. |
|---|---|---|---|---|---|
| Jet | 2% | 5 mrad − 10 mrad | - | - | 3% |
| Electron | 0.7% − 3% | 1 mrad − 3 mrad | 1 mrad | 2% − 15% | - |
| Muon | 5% | 3 mrad | 1 mrad | 5% | 5% |

**Table 4.4:** *The systematic uncertainties attributed to the particle measurements.*

# 4.7 Trigger efficiencies

The LAr calorimeter delivers the main trigger for events with high transverse momentum. If the energy deposit in the electromagnetic section of the LAr calorimeter arises from a high $P_T$ electron, the trigger efficiency is close to 100% [13]. The trigger efficiency for events which are triggered only by one jet is above 90% if $P_T^{Jet} > 20\,\text{GeV}$ [53]. For events which are triggered by muons only, the trigger efficiency is above 70% [87]. Missing transverse momentum leads to trigger efficiencies of 60% if $\not{P}_\perp > 12\,\text{GeV}$ and 95% if $\not{P}_\perp > 25\,\text{GeV}$ [88].

Since in the $ed$ channel and $je\not{P}_\perp$ channel the final state contains an electron, the trigger efficiencies are assumed to be approximately 100% (see above) in these final state topologies. In addition, a channel containing more than two objects[1] also have very high trigger efficiencies [71]. In all final state topologies which result from a bosonic stop decay at least three objects are found. In the $j\mu\not{P}_\perp$ channel, the trigger efficiency is determined by the muon or the $\not{P}_\perp$ trigger, whereas in the $jjj\not{P}_\perp$ channel the jet and the $\not{P}_\perp$ trigger are used. Thus, the trigger efficiencies in the kinematic ranges investigated in this analysis are approximately 100% in all selection channels. A more detailed description of the triggers can be found in [71].

# 4.8 Systematic uncertainties

This section describes the sources of experimental and theoretical systematic uncertainties considered in this analysis. The experimental systematic uncertainties which originate from the object measurements are described in the following. In addition, they are summarised in table 4.4. All systematic uncertainties are added in quadrature.

- The electromagnetic energy scale uncertainty is determined to be between 0.7% and 3% depending on the particle's impact position in the LAr calorimeter [13] (see section 4.5). The uncertainty on the polar angle of electromagnetic clusters varies between 1 mrad and 3 mrad, depending on $\theta$ [13]. The uncertainty on the azimuthal angle is 1 mrad.

---

[1]Here, an object denotes an identified electron, muon, jet or missing transverse momentum.

| Process | Uncertainty |
|---|---|
| $ep \to jjx$ and $ep \to j\gamma x$ | 15% |
| $ep \to j\nu x$ and $ep \to jex$ | 10% |
| $ep \to jj\nu x$ and $ep \to jjex$ | 15% |
| $ep \to \mu\mu$ and $ep \to ee$ | 3% |
| $ep \to Wx$ and $ep \to Wjx$ | 15% |
| $ep \to e\gamma x$ and $ep \to e\gamma j$ | 10% |
| $ep \to e\gamma p$ and $ep \to e\gamma p'$ | 5% |

**Table 4.5:** *The uncertainties attributed to the different processes of the SM expectation.*

The Monte Carlo simulations of tracks in the central tracking system are not very accurate. This leads to uncertainties on the electron identification efficiencies. The tracking efficiency is known with a precision of $2\%$ for polar angles above $37°$ and deteriorates to $15\%$ in the forward region.

- The muon transverse momentum scale uncertainty amounts to $5\%$. The uncertainty on the polar angle is $3$ mrad and on the azimuthal angle is $1$ mrad.

- The hadronic energy scale of the LAr calorimeter is known to $2\%$ [52]. The uncertainty on the jet polar angle determination is $5$ mrad for $\theta < 30°$ and $10$ mrad for $\theta > 30°$.

- The trigger efficiency uncertainty is estimated considering the object with the highest trigger efficiency. It is determined to be $3\%$ if the event is triggered by a jet [89]. If the event is triggered by a muon, the uncertainty on the trigger efficiency amounts to $5\%$ [87]. Else, the trigger efficiency uncertainty is negligible.

- The uncertainty on the integrated luminosity results in an overall normalisation error of $1.5\%$.

- Depending on the SM production process different theoretical uncertainties are used. These amount to $15\%$ for $W$ production to $10\%$ for NC DIS processes and to $15\%$ for photoproduction. For $ep \to \nu jjjX$ reactions, the theoretical uncertainties are about $20\%$, which takes into account the inadequacies of the parton shower modelling of multi–jet production. All theoretical uncertainties attributed to the different processes of the SM expectation are listed in table 4.5.

- For the SUSY signal detection efficiencies, an uncertainty of $10\%$ is assumed resulting mainly from the linear interpolation in the grid of simulated mass values. An additional

theoretical systematic error, mainly due to the uncertainties on the parton densities, affects the signal cross section. This uncertainty varies between $12\%$ at lower stop masses ($x \approx 0.3$) up to $50\%$ for stop masses of $290\,\text{GeV}$ ($x \approx 0.8$) at $\sqrt{s} = 319\,\text{GeV}$. An additional uncertainty of $7\%$ on the signal cross section [5] arises from the variation of the scale at which the parton densities are evaluated.

For the limit derivation (chapter 6.4), the systematic uncertainties have to be determined as a function of the transverse or invariant mass. The systematic uncertainties on the SM prediction are fitted for each selection channel investigated. Their distributions are shown in figure 4.8 for the four selection channels as a function of the transverse or invariant mass. The uncertainties on the SM prediction at $\sqrt{s} = 301\,\text{GeV}$ and $\sqrt{s} = 319\,\text{GeV}$ differ slightly due to the different uncertainties arising from the statistics and the track efficiencies. The resulting total uncertainty range in the relevant mass regions is roughly between $20\%$ and $50\%$ for the $je\,\slashed{P}_\perp$ channel, between $15\%$ and $90\%$ for the $j\mu\,\slashed{P}_\perp$ channel, between $25\%$ and $75\%$ for the $jjj\,\slashed{P}_\perp$ channel and between $5\%$ and $30\%$ for the $ed$ channel. The average integrated systematic uncertainties amount to about

- $24\%$ in the $je\,\slashed{P}_\perp$ channel,

- $18\%$ in the $j\mu\,\slashed{P}_\perp$ channel,

- $28\%$ in the $jjj\,\slashed{P}_\perp$ channel and

- $12\%$ in the $ed$ channel.
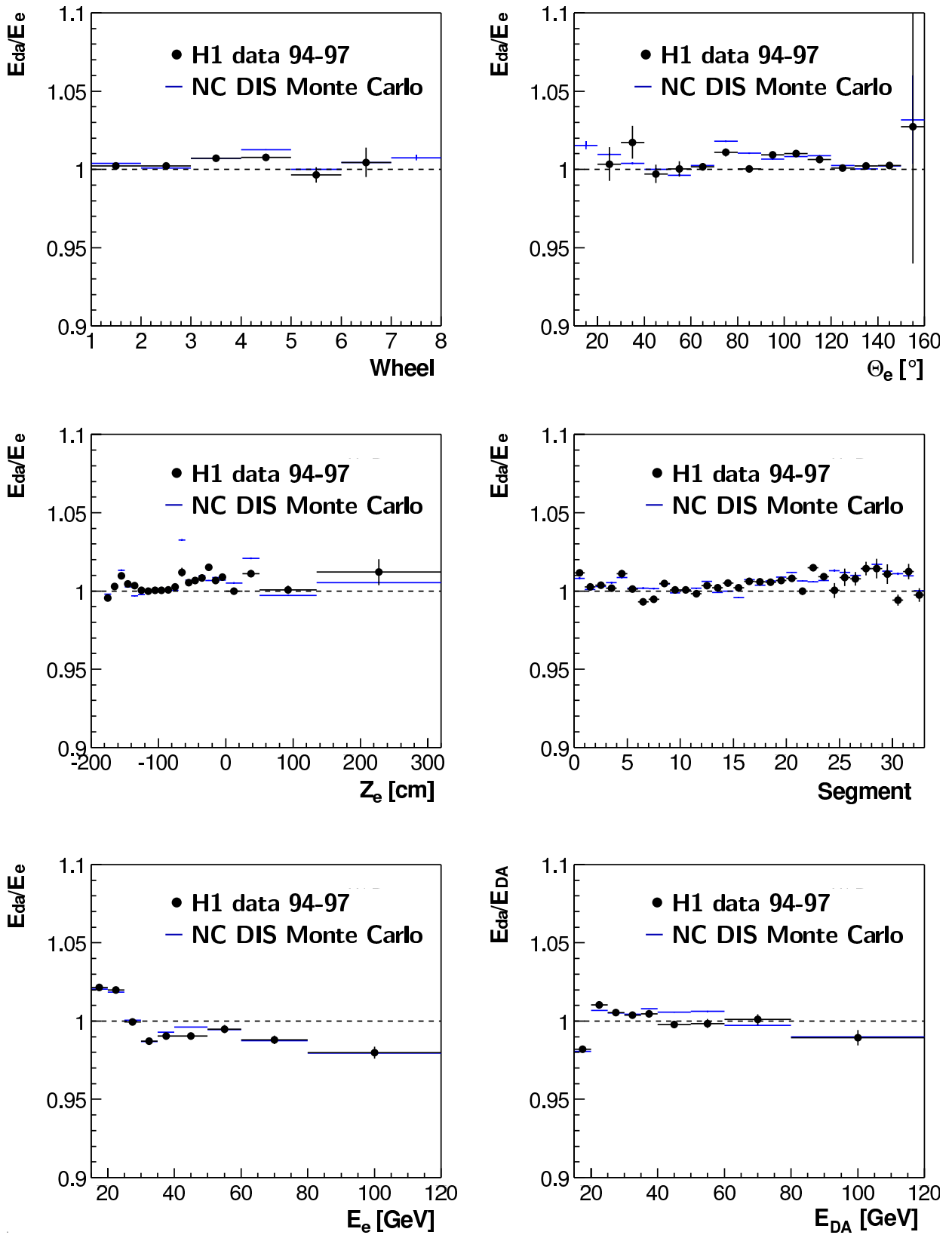
**Figure 4.4:** *The ratio $E_{DA}/E_e$ of the calorimetric energy and the double angle energy dependent on the wheels, the $z$ direction, the polar angle $\theta_e$, the segments and the energies $E_e$ and $E_{DA}$ for the 1994–1997 data sample.*
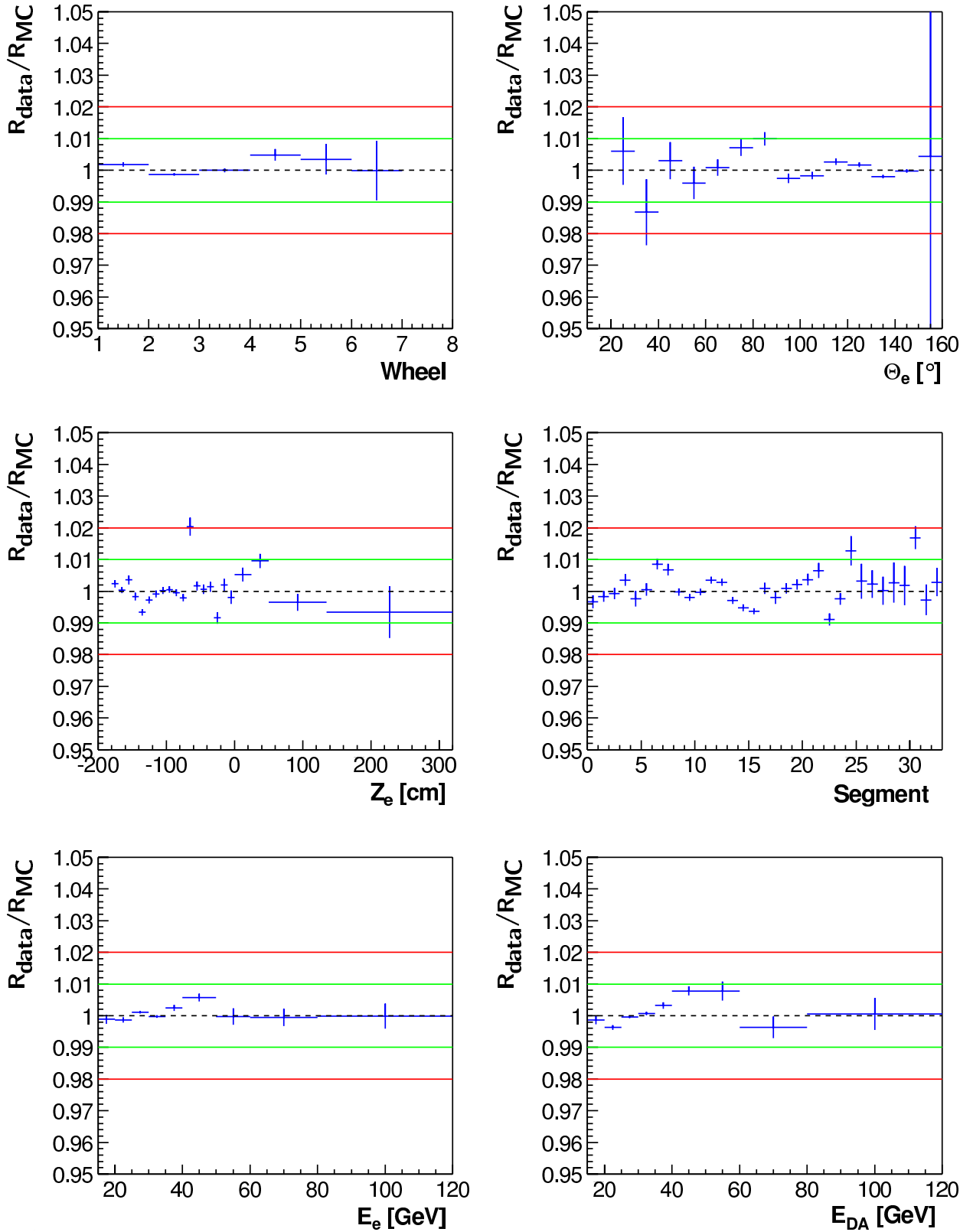
**Figure 4.5:** *The ratio $R_{data}/R_{MC}$ of the data and the NC DIS Monte Carlo expectation dependent on the wheels, the $z$ direction, the polar angle $\theta_e$, the segments and the energies $E_e$ and $E_{DA}$ for the 1994–1997 data sample.*
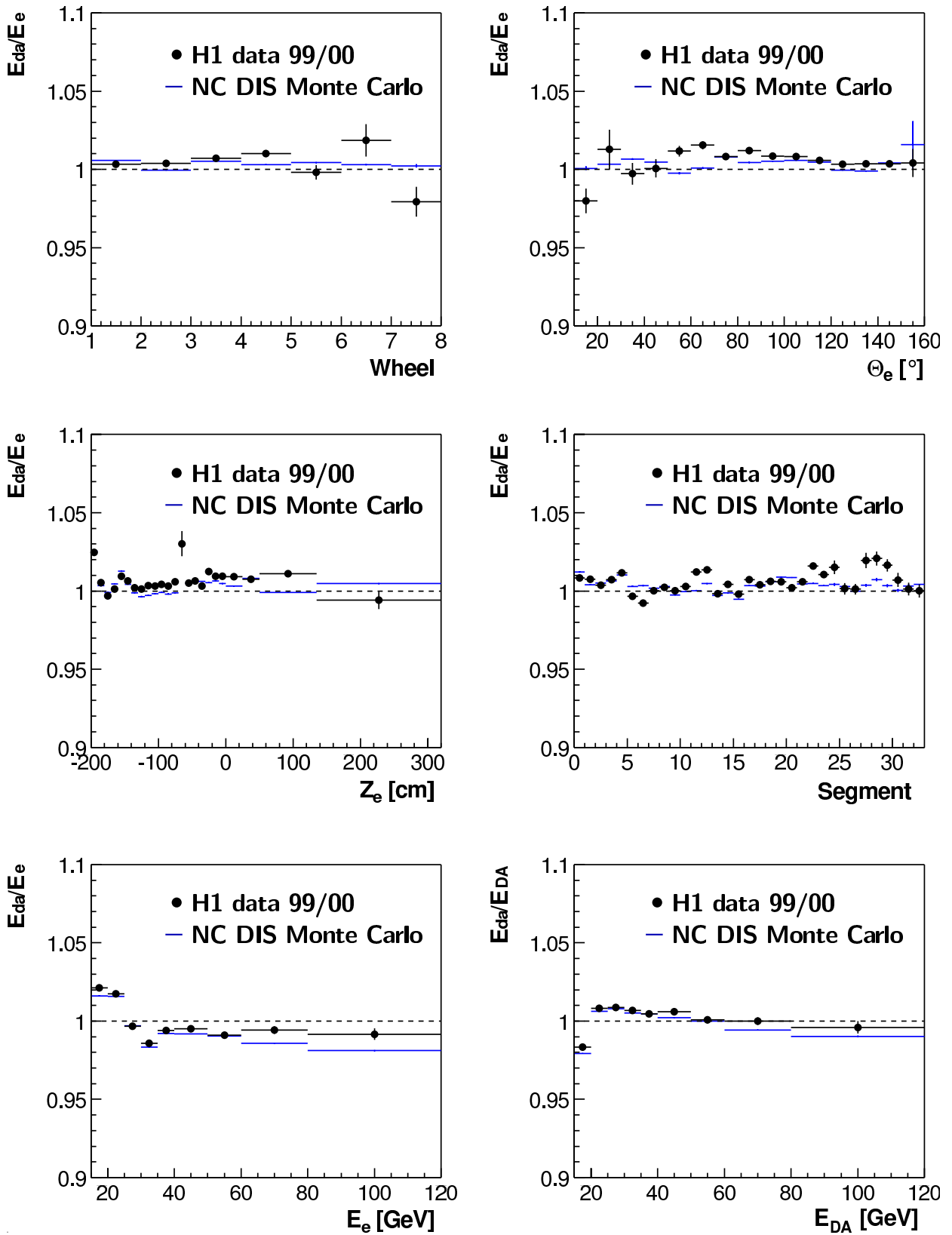
**Figure 4.6:** *The ratio $E_{DA}/E_e$ of the calorimetric energy and the double angle energy dependent on the wheels, the $z$ direction, the polar angle $\theta_e$, the segments and the energies $E_e$ and $E_{DA}$ for the 1999/2000 $e^+p$ data sample.*
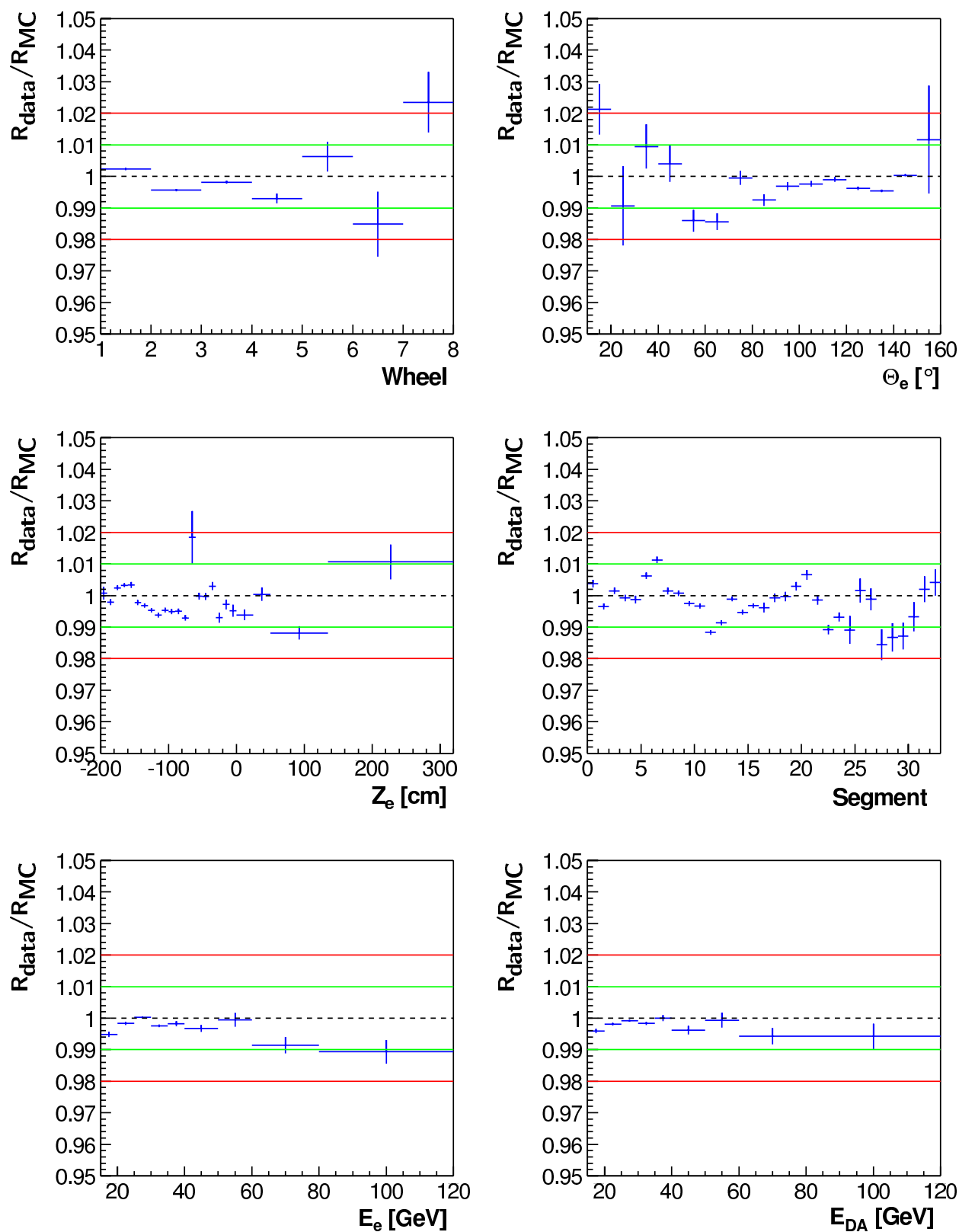
**Figure 4.7:** *The ratio $R_{data}/R_{MC}$ of the data and the NC DIS Monte Carlo expectation dependent on the wheels, the $z$ direction, the polar angle $\theta_e$, the segments and the energies $E_e$ and $E_{DA}$ for the 1999/2000 $e^+p$ data sample.*
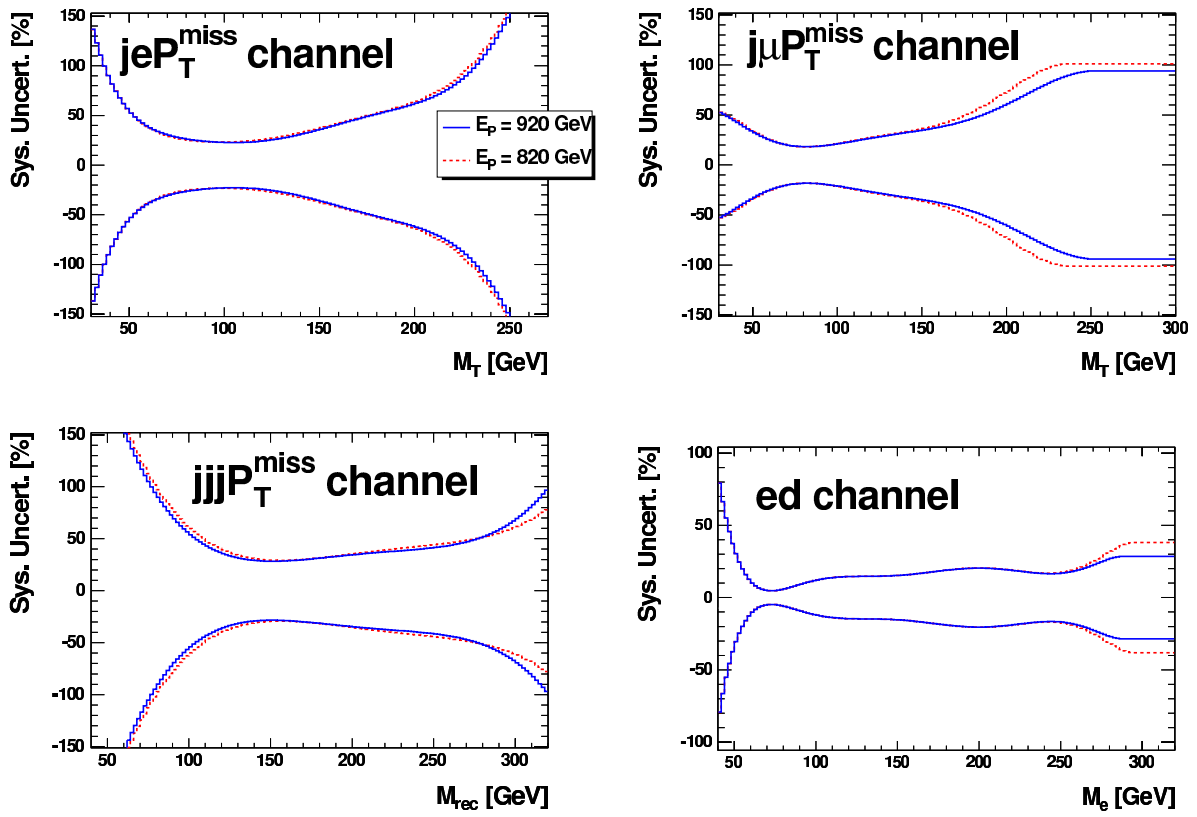
**Figure 4.8:** *The systematic uncertainties on the predicted number of events as a function of the transverse mass or invariant mass for the four selection channels. The fit on the total uncertainty is shown for $\sqrt{s} = 301$ GeV and $\sqrt{s} = 319$ GeV.*

# 5
# Analysis of the Stop Decay Channels

In this chapter, the selection and analysis of the final state topologies considered in this work are described.

According to table 2.3, the bosonic stop decay can lead to three different final state topologies. If the $W$ boson decays into leptons, the signature is a jet, a lepton (electron or muon) and missing transverse momentum ($je\!\!\!/P_\perp$ channel and $j\mu\!\!\!/P_\perp$ channel). The $W$ decay into $\tau\nu_\tau$, where $\tau \to$ hadrons $+\nu$, is not investigated in this analysis since a $\tau$ identification is very difficult. If the $W$ boson decays into hadrons, the signature is three jets and missing transverse momentum which arises only from the $\not{R}_p$ sbottom decay $\tilde{b} \to \nu d$ ($jjj\!\!\!/P_\perp$ channel).

For stop and sbottom masses for which $M_{\tilde{t}} \approx M_{\tilde{b}} + M_W$ holds, the $\not{R}_p$ decay $\tilde{t} \to ed$ becomes dominant (see figure 2.13) and has to be taken into account in order to cover most of the branching fraction in the stop mass range analysed.

The analysis of the the final state topologies under consideration is based on the four–momenta given for each particle. These quantities are provided by the basic data selection, as described in chapter 4, which has also been used in the general search analysis [52,70,71]. In the present analysis, the criteria for the event selection are weaker than in [52,70,71] in order to increase the sensitivity to the stop decay topologies.

## 5.1 The bosonic stop decay channels $\tilde{t} \to je\!\!\!/P_\perp$ and $\tilde{t} \to j\mu\!\!\!/P_\perp$

The signatures of the $je\!\!\!/P_\perp$ and $j\mu\!\!\!/P_\perp$ channel are a high energy electron or muon, a jet and missing transverse momentum. These final state topologies correspond to the events with isolated electrons or muons and missing transverse momentum, observed at H1 [6]. In order to maximise the stop signal sensitivity, the event selection is slightly different in the present analysis. In

addition, the presence of a jet is required because in this analysis a search for new particles with a jet in the final state is performed.

Moreover, the final states of the bosonic stop decays with the $W$ boson decaying into leptons are complementary to the final states considered in the previous $\not{R}_p$ SUSY analyses of squark production by H1 [5, 4].

## 5.1.1    Event selection

The selection criteria for the $je\not{P}_\perp$ and $j\mu\not{P}_\perp$ channel are the following.

- In the $je\not{P}_\perp$ channel, at least one electron is required to be found with $P_T^e > 10\,\text{GeV}$ within the polar angle range $5° < \theta_e < 120°$.

  In the $j\mu\not{P}_\perp$ channel, at least one muon is required to be found with $P_T^\mu > 10\,\text{GeV}$ within the angular range $10° < \theta_\mu < 120°$.

  The cuts on the polar angles reflect the different detector acceptance for electrons and muons.

- At least one jet is required to be found with $P_T^{Jet} > 10\,\text{GeV}$ within the angular range $7° < \theta_{Jet} < 140°$.

- The total missing transverse momentum must satisfy $\not{P}_\perp > 12\,\text{GeV}$.

- The difference in azimuthal angle between the lepton $l$ and the direction of the system $X_{tot}$, composed of the measured energies of all other particles in the event, must be $\Delta\phi(l - X_{tot}) < 165°$. NC background events with a mismeasured lepton are rejected by this cut.

- The ratio $V_{AP}/V_P$ is required to be less than $0.3$. The variables $V_P$ and $V_{AP}$ are defined as the measured transverse calorimetric momentum parallel and anti-parallel to $\vec{P}_{T,had}$, respectively [90]. Here, $\vec{P}_{T,had}$ is the direction of the total calorimetric transverse momentum (see chapter 4.4). $V_P$ and $V_{AP}$ are determined from the transverse momentum vectors $\vec{P}_{T,h}$ of all particles belonging to the hadronic final state. This cut removes NC DIS events which generally have high values of $V_{AP}/V_P$. Besides, it rejects photoproduction background [90].

- In the $je\not{P}_\perp$ channel, the selection is restricted to $y_e > 0.3$. This cut reduces the remaining NC DIS background since particles coming from a bosonic stop decay are boosted in the forward direction. This leads to a rising $d\sigma/dy$ distribution (see figure 5.1) which contrasts with the steeply falling $d\sigma/dy \sim y^{-2}$ distribution of NC DIS events.

In order to confirm that the data is well understood, several control distributions are viewed after the first two selection cuts. This preselection does not have a restriction on the missing transverse momentum or the value of $\sum_i (E_i - P_{z,i})$ and thus contains a large part of NC DIS events.

Figure 5.1 shows the control distributions for the transverse momenta and the polar angles of the electron and jet, respectively, the missing transverse momentum and $y_e$ for the $je\mkern-10mu/\;_\perp$ channel. Here, only the spectra of the data and the SM background for the 1999/2000 $e^+p$ H1 data sample are shown. The control distributions of the 1994–1997 H1 data sample look very similar but the statistical errors are larger. The stop signal which is indicated by the filled histograms has an arbitrary normalisation. Data and SM prediction are in good agreement for this control sample.

In figure 5.2, the control distributions of the variables $V_{AP}/V_P$ and $\Delta\phi(l - X_{tot}) < 165°$ for the $j\mu\mkern-10mu/\;_\perp$ channel are shown. It can be seen that the restrictions on these quantities are very efficient to suppress the NC DIS background. Furthermore, the transverse momenta of the muon and the jet and the missing transverse momentum are illustrated in the figure. In all histograms, the stop signal in arbitrary normalisation is again indicated by the filled histograms.

In the $je\mkern-10mu/\;_\perp$ and $j\mu\mkern-10mu/\;_\perp$ channel, the stop mass cannot be reconstructed since there are two neutrinos in the final state. Therefore, the transverse mass distributions are investigated. The transverse mass is defined as

$$M_T = \sqrt{(\mkern-10mu/\;_\perp + P_T^\ell + P_T^{Jet})^2 - (\vec{\mkern-10mu/\;}_\perp + \vec{P}_T^\ell + \vec{P}_T^{Jet})^2},$$ (5.1)

where $\vec{\mkern-10mu/\;}_\perp$, $\vec{P}_T^\ell$ and $\vec{P}_T^{Jet}$ are the missing transverse momentum, lepton and jet momentum, respectively. The transverse mass distributions are shown in figure 5.3 a) and 5.3 b). The uncertainty on the SM background (see chapter 4.8) is indicated by the shaded error band. In both figures, the signal of a hypothetical $260\,\mathrm{GeV}$ stop which decays into a sbottom of $100\,\mathrm{GeV}$ and a $W$ boson is illustrated. It is indicated by the dashed histogram and given in the same arbitrary normalisation in both channels. In the $je\mkern-10mu/\;_\perp$ channel, $3$ events are found while the expectation from the SM is $3.84 \pm 0.92$ events. In the $j\mu\mkern-10mu/\;_\perp$ channel, $8$ events are found while $2.69 \pm 0.47$ are expected. This slight excess could be interpreted as a scalar top decaying via $\tilde{t} \to \tilde{b}W$ [7] (see section 6.1). Between $60\%$ and $70\%$ of the SM expectation arises from the production of real $W$ bosons. The numbers of events and SM expectations can be found in table 5.2 in section 5.4.

All $11$ events in the $je\mkern-10mu/\;_\perp$ and $j\mu\mkern-10mu/\;_\perp$ channel were also found in [6], where additional events were selected since there were no explicit requirements on jets. In table 5.1, all events with a high energy isolated electron or muon and missing transverse momentum ("isolated lepton events") selected in the H1 $e^+p$ data sample [6] are listed. The channel in which the isolated leptons end up in the present analysis is given in the third column. In addition, the right column gives their rejection reasons in this analysis. The $\theta$ and $P_T$ cuts on the jet are the main restrictions on the selection which discard the remaining isolated lepton events from this analysis. About $30\%$ of the isolated lepton events are rejected by these jet requirements. One additional event is removed by the cut on the $z_{vtx}$.

The event display in figure 5.4 shows an example event which is attributed to the $je\mkern-10mu/\;_\perp$ channel. The transverse momenta are $P_T^e = 41\,\mathrm{GeV}$ and $P_T^{Jet} = 32\,\mathrm{GeV}$ and the missing transverse momentum is $\mkern-10mu/\;_\perp = 43\,\mathrm{GeV}$. The transverse mass of the event amounts to $M_T = 116\,\mathrm{GeV}$. Figure 5.5 shows an event detected in the $j\mu\mkern-10mu/\;_\perp$ channel with $P_T^\mu = 47\,\mathrm{GeV}$, $P_T^{Jet} = 14\,\mathrm{GeV}$ and
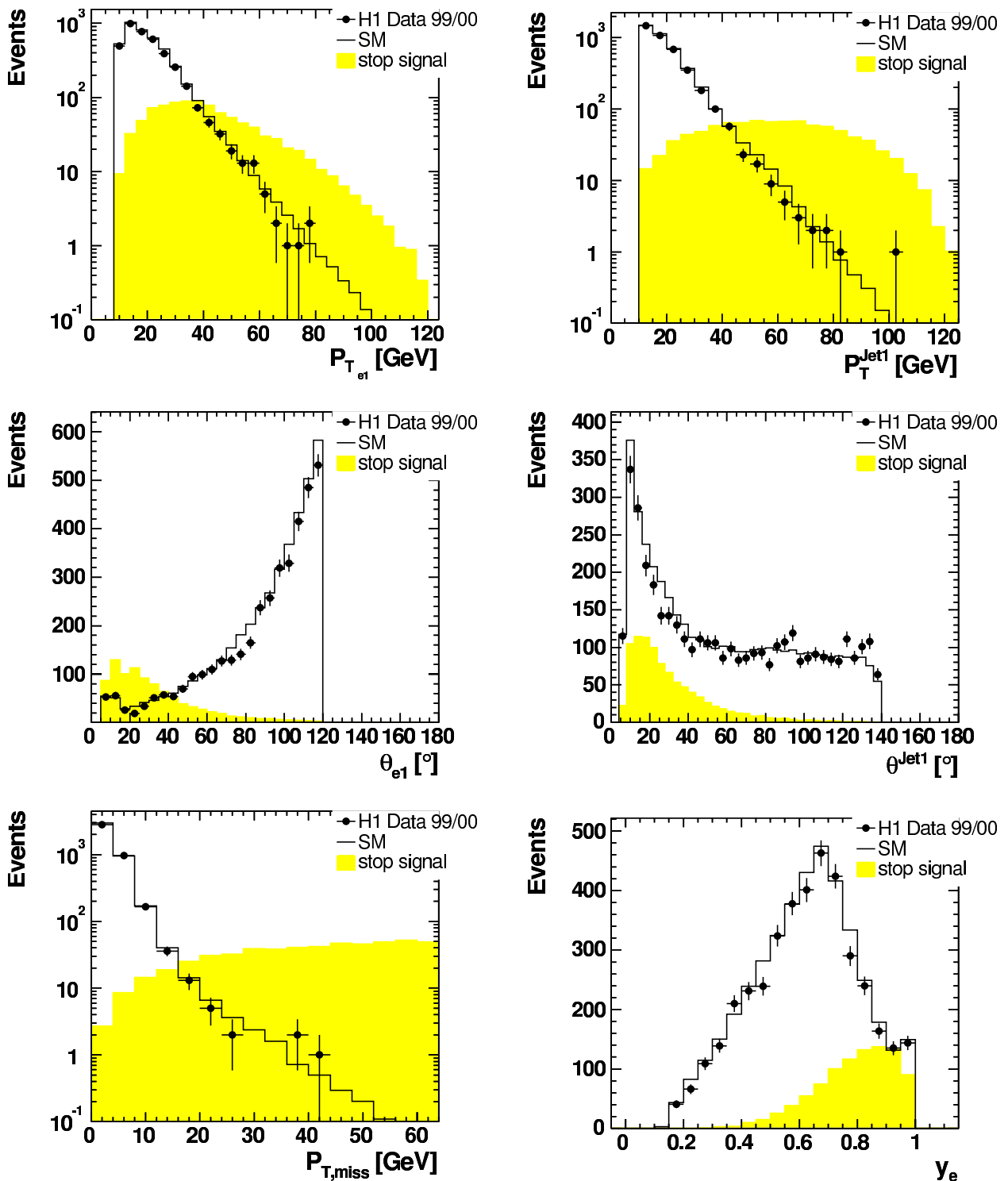
**Figure 5.1:** *Control distributions in the $je\not{P}_\perp$ channel for the 1999/2000 $e^+p$ H1 data sample. The stop signal is indicated by the filled histograms in arbitrary normalisation.*
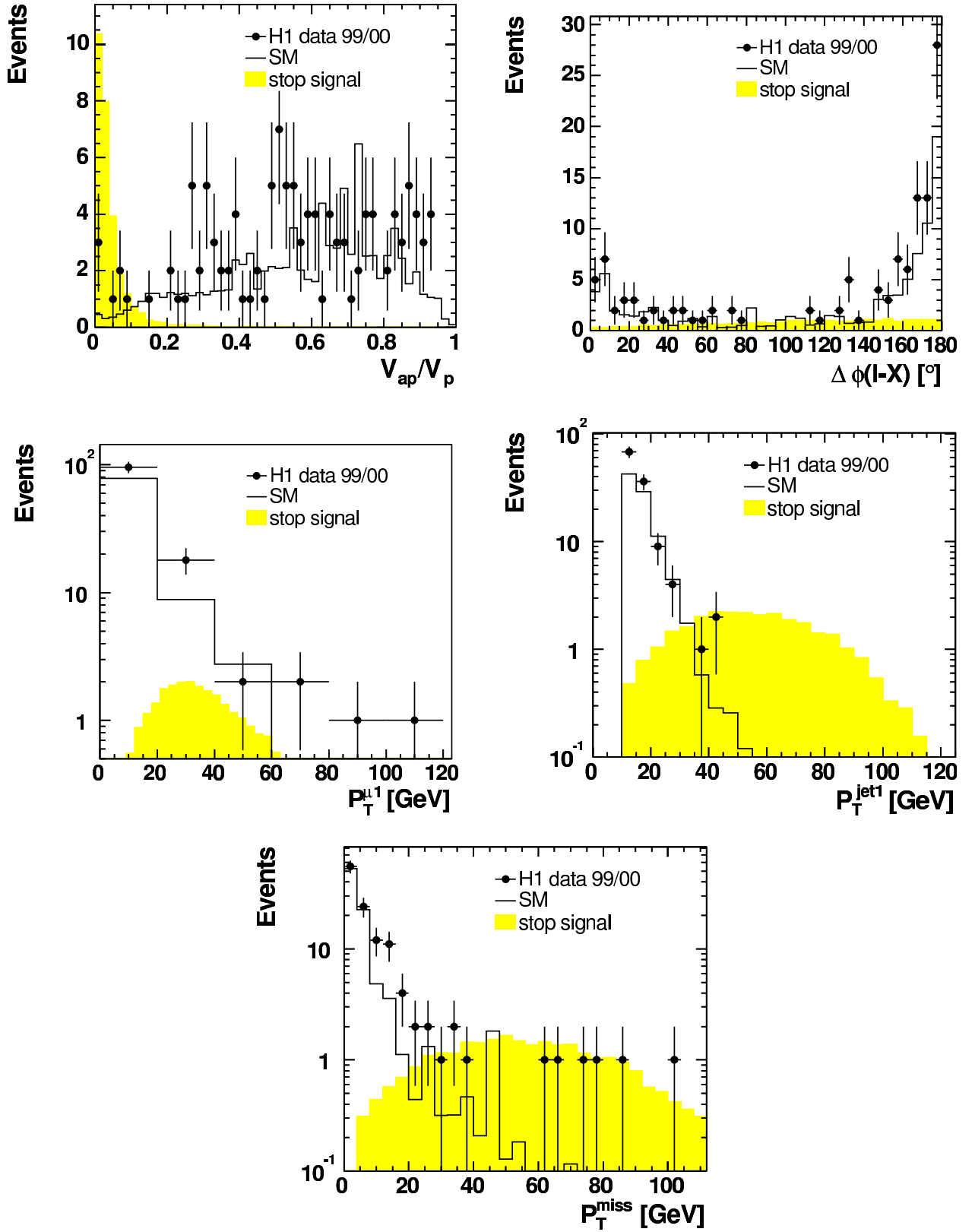
**Figure 5.2:** *Control distributions in the $j\mu\not{P}_\perp$ channel for the 1999/2000 $e^+p$ H1 data sample. The stop signal is indicated by the filled histograms in arbitrary normalisation.*
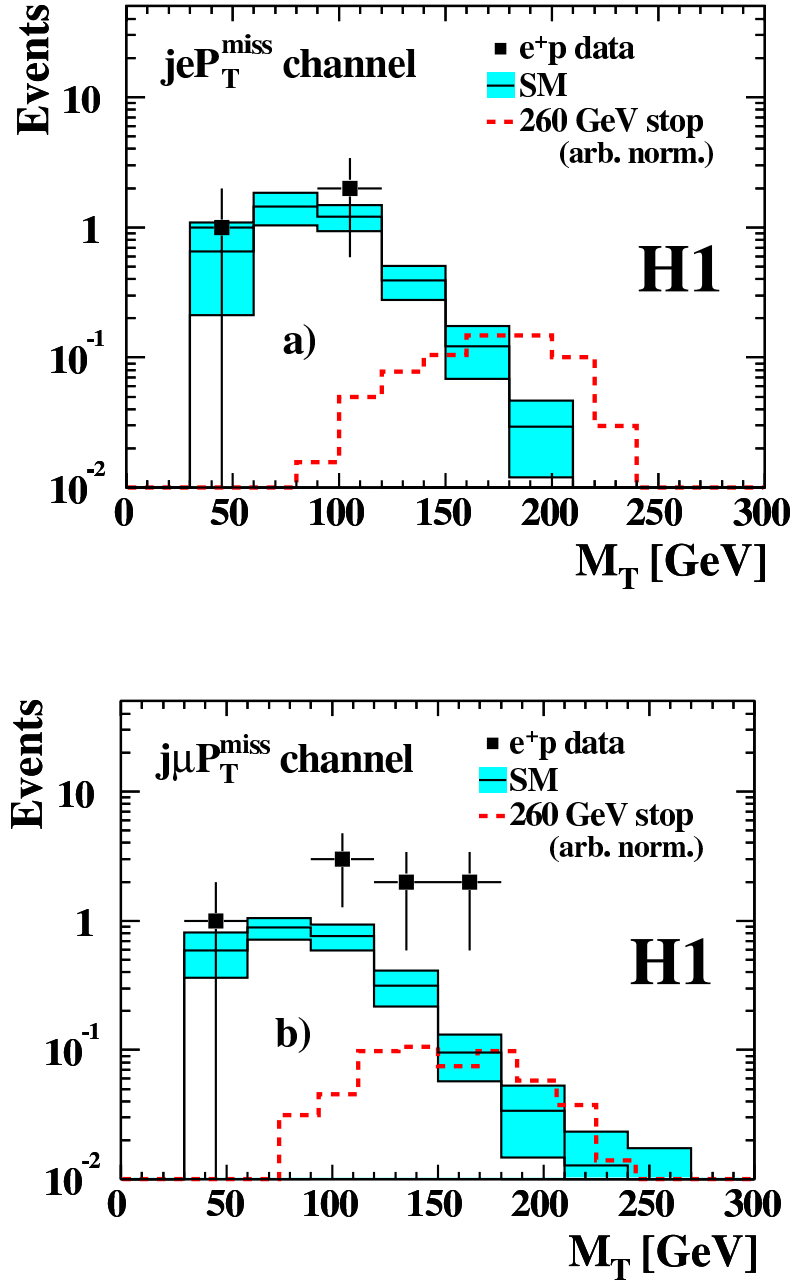
**Figure 5.3:** *The transverse mass spectra for the $e^+p$ H1 data set: a) transverse mass of the $je\!\!\!/P_\perp$ channel; b) transverse mass of the $j\mu\!\!\!/P_\perp$ channel. The data are compared with the SM expectations with the systematic uncertainties shown as the shaded band. The expected signal from a stop with mass $260\,$GeV which decays into a sbottom of $100\,$GeV and a $W$ boson is also shown with arbitrary normalisation. It is indicated by the dashed histogram.*

$\!\!\!/P_\perp = 60\,$GeV. Here, the transverse mass of the event is $M_T = 120\,$GeV. The jets and the leptons of both events have polar angles below $45°$. Thus, these two events could be the result

| Run | Event | Channel | Rejection reason |
|---|---|---|---|
| 90264 | 313 | $e\!\!\!/\!P_{\perp}$ | $\theta^{Jet} < 7°$ |
| 186729 | 702 | $j\mu\!\!\!/\!P_{\perp}$ | |
| 188108 | 5066 | $j\mu\!\!\!/\!P_{\perp}$ | |
| 192227 | 6208 | $j\mu\!\!\!/\!P_{\perp}$ | |
| 195308 | 16793 | $j\mu\!\!\!/\!P_{\perp}$ | |
| 196406 | 38438 | $je\!\!\!/\!P_{\perp}$ | |
| 248207 | 32134 | $je\!\!\!/\!P_{\perp}$ | |
| 251415 | 43944 | $j\mu\!\!\!/\!P_{\perp}$ | |
| 252020 | 30485 | $je\!\!\!/\!P_{\perp}$ | |
| 253700 | 90241 | $j\mu\!\!\!/\!P_{\perp}$ | |
| 266336 | 4126 | $j\mu\!\!\!/\!P_{\perp}$ | |
| 268338 | 70014 | | $|z_{vtx}| > 35\,\mathrm{cm}$ |
| 269672 | 66918 | $e\!\!\!/\!P_{\perp}$ | $P_T^{Jet} < 10\,\mathrm{GeV}$ |
| 270132 | 73115 | $j\mu\!\!\!/\!P_{\perp}$ | |
| 274357 | 6157 | $e\!\!\!/\!P_{\perp}$ | $\theta^{Jet} < 7°$ |
| 275991 | 29613 | $e\!\!\!/\!P_{\perp}$ | $\theta^{Jet} < 7°$ |
| 276220 | 76295 | $e\!\!\!/\!P_{\perp}$ | no jet |
| 277699 | 91265 | $e\!\!\!/\!P_{\perp}$ | $P_T^{Jet} < 10\,\mathrm{GeV}$ |

**Table 5.1:** *The events with a high energy isolated electron or muon and missing transverse momentum ("isolated lepton events") selected in the H1 $e^+p$ data sample [6]. The right column gives their rejection reasons in this analysis.*

of both a Standard Model process or of a stop decaying bosonically.
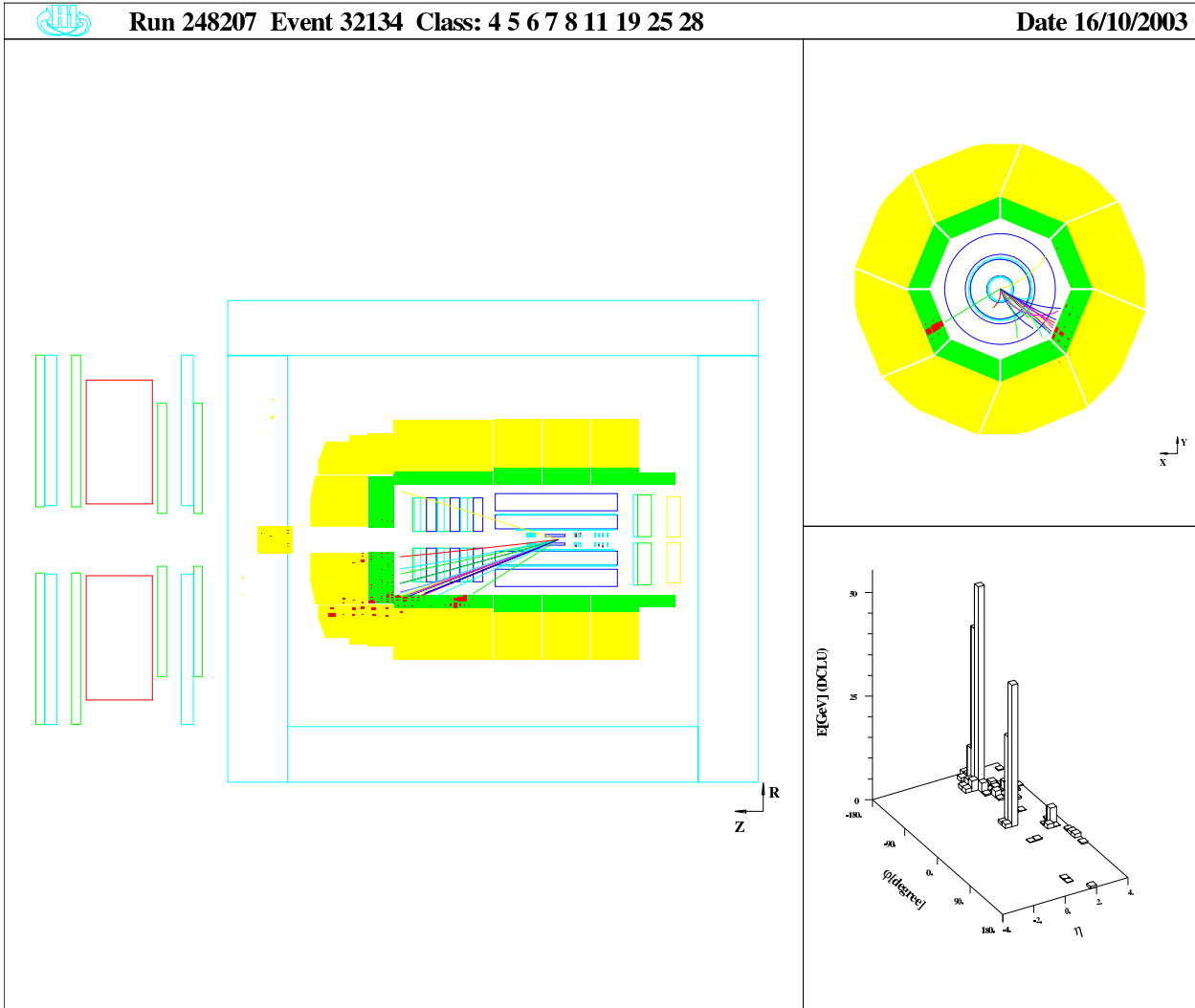
**Figure 5.4:** *The event display of an example event observed in the $je\!\!\!/P_\perp$ channel with $P_T^e = 41\,GeV$, $P_T^{Jet} = 32\,GeV$, $\!\!\!/P_\perp = 43\,GeV$ and $M_T = 116\,GeV$.*

## 5.1.2   Signal selection efficiencies and mass windows

The selection efficiencies for the final state topologies arising from stop decays are obtained as described in section 2.6 in the mass ranges $180\,\text{GeV} < M_{\tilde{t}} < 290\,\text{GeV}$ and $100\,\text{GeV} < M_{\tilde{b}} < 210\,\text{GeV}$. The stop and sbottom mass grid is segmented in steps of typically $20\,\text{GeV}$. The last step to the highest stop (sbottom) mass is only $10\,\text{GeV}$ since stop masses above $290\,\text{GeV}$ are hardly accessible at HERA and thus not considered. For each point in this grid, a total of $1000$ stop signal events are simulated. The efficiency for stop detection is calculated by counting the stop signal events which have passed through a complete simulation of the H1 detector and the relevant selection cuts corresponding to the considered stop decay channel. Between these efficiencies obtained for
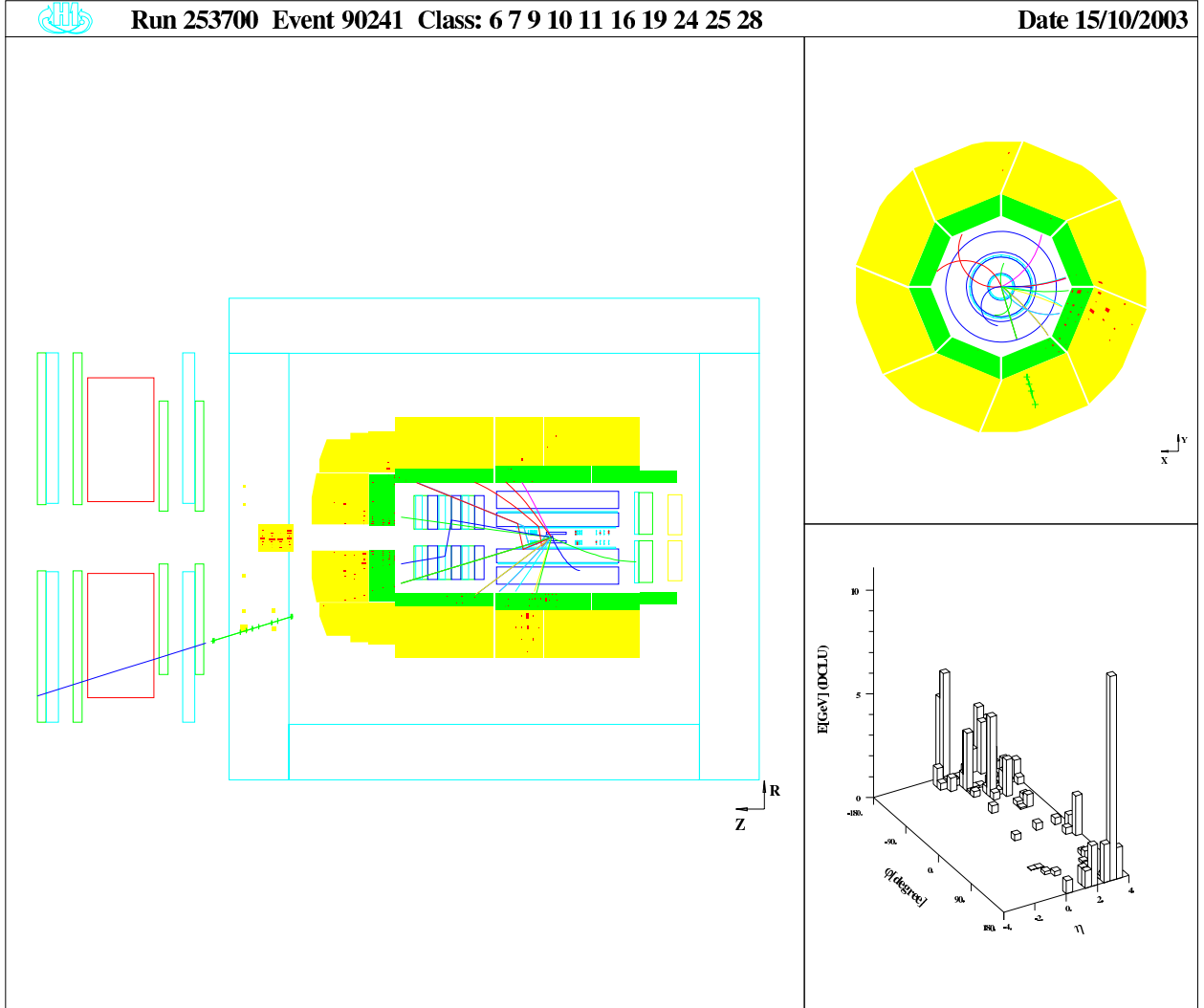
**Figure 5.5:** *The event display of an example event observed in the $j\mu \not{P}_\perp$ channel with $P_T^\mu = 47\,GeV$, $P_T^{Jet} = 14\,GeV$, $\not{P}_\perp = 60\,GeV$ and $M_T = 120\,GeV$.*

each mass grid point, a linear interpolation is applied. The efficiencies are furthermore calculated for different $\not{R}_p$ couplings $\lambda'_{131}$ to account for variation of the efficiencies with the coupling $\lambda'_{131}$, when the stop mass and width are both large.

The stop signal efficiency amounts typically to $35\%$–$45\%$ for the $je \not{P}_\perp$ channel and $30\%$–$40\%$ for the $j\mu \not{P}_\perp$ channel and depends mainly on $M_{\tilde{t}}$ and $M_{\tilde{b}}$. Figures 5.6 and 5.7 illustrate the efficiencies for the $je \not{P}_\perp$ channel and the $j\mu \not{P}_\perp$ channel, respectively, at $\sqrt{s} = 301\,$GeV (left) and $\sqrt{s} = 319\,$GeV (right) in a 2–dimensional plot as a function of the stop and the sbottom mass. In these examples, the $\not{R}_p$ coupling $\lambda'_{131}$ is fixed to $0.3$ which is about the electromagnetic strength. The light points indicate the simulated points in the stop and sbottom mass grid. At very high stop masses ($M_{\tilde{t}} \gtrsim 280\,$GeV), where the stop width gets very large, the efficiencies decrease to
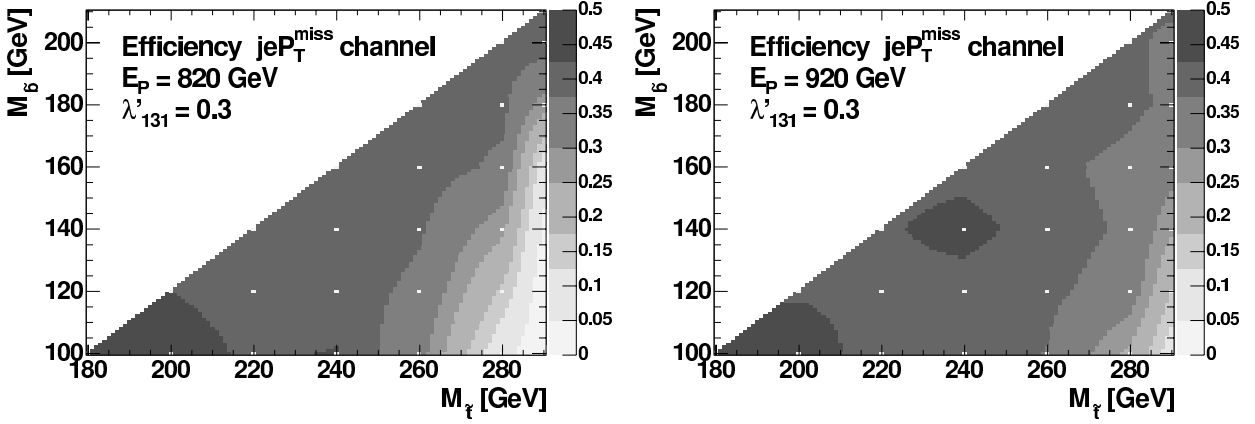
**Figure 5.6:** *The signal selection efficiencies for the $je\!\!\!/P_\perp$ channel at $\sqrt{s} = 301\,GeV$ (left) and $\sqrt{s} = 319\,GeV$ (right) as a function of the stop and the sbottom mass. The $\!\!\!/R_p$ coupling $\lambda'_{131}$ is set to $0.3$. The light points indicate the simulated points in the stop and sbottom mass grid.*
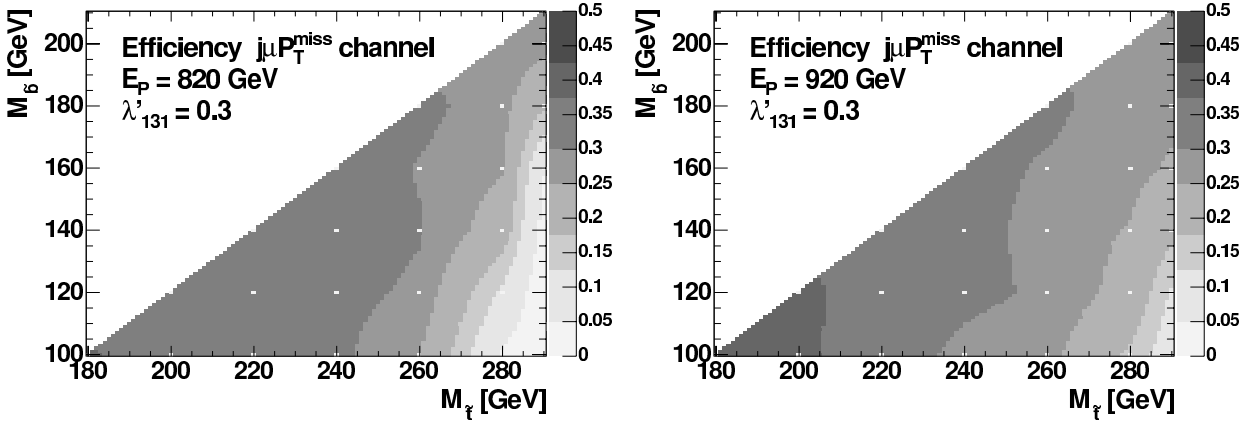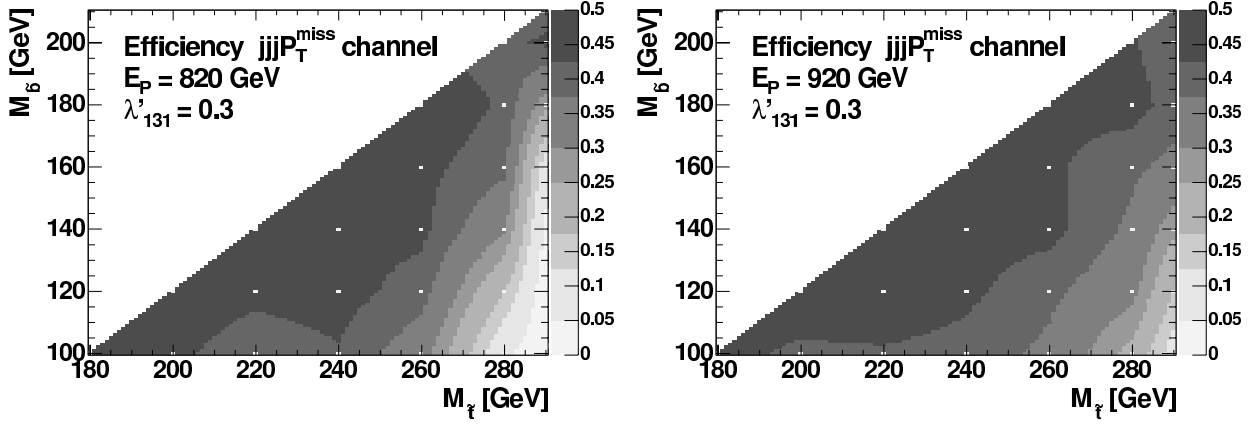


**Figure 5.7:** *The signal selection efficiencies for the $j\mu\!\!\!/P_\perp$ channel at $\sqrt{s} = 301\,GeV$ (left) and $\sqrt{s} = 319\,GeV$ (right) as a function of the stop and the sbottom mass. The $\!\!\!/R_p$ coupling $\lambda'_{131}$ is set to $0.3$. The light points indicate the simulated points in the stop and sbottom mass grid.*

only a few percent, especially at the lower centre–of–mass energy of $301\,$GeV. In this high stop mass region the efficiencies also depend markedly on the $\!\!\!/R_p$ coupling $\lambda'_{131}$ which is accounted for in the signal simulations. The regions at $M_{\tilde{t}} \approx 260\,$GeV and $M_{\tilde{t}} \approx 240\,$GeV in the $je\!\!\!/P_\perp$ channel (figure 5.6), where the efficiency is slightly larger than in the environment, arise from fluctuations of the efficiency. The diagonal limit which can be seen in the plots is caused by the fact that only the mass region $M_{\tilde{t}} \lesssim M_{\tilde{b}} + 80\,$GeV is investigated.

## The sliding mass window method

For the limit derivation (see chapter 6.3), only events which could have been produced by a bosonic stop decay or the direct $\not{R}_p$ stop decay (see section 5.3) are taken into account. Therefore, a *sliding mass window method* is applied which filters such events. For this purpose, in each stop decay channel the number of observed and expected events satisfying the relevant selection cuts, $N_{data}$ and $N_{SM}$, are integrated within a mass bin (transverse mass bin) around the calculated stop mass (transverse mass), corresponding to the stop decay channel under consideration. Then, in each channel the width of this mass bin is adjusted to the expected mass resolution such that each bin contains events reconstructed within $\pm 2$ standard deviations of the given stop mass. These mass bins slide over the accessible stop mass range. The mean value of the mass bins and the resolution of the mass windows are determined using the root mean square which is given in the $je P_\perp$ and $j\mu P_\perp$ channel by

$$M_T = \sqrt{\frac{1}{N} \sum_{i=1}^{N} M_{T,i}^2}.$$
(5.2)

The sum runs over all stop signal events simulated for one specific stop and sbottom mass (and $\lambda'_{131}$) combination.

Since in the $je P_\perp$ channel and $j\mu P_\perp$ channel the transverse mass is taken into account, the corresponding mass windows are very large and contain most of the observed data events and the SM background expectation.

The mass windows calculated with the sliding mass window method are shown in figure 5.8 for the $je P_\perp$ channel and in figure 5.9 for the $j\mu P_\perp$ channel. They are given for both centre–of–mass energies: $\sqrt{s} = 301\,\text{GeV}$ (left) and $\sqrt{s} = 319\,\text{GeV}$ (right). The $\not{R}_p$ coupling $\lambda'_{131}$ is again set to $0.3$ in both examples. The hashed lines indicate the mean values of the calculated transverse mass windows. Both mass windows are very broad due the limited resolution in the transverse mass which is caused by energy losses arising from the two neutrinos in the final state. In general, the mass windows get broader with the mass. Nevertheless, at the centre–of–mass energy of $\sqrt{s} = 301\,\text{GeV}$, the mass window narrows again for very high transverse masses. This effect is caused by the very low efficiency (below $1\%$) at stop masses of $290\,\text{GeV}$ (see figures 5.6 and 5.7). Therefore, the width of this last mass bin cannot be determined at high accuracy.
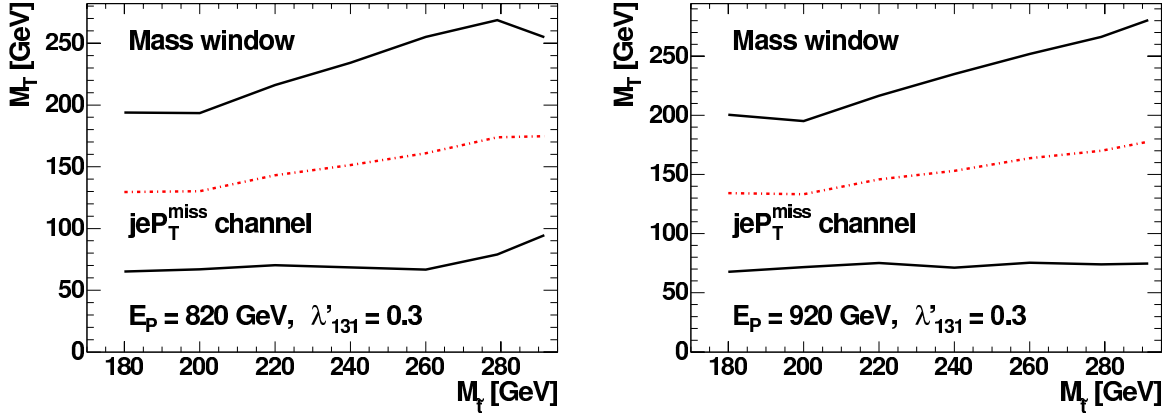
**Figure 5.8:** *The adjusted mass windows for the $je\!\!\!/P_\perp$ channel at $\sqrt{s} = 301\,GeV$ (left) and $\sqrt{s} = 319\,GeV$ (right). The hashed lines indicate the mean values of the calculated transverse mass windows. The $\not{R}_p$ coupling $\lambda'_{131}$ is set to $0.3$.*
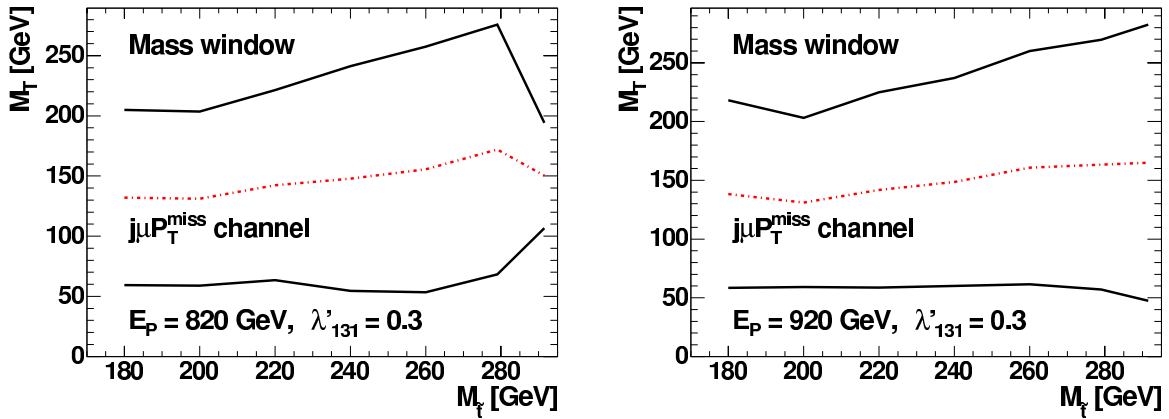


**Figure 5.9:** *The adjusted mass windows for the $j\mu\!\!\!/P_\perp$ channel at $\sqrt{s} = 301\,GeV$ (left) and $\sqrt{s} = 319\,GeV$ (right). The hashed lines indicate the mean values of the calculated transverse mass windows. The $\not{R}_p$ coupling $\lambda'_{131}$ is set to $0.3$.*

# 5.2    The bosonic stop decay channel $\tilde{t} \rightarrow jjj\!\!\!/P_\perp$

The bosonic stop decay with the subsequent $W$ boson decay into hadrons is also not considered in the existing $\not{R}_p$ SUSY analyses. In those works, at least two jets are required, whereas in the present analysis all three jets which could occur in the $jjj\!\!\!/P_\perp$ channel are searched for.

## 5.2.1 Event selection

For the $jjj\displaystyle{\not}P_\perp$ final state topology the following criteria are required.

- Three jets must be found with

  - $P_T^{Jet1} > 20\,\text{GeV}$,
  - $P_T^{Jet2} > 15\,\text{GeV}$ and
  - $P_T^{Jet3} > 10\,\text{GeV}$,

  each with polar angle $7° < \theta_{Jet} < 140°$. Here, $P_T^{Jet1}$ ($P_T^{Jet2,3}$) is the transverse momentum of the jet with the (second, third) highest $P_T$ in the event.

- The total missing transverse momentum must satisfy $\displaystyle{\not}P_\perp > 25\,\text{GeV}$.

- The selection is restricted to $y_h > 0.4$ exploiting the different $y_h$ distributions of the stop signal and the SM background. This cut is applied in analogy to the $y_e$ requirement in the $je\displaystyle{\not}P_\perp$ channel. The $y_h$–cut in this $jjj\displaystyle{\not}P_\perp$ channel is more restrictive in order to maximise the signal sensitivity.

The control distributions in figure 5.10 show different kinematical quantities after a preselection in which only the presence of the jet with the highest $P_T$ is required. Furthermore, the cut on $y_h$ is not applied in this preselection. These control distributions show that the SM expectation is in agreement with the data for CC DIS–like processes which mainly contribute here. The stop signal in arbitrary normalisation is again indicated by the filled histograms.

Assuming that only one neutrino is present in the event and applying the constraints

$$\vec{\displaystyle{\not}P}_\perp = \vec{P}_T^\nu \qquad \text{and} \tag{5.3}$$

$$\sum_i (E_i - P_{z,i}) + (E_\nu - P_{z,\nu}) = 2E_e^0, \tag{5.4}$$

the four–vector of the neutrino can be calculated from the total four–momentum of the event, $P_{T,tot}$. Since neutrinos are assumed to be massless, the energy of the neutrino can be calculated as

$$E_\nu = \frac{(P_T^\nu)^2 + (E_\nu - P_{z,\nu})^2}{2(E_\nu - P_{z,\nu})}. \tag{5.5}$$

Hence, the invariant mass $M_{rec}$ can be reconstructed using equation 5.4,

$$M_{rec} = \sqrt{(E_{tot} + E_\nu)^2 - (P_{z,tot} + P_{z,\nu})^2}, \tag{5.6}$$

where $P_{z,\nu}$ is computed from equation 5.3. In this final state topology, $M_{rec}$ is reconstructed with a mass resolution of about $15\,\text{GeV}$. The reconstructed mass distribution for the $jjj\displaystyle{\not}P_\perp$ channel is shown in figure 5.11 c). The uncertainty on the SM background is indicated by the shaded
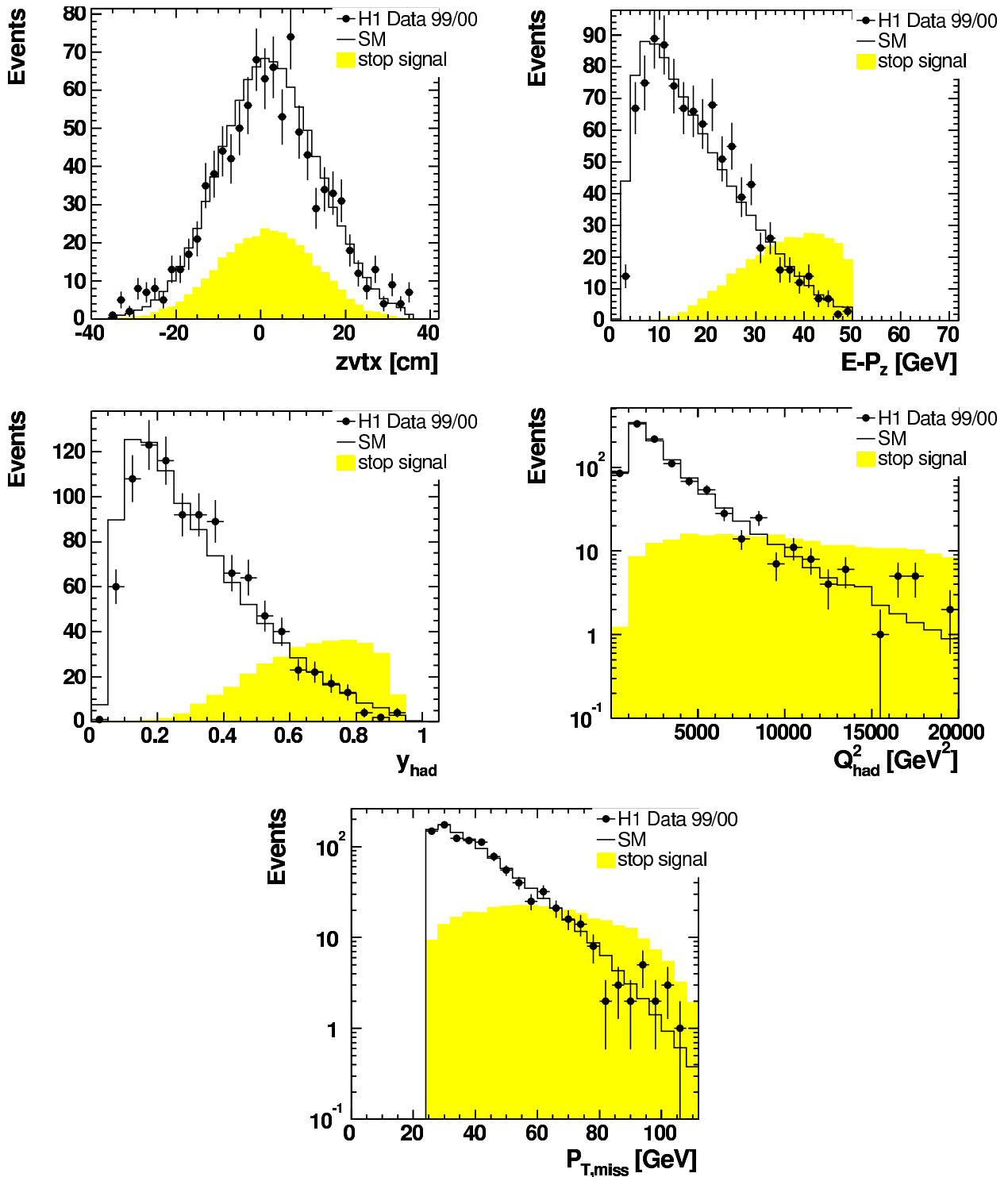
**Figure 5.10:** *Control distributions in the $jjj\not{P}_\perp$ channel for the 1999/2000 $e^+p$ H1 data sample. The stop signal is indicated by the filled histograms in arbitrary normalisation.*
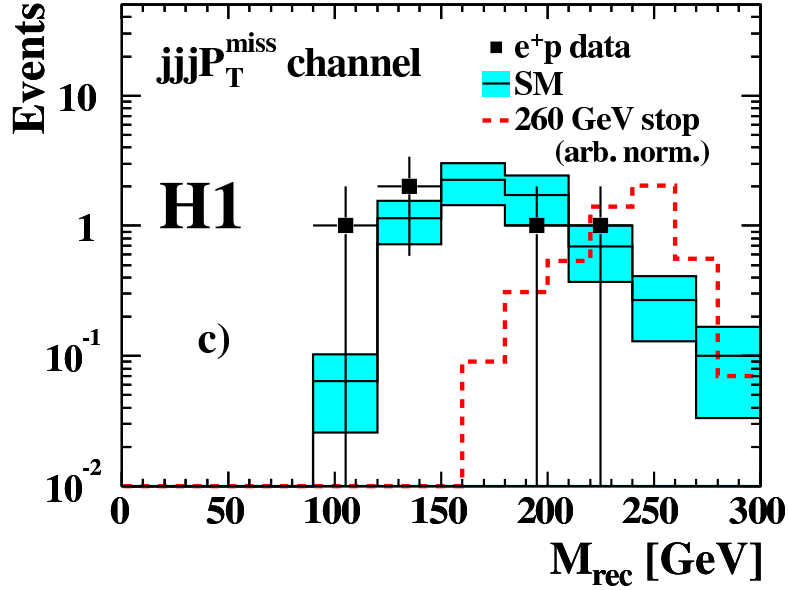
**Figure 5.11:** *The reconstructed mass distribution for the $e^+p$ H1 data set of the $jjj\!\!\!/\!P_\perp$ channel. The data are compared with the SM expectation with the systematic uncertainties shown as the shaded band. The expected signal from a stop with mass $260\,\text{GeV}$ which decays into a sbottom of $100\,\text{GeV}$ and a $W$ boson is also shown with arbitrary normalisation. It is indicated by the dashed histogram.*

error band and again the signal of a hypothetical $260\,\text{GeV}$ stop which decays into a sbottom of $100\,\text{GeV}$ and a $W$ boson is illustrated as dashed histogram. The stop signal is given in the same arbitrary normalisation as the stop signals for the $je\!\!\!/\!P_\perp$ and $j\mu\!\!\!/\!P_\perp$ channels. A total of $5$ events are found while $6.24 \pm 1.74$ events are expected from SM processes (see table 5.2). The SM background arises predominantly from CC DIS processes.

## 5.2.2  Signal selection efficiencies and mass windows

Again, the selection efficiencies are determined as a function of the stop mass, the sbottom mass and the coupling $\lambda'_{131}$. The stop detection efficiency is typically $35\%$–$50\%$ in case of this final state topology. Figure 5.12 illustrates the signal selection efficiencies for the $jjj\!\!\!/\!P_\perp$ channel at $\sqrt{s} = 301\,\text{GeV}$ (left) and $\sqrt{s} = 319\,\text{GeV}$ (right) as a function of the stop and the sbottom mass. The $\not{R}_p$ coupling $\lambda'_{131}$ is chosen to be $0.3$.

The sliding mass window method explained in section 5.1.2 leads to the adjusted mass windows shown in figure 5.13 for $\sqrt{s} = 301\,\text{GeV}$ (left) and $\sqrt{s} = 319\,\text{GeV}$ (right). The $\not{R}_p$ coupling $\lambda'_{131}$ is again chosen to be $0.3$ in these examples. In both plots, the hashed lines indicate the mean values of the calculated reconstructed mass windows.

In figure 5.14, an event which is detected in the $jjj\!\!\!/\!P_\perp$ channel is shown. The transverse momenta of the jets are $P_T^{Jet1} = 60\,\text{GeV}$, $P_T^{Jet2} = 24\,\text{GeV}$ and $P_T^{Jet3} = 13\,\text{GeV}$. The missing

**Figure 5.12:** *The signal selection efficiencies for the $jjj\!\!\!/P_\perp$ channel at $\sqrt{s} = 301\,GeV$ (left) and $\sqrt{s} = 319\,GeV$ (right) as a function of the stop and the sbottom mass. The $\!\!\!R_p$ coupling $\lambda'_{131}$ is set to $0.3$. The light points indicate the simulated points in the stop and sbottom mass grid.*
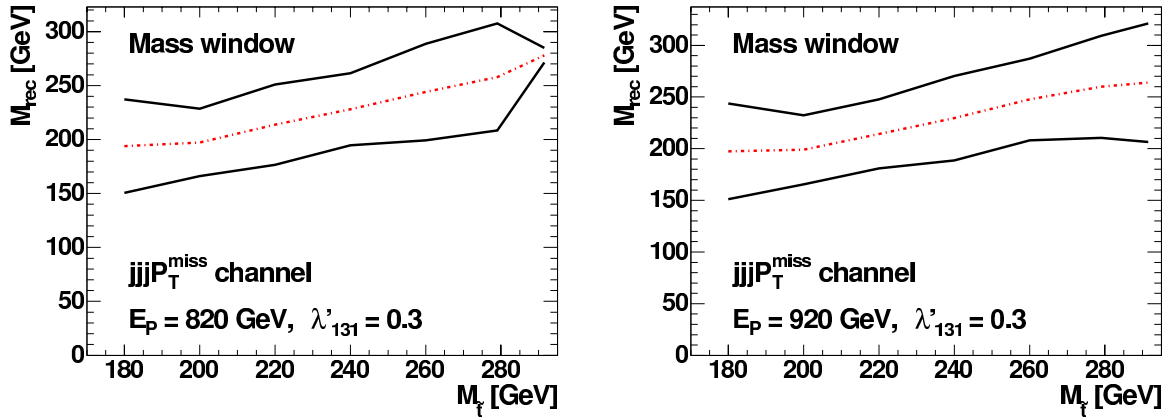


**Figure 5.13:** *The adjusted mass windows for the $jjj\!\!\!/P_\perp$ channel at $\sqrt{s} = 301\,GeV$ (left) and $\sqrt{s} = 319\,GeV$ (right). The hashed lines indicate the mean values of the calculated reconstructed mass windows. The $\!\!\!R_p$ coupling $\lambda'_{131}$ is set to $0.3$.*

transverse momentum of the event amounts to $\!\!\!/P_\perp = 72\,$GeV. Because of its large reconstructed mass of $M_{rec} = 221\,$GeV, this event is contained in the calculated mass window over the whole stop mass range, *i.e.* for each stop mass which is computed in the $jjj\!\!\!/P_\perp$ channel (see figure 5.13). Thus, this example event could arise from both a Standard Model process or a stop decaying bosonically. The muon track which can be seen in the display of the muon system belongs to one of the jets. It is not attributed to an identified muon candidate since it does not fulfil the muon identification criteria.
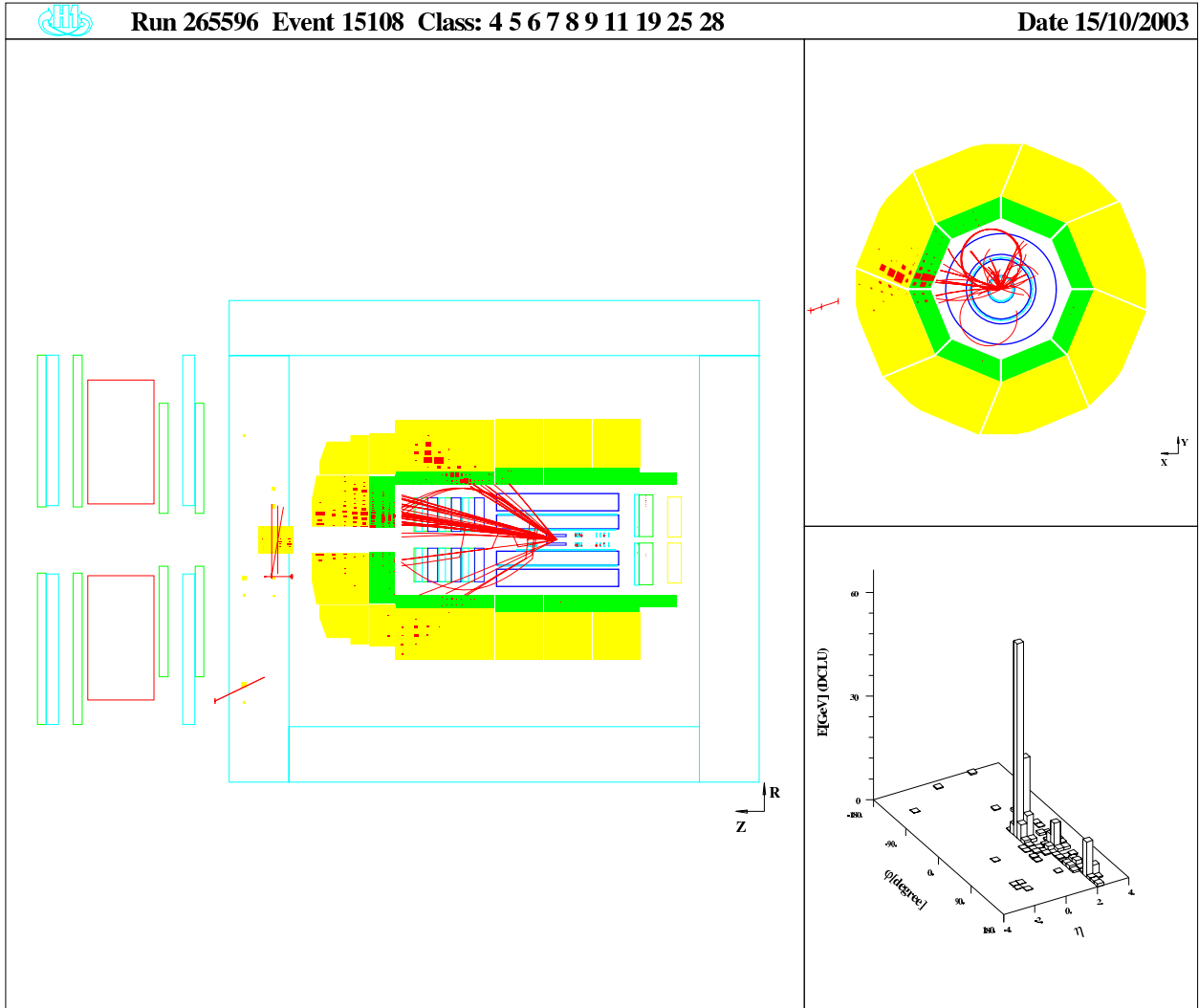
**Figure 5.14:** *The event display of an example event observed in the $jjj\mathbb{P}_\perp$ channel with $P_T^{Jet1} = 60\,GeV$, $P_T^{Jet2} = 24\,GeV$, $P_T^{Jet3} = 13\,GeV$, $\mathbb{P}_\perp = 72\,GeV$ and $M_{rec} = 221\,GeV$.*

# 5.3 The $\mathcal{R}_p$ stop decay channel $\tilde{t} \to ed$

Events in which stop quarks decay into an electron and a quark via $R$–parity violating processes are characterised by high $Q^2$ NC DIS–like topologies. The momentum transfer squared, $Q^2$, is obtained from the scattered electron (see chapter 4.4). Both the stop decay and the NC DIS final states consist of a jet and an electron with high transverse momenta.

## 5.3.1 Event selection

The selection criteria for the $\tilde{t} \to ed$ channel are the following:
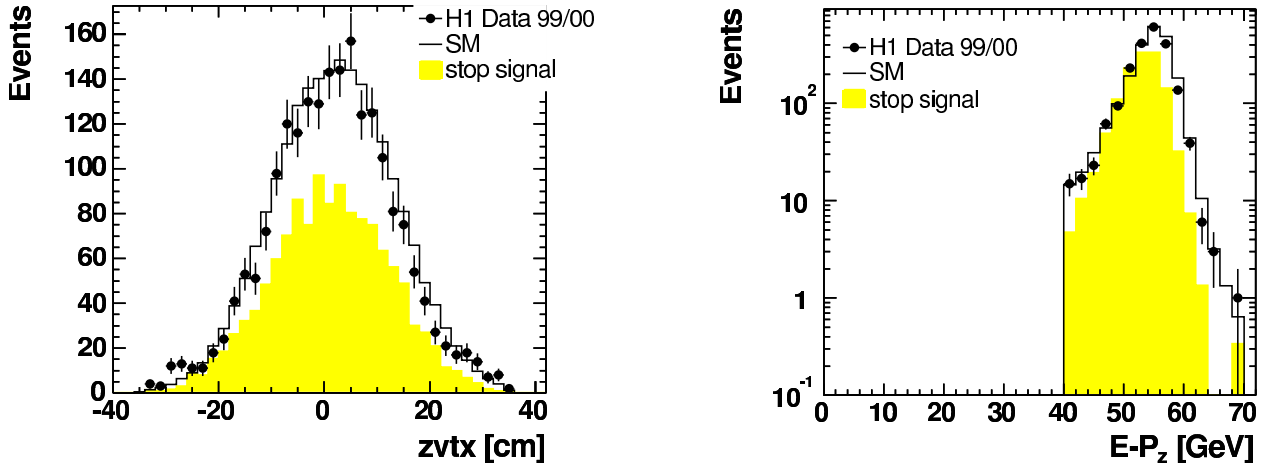
**Figure 5.15:** *The control distributions of the quantities $z_{vtx}$ (left) and $\sum_i (E_i - P_{z,i})$ (right) in the $ed$ channel for the 1999/2000 $e^+ p$ H1 data sample. The filled histograms indicate the stop signal in arbitrary normalisation.*

- The allowed longitudinal momentum loss in the direction of the incident electron is limited by requiring $40\,\text{GeV} < \sum_i (E_i - P_{z,i}) < 70\,\text{GeV}$.

- An electron must be found with $P_T^e > 20\,\text{GeV}$ within the polar angle range $5° < \theta_e < 120°$.

- A jet must be found with $P_T^{Jet} > 20\,\text{GeV}$ and with polar angle $7° < \theta_{Jet} < 140°$.

- The missing transverse momentum and $\sqrt{P_T^e}$ must fulfil $P\!\!\!/_\perp / \sqrt{P_T^e} < 4\sqrt{\text{GeV}}$, which takes into account the energy resolution of the LAr calorimeter.

- Only events within the kinematic range $Q_e^2 > 2500\,\text{GeV}^2$ are considered.

- The selection is restricted to $0.1 < y_e < 0.9$.

  Low values of $y_e$ are excluded since the resolution in the mass $M_e$ decreases with decreasing $y_e$. High values of $y_e$ are excluded to avoid the region where migration effects due to QED radiation in the initial state are largest. Background from photoproduction where a jet is misidentified as an electron, is also suppressed by this cut.

Figure 5.15 shows the control distributions of the variables $z_{vtx}$ (left) and $\sum_i (E_i - P_{z,i})$ (right) for the 1999/2000 $e^+ p$ H1 data sample. The distributions of the data are in good agreement with the SM expectation. Both data and SM background have a peak at $\sum_i (E_i - P_{z,i}) \approx 55\,\text{GeV}$, as expected for NC DIS processes. The filled histograms indicate the stop signal in arbitrary normalisation.

Since in the $ed$ channel NC DIS–like topologies are investigated, the stop mass can be reconstructed and is obtained from the scattered electron according to equation 2.45 by

$$M_e = \sqrt{x_e s}. \tag{5.7}$$
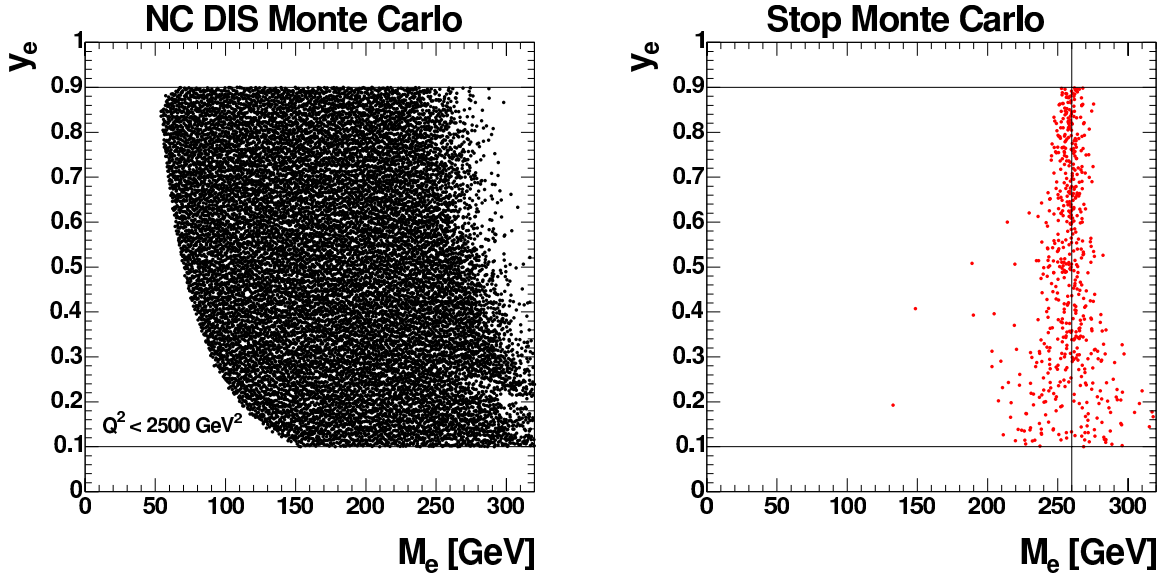
**Figure 5.16:** *The distributions of Monte Carlo events in the $(y_e, M_e)$–plane at $\sqrt{s} = 319\,GeV$ for the NC DIS process (left) and the SUSY signals of a stop of mass $260\,GeV$ decaying via $\not{R}_p$ into $e + d$. The cuts on $y_e$ are indicated by the horizontal lines.*

Here, the Bjorken variable $x_e$ is related to the other kinematic quantities by $Q_e^2 = x_e y_e s$ (equation 2.11). Stop decays via $\not{R}_p$ lead to a resonance peak in the $M_e$ distribution. The resolution in $M_e$ for stop quarks is found to be between $5\,GeV$ and $9\,GeV$, depending on the stop mass. It degrades towards higher invariant masses.

Stop quarks which are produced in the s–channel decay isotropically in their rest frame leading to a flat $d\sigma/dy$ distribution, contrasting with that of NC DIS events[1]. In addition, the distributions of the events in mass $M_e$ and $y_e$ are different for the SUSY signal and the NC DIS background. In figure 5.16, the differences in the $M_e$ and $y_e$ distributions are illustrated in 2–dimensional plots for Monte Carlo events arising from NC DIS (left) and from the $\not{R}_p$ stop decay (right). The stop mass in this example is $260\,GeV$ which is indicated by the vertical line. In both plots, the cuts on $y_e$ are indicated by horizontal lines. The sharp edge on the left side of the NC DIS Monte Carlo arises from the requirement on $Q_e^2$.

In order to maximise the signal sensitivity, a mass dependent lower $y_e$–cut is applied, chosen as in [5]. This cut exploits the differences in the $M_e$ and $y_e$ distributions between the SUSY signal and the NC DIS background. The lower $y_e$–cut which is applied in the $ed$ channel is illustrated in figure 5.17 as a function of the mass $M_e$. For low stop masses, the lower $y_e$–cut values are quasi stable, but above stop masses of about $150\,GeV$, the $y_e$–cut values decrease with the mass. An interpolation fit between the optimised points is applied. For details on the optimisation

---
[1]The $d\sigma/dy \sim y^{-2}$ distribution of NC DIS events can be obtained for the dominant QED contribution from equations 2.11 and 2.12.
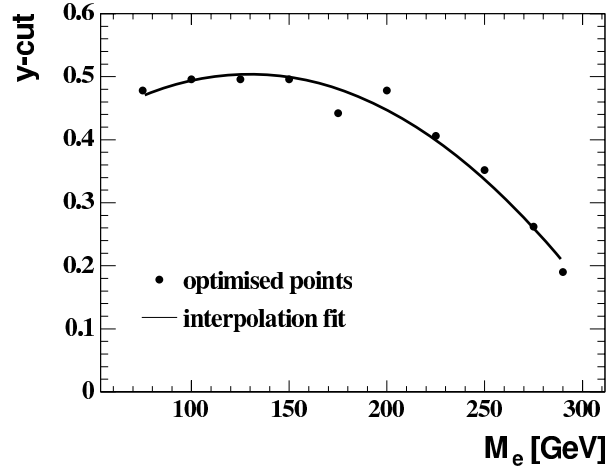
**Figure 5.17:** *The lower $y_e$–cut as chosen in [5] as a function of the invariant stop mass.*

procedure see [91].

The distributions of the variables $y_e$ and $Q_e^2$ for data, SM expectation and the stop signal are shown in figure 5.18 before (top) and after (bottom) the lower $y_e$–cut is applied. The small deficit in the data around $Q_e^2 = 15000\,\mathrm{GeV}^2$ can be explained by statistical fluctuations and has also been observed in other analyses by H1 [83,92].

The $M_e$ spectra for data and for the SM expectation are obtained after the lower $y_e$–cut is applied. They are shown in figure 5.19 d) for the entire H1 $e^+p$ data sample. No significant deviation from the SM is found. In particular at masses above $\sim 180\,\mathrm{GeV}$ where the stop signal is searched for, no significant peak is observed in the data. The signal from a hypothetical stop of mass $260\,\mathrm{GeV}$ in arbitrary normalisation is illustrated by the dashed histogram. A total of $1100$ events are found in the $e^+p$ data set, while $1120 \pm 131$ are expected from SM processes, mainly from NC DIS events. The number of events and the SM expectation can be found in table 5.2.

## 5.3.2 Signal selection efficiencies and mass windows

The stop selection efficiencies are obtained as a function of the stop mass and the Yukawa coupling $\lambda'_{131}$. In the $ed$ channel, the typical stop signal efficiency is about $30\%$–$45\%$. Figure 5.20 illustrates these efficiencies for $\sqrt{s} = 301\,\mathrm{GeV}$ (left) and $\sqrt{s} = 319\,\mathrm{GeV}$ (right) as a function of the stop mass. Here, the $\not{R}_p$ coupling $\lambda'_{131}$ is again chosen to be $0.3$.

The adjusted mass windows determined with the sliding mass window method are shown in figure 5.21 for $\sqrt{s} = 301\,\mathrm{GeV}$ (left) and $\sqrt{s} = 319\,\mathrm{GeV}$ (right). The $\not{R}_p$ coupling $\lambda'_{131}$ set to $0.3$. The mean values of the calculated invariant mass windows are indicated by the hashed lines. In the $ed$ channel, the sliding mass window method (see section ) is also applied in order to further reduce the contribution from the NC DIS background in the mass dependent limit calculation. At
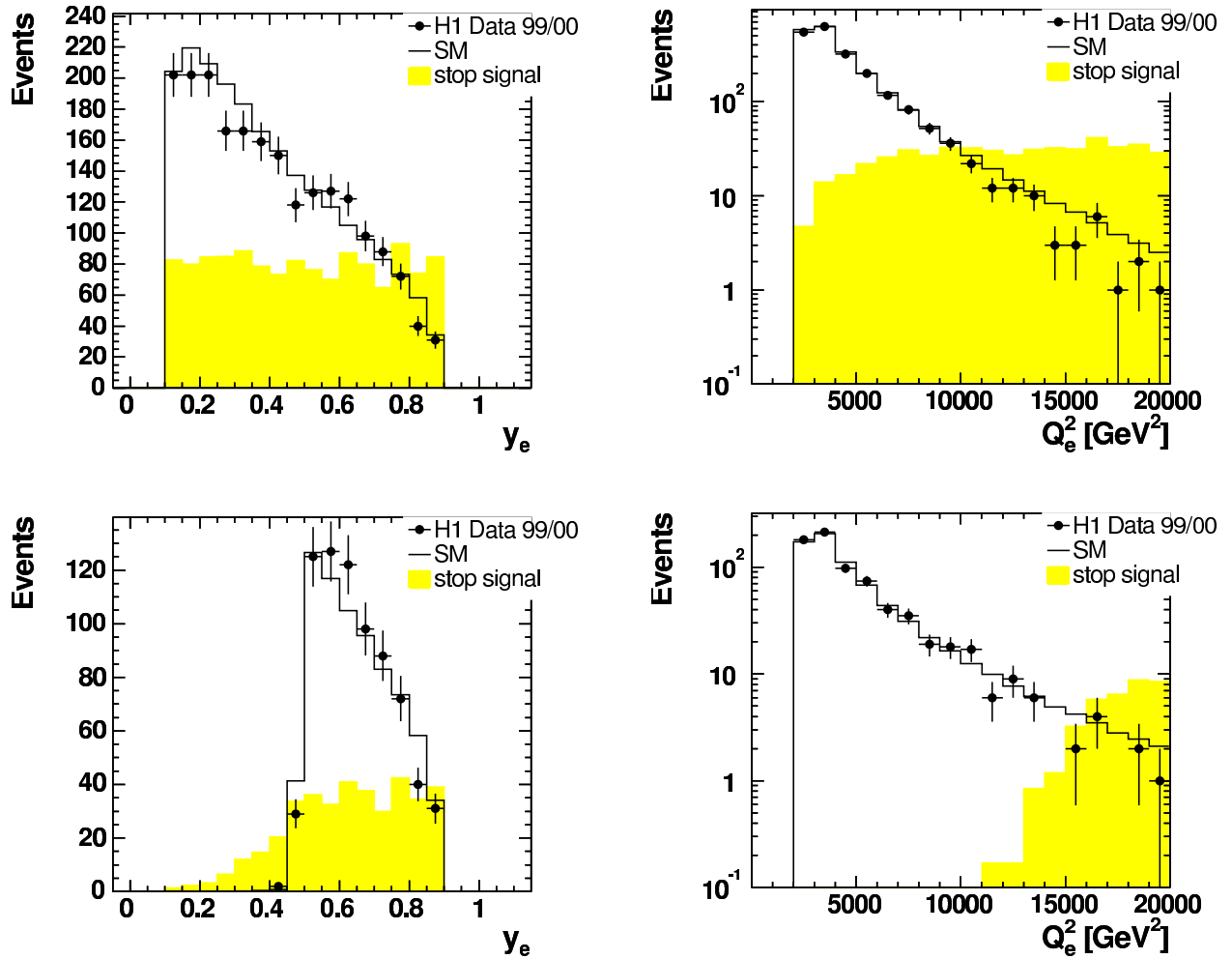
**Figure 5.18:** *The control distributions of the variables $y_e$ and $Q_e^2$ for the 1999/2000 $e^+p$ H1 data sample in the $ed$ channel before (top) and after (bottom) the lower $y_e$–cut is applied. The filled histograms indicate the stop signal in arbitrary normalisation.*

low stop masses, the width of the mass windows is very small but it increases with the invariant mass $M_e$.
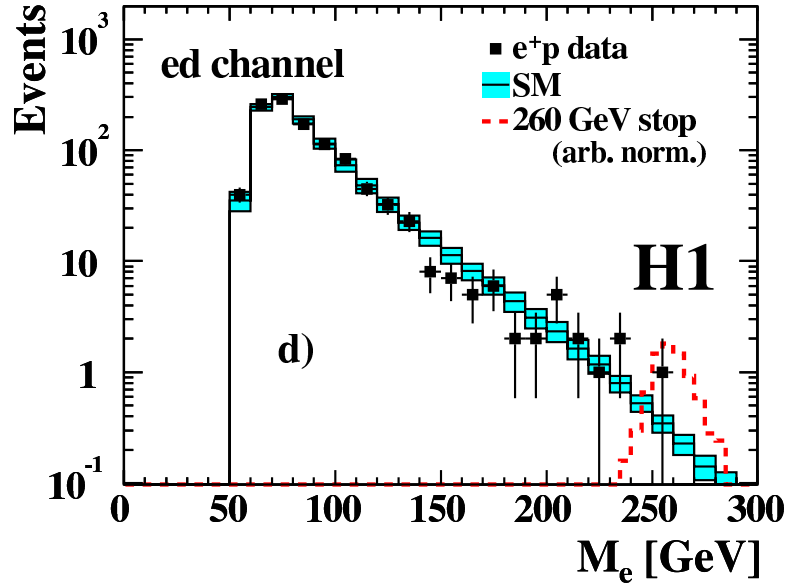
**Figure 5.19:** *The $M_e$ distribution for the $e^+p$ H1 data set of the $ed$ channel. The data are compared with the SM expectation with the systematic uncertainties shown as the shaded band. The expected signal from a stop with mass $260\,GeV$ with arbitrary normalisation. It is indicated by the dashed histogram.*
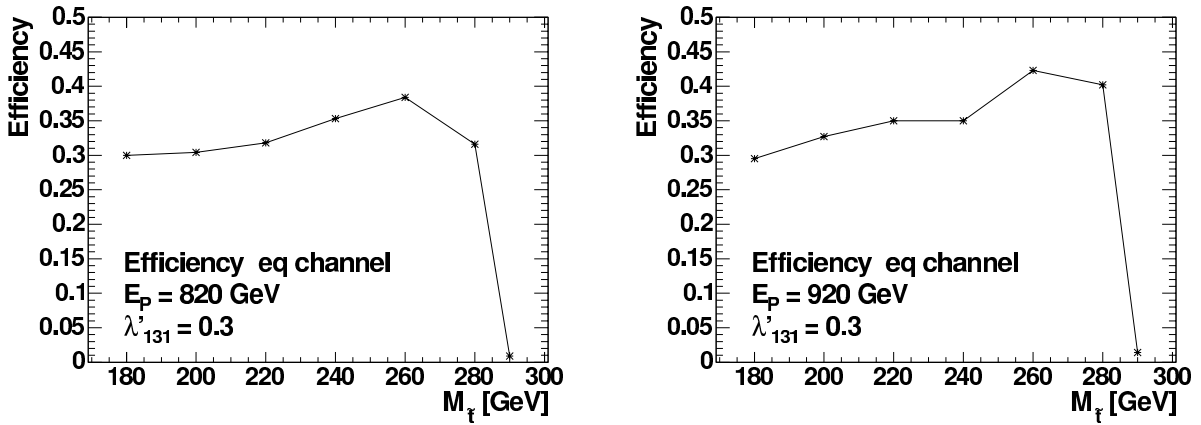


**Figure 5.20:** *The signal selection efficiencies for the $ed$ channel at $3\sqrt{s} = 01\,GeV$ (left) and $\sqrt{s} = 319\,GeV$ (right) as a function of the stop mass. The $\not{R}_p$ coupling $\lambda'_{131}$ is set to $0.3$.*

# 5.4   Selection summary

In table 5.2, the total numbers of selected events and the SM expectation are summarised for the four investigated stop decay topologies in $106\,\text{pb}^{-1}$ of H1 data in positron–proton scattering. The numbers are given for the 1994–1997 H1 data sample, the 1999/2000 $e^+p$ H1 data sample
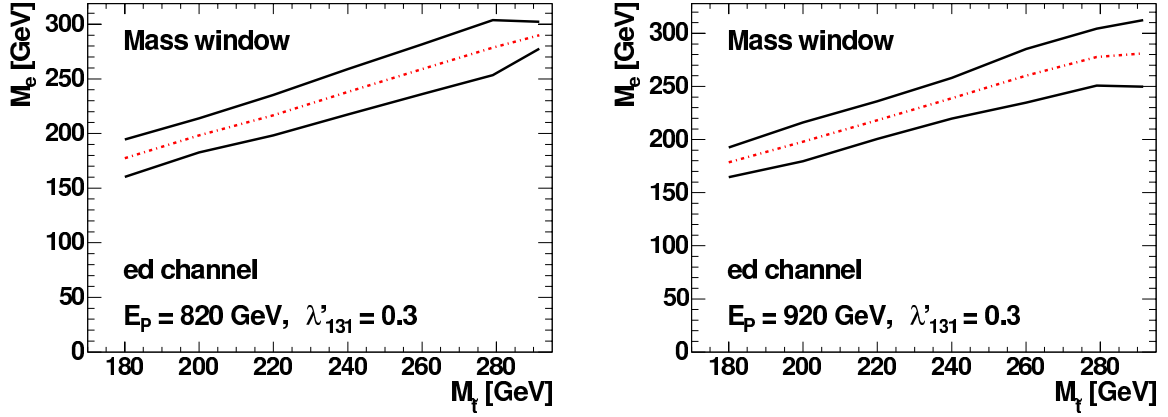
**Figure 5.21:** *The adjusted mass windows determined with the sliding mass window method for the $ed$ channel at $\sqrt{s} = 301$ GeV (left) and $\sqrt{s} = 319$ GeV (right). The hashed lines indicate the mean values of the calculated invariant mass windows. The $\not{R}_p$ coupling $\lambda'_{131}$ is set to $0.3$.*

and the combined data sample. For the $je\not{P}_\perp$ channel and $j\mu\not{P}_\perp$ channel, the SM expectations arising from $W$ production are given in brackets. The selection cuts of the decay channels ensure that less than $0.1\%$ of the SM background or stop signal events contribute to more than one selection channel. Moreover, all data events contribute to only one selection channel. Therefore, explicit cuts on the exclusivity of the selection channels for the data, the SM background or the stop signal are not necessary in this analysis.

No significant deviation from the SM prediction can be observed; two of the three decay channels resulting from bosonic stop decay modes and the $\not{R}_p$ decay channel are in good agreement with the SM expectation. The slight excess which is observed in the $j\mu\not{P}_\perp$ channel is discussed in section 6.1.

| Channel | $\sqrt{s} = 301\,\text{GeV}$ | | $\sqrt{s} = 319\,\text{GeV}$ | | combined | |
|---|---|---|---|---|---|---|
| | data | SM expectation | data | SM expectation | data | SM expectation |
| $je\not{P}_\perp$ | 1 | $1.16 \pm 0.28$ ($W$: $0.75 \pm 0.12$) | 2 | $2.68 \pm 0.64$ ($W$: $1.80 \pm 0.29$) | 3 | $3.84 \pm 0.92$ ($W$: $2.55 \pm 0.41$) |
| $j\mu\not{P}_\perp$ | 4 | $0.84 \pm 0.14$ ($W$: $0.57 \pm 0.09$) | 4 | $1.85 \pm 0.33$ ($W$: $1.36 \pm 0.22$) | 8 | $2.69 \pm 0.47$ ($W$: $1.93 \pm 0.31$) |
| $jjj\not{P}_\perp$ | 1 | $1.91 \pm 0.54$ | 4 | $4.33 \pm 1.21$ | 5 | $6.24 \pm 1.74$ |
| $ed$ | 366 | $384 \pm 45$ | 734 | $736 \pm 86$ | 1100 | $1120 \pm 131$ |

**Table 5.2:** *The total number of selected events for the $e^+p$ H1 data set of the stop decay channels at $\sqrt{s} = 301\,\text{GeV}$, $\sqrt{s} = 319\,\text{GeV}$ and the combined data set. For the $je\not{P}_\perp$ channel and the $j\mu\not{P}_\perp$ channel the SM expectation arising from $W$–production are given in brackets.*

# 6
# Interpretation of the Results

In this chapter, the results of the analysis of the final state topologies considered in this thesis (see chapter 5) are interpreted in terms of the Minimal Supersymmetric Standard Model. A stop signal cross section, depending on the stop mass, is calculated for the final state topologies classified as a bosonic stop decay. First, an interpretation of the bosonic stop decay channels is given, then the method of calculating exclusion limits is presented.

Although the slight excess in the $j\mu P_\perp$ channel might arise from a stop decaying bosonically, the presence of a stop is not confirmed by the observation in the other three selection channels. Thus, the analysis results of chapter 5 are used to obtain exclusion limits in the MSSM with $\not{R}_p$ . Finally, a scan of the SUSY parameter space is performed and the resulting exclusion limits are discussed.

## 6.1    Interpretation of bosonic stop decay searches

In the $j\mu P_\perp$ channel, a slight excess of events compared with the SM expectation is observed, confirming the previous H1 analysis of isolated lepton events [6]. All other channels are in good agreement with the SM (see table 5.2).

Assuming the presence of a stop of mass $M_{\tilde{t}}$ decaying bosonically, the observed event yields are used to determine the allowed range for a stop production cross section $\sigma_{\tilde{t}}$. This signal cross section for different stop masses is determined from the number of observed and expected events in the corresponding mass or transverse mass bin, $N_{data}$ and $N_{SM}$ (see chapter 5.1.2), for each bosonic stop decay channel. The cross section is calculated by folding in the signal efficiency $\epsilon$, the $\tilde{t}$ and $W$ branching ratios $BR_{\tilde{t} \to \tilde{b}W} \cdot BR_{W \to f\bar{f}'}$ and taking into account the integrated
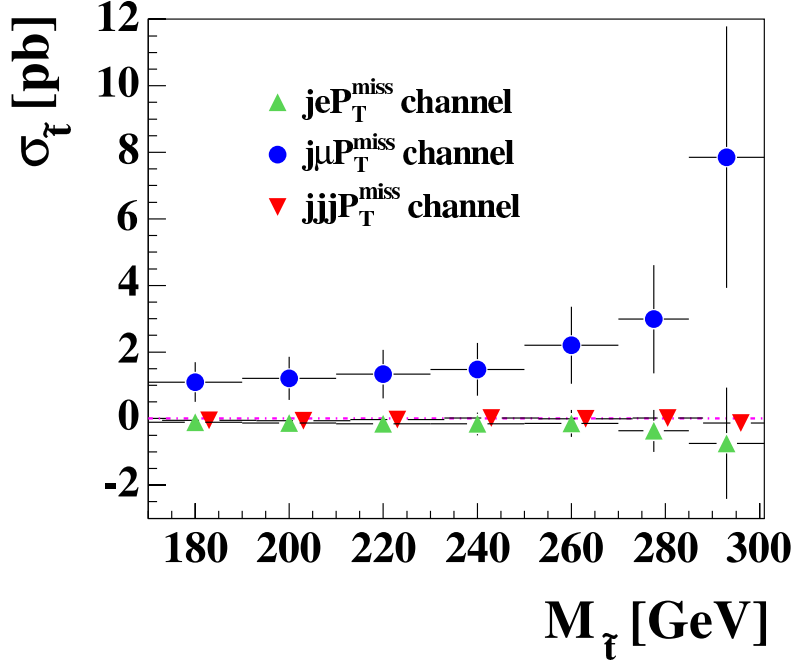
**Figure 6.1:** *The stop cross sections $\sigma_{\tilde{t}}$ for all bosonic stop decay channels as a function of the stop mass.*

luminosities $\mathcal{L}_{301}$ and $\mathcal{L}_{319}$:

$$\sigma_{\tilde{t}}(M_{\tilde{t}}) = \frac{N_{data} - N_{SM}}{\epsilon \cdot BR_{\tilde{t} \to \tilde{b}W} \cdot BR_{W \to f\bar{f}'}} \cdot \frac{1}{r_\sigma \cdot \mathcal{L}_{301} + \mathcal{L}_{319}}. \qquad (6.1)$$

Here, $\mathcal{L}_{301}$ and $\mathcal{L}_{319}$ are the integrated luminosities for the centre–of–mass energies $\sqrt{s} = 301$ GeV and $\sqrt{s} = 319$ GeV, respectively. The variable $r_\sigma$ is the ratio of the cross sections at $\sqrt{s} = 319$ GeV and $\sqrt{s} = 301$ GeV. The branching ratio for $\tilde{t} \to \tilde{b}W$ is assumed to be $BR_{\tilde{t} \to \tilde{b}W} = 100\%$. If $N_{data}$ and $N_{SM}$ are identical, the cross section is expected to be zero.

The uncertainty on the cross section, $\Delta\sigma_{\tilde{t}}$, is determined from the statistical errors on the numbers of observed events and the theoretical and experimental uncertainties on the SM prediction which are described in chapter 4.8. The error $\Delta\sigma_{\tilde{t}}$ of the cross section is dominated by the statistical error. The uncertainties on the cross sections are added in quadrature for each error source.

In figure 6.1, the calculated cross sections and its errors are shown for all bosonic stop decay channels as a function of the stop mass. In order to obtain the allowed cross section regions, a fit is applied which gives the envelope of the values $\sigma_{\tilde{t}} + \Delta\sigma_{\tilde{t}}$ and $\sigma_{\tilde{t}} - \Delta\sigma_{\tilde{t}}$ as a function of the stop mass. As a result, the bands in figure 6.2 represent the allowed cross section regions $\sigma_{\tilde{t}} \pm \Delta\sigma_{\tilde{t}}$ for all bosonic stop decay channels. The band for the $jjj\not{P}_\perp$ channel is narrow (*i.e.* the error is small) due to the large branching ratio $BR_{W \to q\bar{q}'}$.

From both figures (6.1 and 6.2) it can be seen that the excess observed in the $j\mu\not{P}_\perp$ channel
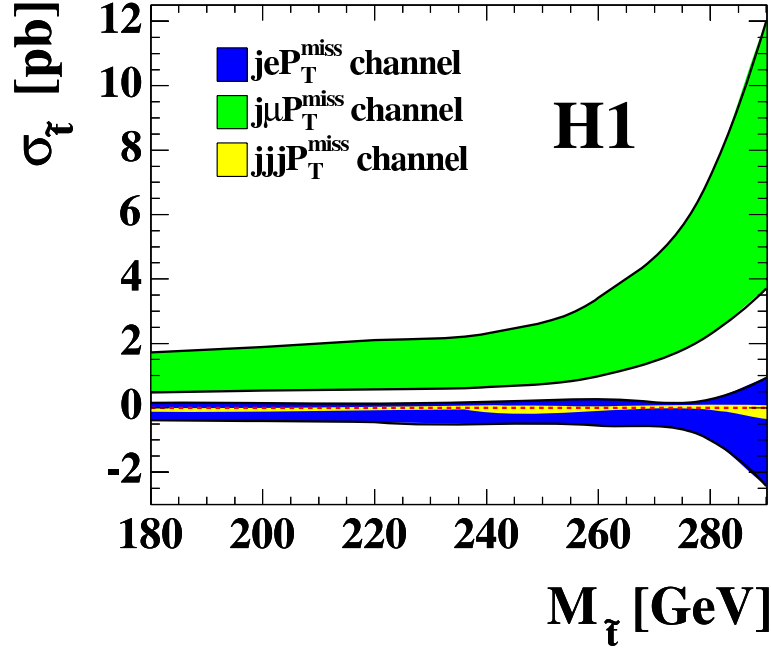
**Figure 6.2:** *The bands representing the allowed stop cross section regions $\sigma_{\tilde{t}} \pm \Delta\sigma_{\tilde{t}}$ as a function of the stop mass as obtained from the analysis for each bosonic stop decay channel.*

cannot be interpreted as a stop signal since it is not supported by the other decay modes. For instance, the probability that the observed event rate in the $jjj\!\!\!/P_\perp$ channel fluctuates upwards to produce at least the number of events expected on the basis of the signal in the $j\mu\!\!\!/P_\perp$ channel is around $0.5\%$ to $1\%$, depending slightly on the stop mass. This probability corresponds roughly to a compatibility of the $j\mu\!\!\!/P_\perp$ and $jjj\!\!\!/P_\perp$ channels at the $2\sigma$ level which has also been observed in other analyses by H1 [93]. Hence, exclusion limits on the $\not{R}_p$ SUSY model described in section 2.5 are derived.

# 6.2 Modified frequentist confidence levels

In the present analysis, a modified frequentist approach and its implementation described in [94] is used. This method is based on likelihood ratios and has also been used in the LEP searches for the Higgs boson [37, 95, 96, 97]. The basic concepts of this method of calculating modified frequentist confidence levels are summarised in the following.

## Likelihood ratios

The likelihood ratio $Q$ is a test statistic (or *discriminator*) which is introduced to distinguish signal–like results from background–like results of a search with $n$ independent selection channels. For

this purpose, a signal + background $(s + b)$ hypothesis and the background–only $(b)$ hypothesis are assumed. In the selection channel $i$, the likelihood ratio $Q_i$ is defined as the ratio of the Poisson probabilities for observing the $s + b$ and the $b$–only hypothesis. Thus, the likelihood ratio of this selection channel can be written as

$$Q_i = \frac{e^{-(s_i+b_i)}(s_i + b_i)^{d_i}}{d_i!} \bigg/ \frac{e^{-b_i}b_i^{d_i}}{d_i!}, \tag{6.2}$$

where $b_i$ is the estimated SM background and $d_i$ is the number of observed candidate events. The expected number of signal events in the selection channel $i$ is given by $s_i = N \cdot (\epsilon \cdot BR)_i$. Here, $N$ is the total number of simulated signal events and $(\epsilon \cdot BR)_i$ is the product of the efficiency and the branching ratio of this selection channel.

The total likelihood ratio for a set of $n$ independent channels is defined as the product of the likelihood ratios of the selection channels:

$$Q = \prod_{i=1}^{n} Q_i. \tag{6.3}$$

## Confidence levels

Confidence levels (CL) are determined using the total likelihood ratio of equation 6.3 which is used as a test statistic. The confidence level $CL_{s+b}$ is defined as the probability that this test statistic would be less than or equal to that observed in the data,

$$CL_{s+b} = P_{s+b}(Q \le Q_{obs}). \tag{6.4}$$

It gives the probability that an ensemble of $s + b$ experiments is more background–like than the observation. A search with downward fluctuating background will set strong exclusion limits on $1 - CL_{s+b}$. Hence, the confidence level $CL_b$ is calculated equivalent to $CL_{s+b}$, assuming the presence of the background only. It can be written as

$$CL_b = P_b(Q \le Q_{obs}) \tag{6.5}$$

and gives the probability that the number of the estimated background events is smaller than or equal to that of the number of observed data candidates.

Figure 6.3 illustrates an example of the probability density functions (p.d.f.) of the test statistic as a function of $-2\ln Q$ [98]. In this example, a hypothetical observed likelihood of $-2\ln Q = -3$ is assumed and the confidence levels $CL_{s+b}$ and $1 - CL_b$ are illustrated. On the left hand side, the $s + b$–like p.d.f. is shown, whereas the $b$–like distribution can be seen on the right hand side. The probability that an ensemble of background–only experiments is more signal–like than the observation is indicated by the region marked as $1 - CL_b$ in the upper histogram. The probability that an ensemble of $s + b$ experiments is more background–like than the observation is indicated by the $CL_{s+b}$ region in the lower histogram.
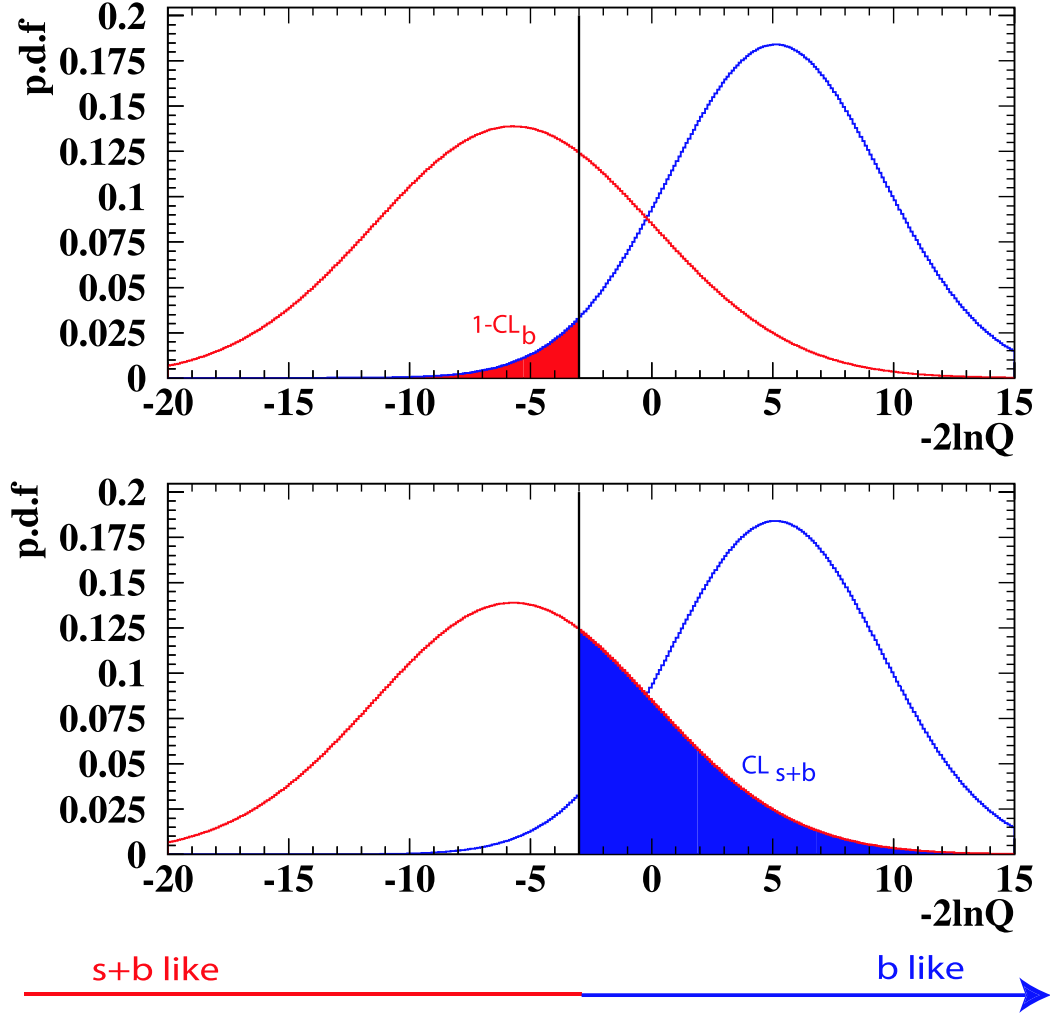
**Figure 6.3:** *An example of probability distribution functions (p.d.f.) for background–only (right side) and signal + background (left side) experiments. The shaded area in the upper histogram, $1 - CL_b$, gives a measurement of the compatibility with the background–only hypothesis while the shaded area in the lower histogram, $CL_{s+b}$, gives a measurement of the compatibility with the signal + background hypothesis. The plot is taken from [98].*

The CL used to obtain exclusion limits is the CL of the modified frequentist approach. It is given by

$$CL_s = \frac{CL_{s+b}}{CL_b}.$$ (6.6)

An upper limit $N_{lim}$ on the number of events coming from stop production is calculated at the $95\%$ confidence level using a confidence level computation program [94, 99]. The limit is determined such that $CL_s \leq 0.05$ for $N \geq N_{lim}$.

The systematic uncertainties on the signal and the SM background expectations are both taken into account in the limit calculation. For details on the computation see [94].

# 6.3   Derivation of exclusion limits

The results from the selection channels considered in this analysis are combined to derive constraints in the MSSM. For a given set of parameters within this model, the full supersymmetric mass spectrum, in particular the stop and sbottom masses, and the branching ratios of all stop and sbottom decay modes are calculated with the SUSYGEN package [54, 55]. Each considered selection channel contributes to the calculation of the upper limit $N_{lim}$ (see section 6.2) via:

- the numbers of observed events in the data sets within the sliding mass bins (transverse mass bins) around the calculated stop mass (transverse mass), as defined in chapter 5.1.2,

- the corresponding numbers of events expected from SM background processes and their experimental and theoretical uncertainties,

- the signal efficiencies for all stop decay modes in all selection channels and their errors (see chapter 2.6),

- the calculated branching ratios of all stop decay modes.

Finally, $N_{lim}$ is translated into a bound on the stop production cross section $\sigma_{lim}$. The given set of model parameters is excluded if it predicts a cross section which is larger than $\sigma_{lim}$. Theoretical errors on the signal cross section are included in the systematic uncertainties of the signal efficiencies (see chapter 4.8). Besides it has been tested that the deduced limits are rather insensitive to systematic uncertainties on the SM expectation.

# 6.4   Exclusion limits in the MSSM

The interpretation of the results is performed within a Minimal Supersymmetric Standard Model (see chapter 2.4.1) in which the masses of the neutralinos, charginos and gluinos, as well as the couplings between any two SUSY particles and a standard model fermion or boson, are determined by the usual MSSM parameters: the "mass" term $\mu$ which corresponds to the Higgs boson mass parameter in the SM, the soft SUSY breaking mass parameters $M_1$, $M_2$ and $M_3$ for $U(1)$, $SU(2)$ and $SU(3)$ gauginos and $\tan\beta$, the ratio of the vacuum expectation values of the two neutral scalar Higgs fields. The usual GUT relations between $M_1$, $M_2$ and $M_3$ given in equations 2.25 and 2.26 are assumed to hold. Thus, only the parameter $M_2$ is arbitrary and chosen to be $1000\,\text{GeV}$. All sfermion masses as well as the squark mixings $\theta_{\tilde{t}}$ and $\theta_{\tilde{b}}$ and the soft SUSY breaking trilinear couplings $A_t$ and $A_b$ are free parameters in this model. The higgsino and slepton masses and the squark masses of the first two generations are chosen to be 1 TeV. The squark mixing parameters, masses and the SUSY parameters $A_t$, $A_b$, $\tan\beta$ and $\mu$ are related by the equations 2.40 and 2.41. These parameters are investigated as described in the following.

# 6.4.1   Scan of the SUSY parameter space

In order to investigate systematically the dependence of the sensitivity on the MSSM parameters, a scan of the SUSY parameter space is performed. The parameters $\mu$, $M_2$ and $\tan\beta$ are used to determine the masses and couplings of the neutralinos and charginos as explained in chapter 2.4.1. Thus, especially the parameters $\mu$ and $M_2$ have to be restricted to high values in order to suppress kinematically the usual stop and sbottom decays into gauginos.

The SUSY parameter space is selected such that the combined branching ratio fulfils

$$BR_{tot} = BR_{\tilde{t} \to ed} + BR_{\tilde{t} \to \tilde{b}W} \cdot BR_{\tilde{b} \to \nu_e d} > 85\%. \tag{6.7}$$

The choice of $BR_{tot} > 85\%$ determines the values of $M_2$ and $\mu$ for which a bosonic stop decay can occur. In figure 6.4, $BR_{tot}$ is shown in a 2–dimensional plot as a function of the SUSY parameters $M_2$ and $\mu$. Here, the parameter $\tan\beta$ is set to 10. The mixing angles do not have a large influence on $BR_{tot}$ and are fixed to $\theta_{\tilde{t}} = \theta_{\tilde{b}} = 1.2$ in this example. Shown are the regions in which the branching ratio is larger than $10\%$, $50\%$ and $85\%$. In large parts of the latter region, the branching amounts to $100\%$ and decreases only at the edges of the displayed area. It can be seen that for values of $M_2$ and $\mu$ below about $400\,\text{GeV}$ the branching ratio $BR_{tot}$ falls quite steeply from $\sim 100\%$ to a few percent. The parameters $M_2$ and $\mu$ are therefore chosen to be above $400\,\text{GeV}$ in this analysis. These restrictions on the SUSY parameter space lead to a combined branching ratio which is always $BR_{tot} \approx 100\%$. Hence, the exclusion limits are given by the SUSY parameters only and the cut on the branching ratio is a supplementary requirement on the parameter space.

For the scan, the SUSY parameter space is restricted to the following values:

- The parameter $M_2$ is set to $1000\,\text{GeV}$.

  The parameter $\mu$ is restricted to the range $400\,\text{GeV} < \mu < 1000\,\text{GeV}$.

  Both requirements ensure that the masses of the neutralinos, charginos and gluinos are large enough to forbid kinematically fermionic squark decays via their usual gauge couplings.

- The mixing angles $\theta_{\tilde{t}}$ and $\theta_{\tilde{b}}$ are allowed to vary between $0.6$ rad and $1.2$ rad.

  In principle, the choice of the mixing angles is arbitrary but their values are chosen such that they are reliable in terms of resonant stop production and the subsequent bosonic stop decay.

  Higher values of $\theta_{\tilde{t}}$ suppress the stop production cross section which is proportional to $\cos^2\theta_{\tilde{t}}$, according to equation 2.48.

  Higher values of $\theta_{\tilde{b}}$ suppress the branching ratio $BR_{\tilde{t} \to \tilde{b}W}$ which is proportional to $\cos^2\theta_{\tilde{b}}$ (see chapter 2.5.2).

- The ratio of the vacuum expectation values of the Higgs fields $\tan\beta$ is set to $10$ since the sbottom mass can only be quite small if $\tan\beta \gtrsim 10$ [23] (see chapter 2.4.3).
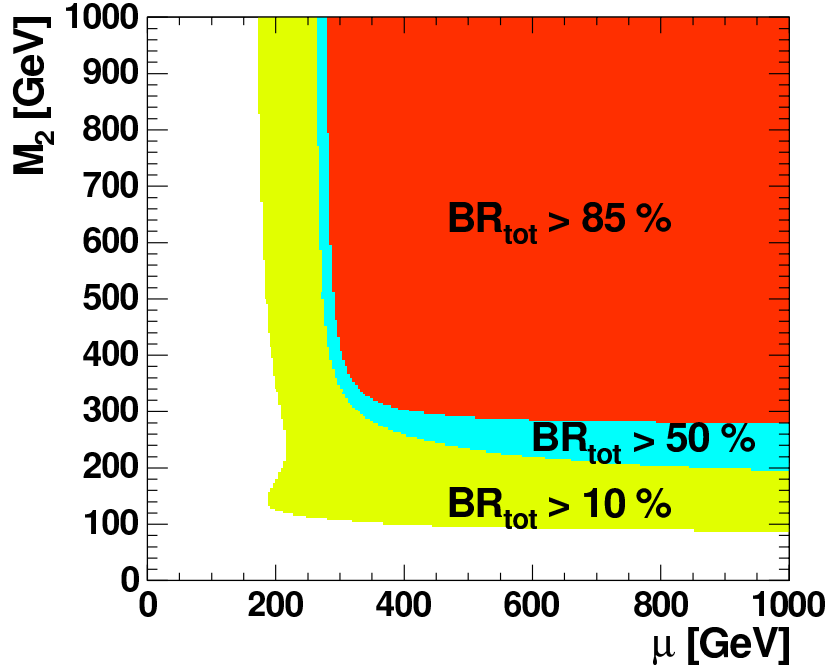
**Figure 6.4:** *The combined branching ratio $BR_{tot}$ as a function of the SUSY parameters $M_2$ and $\mu$ with $\tan\beta = 10$ and $\theta_{\tilde{t}} = \theta_{\tilde{b}} = 1.2$.*

- The trilinear couplings $A_t$ and $A_b$ are needed to determine the masses of the heaviest stop and sbottom, according to equation 2.40, and are set to $A_t = A_b = -100$ GeV.

- The stop and sbottom masses are allowed to vary between $180$ GeV $< M_{\tilde{t}} < 290$ GeV and $100$ GeV $< M_{\tilde{b}} < 210$ GeV (see chapter 2.5.2). Here, the notations $\tilde{t}$ and $\tilde{b}$ are equivalent to $\tilde{t}_1$ and $\tilde{b}_1$, respectively, since the production of the heavier stop is kinematically suppressed (see chapter 2.5.1).

All specific parameter ranges are listed in table 6.1. For the given values of $M_2$, $\tan\beta$, $A_t$ and $A_b$, the parameters $\theta_{\tilde{t}}$, $\theta_{\tilde{b}}$ and $\mu$ are scanned in the $(M_{\tilde{t}}, M_{\tilde{b}})$–plane for fixed values of $\lambda'_{131}$ and in the $(M_{\tilde{t}}, \lambda'_{131})$–plane for $M_{\tilde{b}} = 100$ GeV.

## 6.4.2   Resulting limits

For each point in the 5–dimensional parameter space ($M_{\tilde{t}}$, $M_{\tilde{b}}$, $\theta_{\tilde{t}}$, $\theta_{\tilde{b}}$ and $\mu$), an upper bound on the coupling $\lambda'_{131}$ is obtained. The resulting limits are given for two cases:

- every point in the scanned SUSY parameter space is excluded which gives the strongest exclusion limits,

| SUSY Parameter Range |
|:---:|
| $M_2 = 1000\,\text{GeV}$ |
| $400\,\text{GeV} < \mu < 1000\,\text{GeV}$ |
| $\tan\beta = 10$ |
| $180\,\text{GeV} < M_{\tilde{t}} < 290\,\text{GeV}$ |
| $100\,\text{GeV} < M_{\tilde{b}} < 210\,\text{GeV}$ |
| $0.6\,\text{rad} < \theta_{\tilde{t},\tilde{b}} < 1.2\,\text{rad}$ |
| $A_t = A_b = -100\,\text{GeV}$ |

**Table 6.1:** *The chosen SUSY parameter range in the MSSM.*

- at least one point in the scanned SUSY parameter space is excluded leading to the weakest exclusion limits.

The resulting limits obtained for $\tan\beta = 10$ are shown in figure 6.5 a) and b) in the $(M_{\tilde{t}}, M_{\tilde{b}})$–plane for $\lambda'_{131} = 0.1$ and $\lambda'_{131} = \sqrt{4\pi\alpha_{em}} = 0.3$, respectively, where $\sqrt{4\pi\alpha_{em}} = e$ is the electromagnetic charge and $\alpha_{em}$ denotes the fine structure constant. The two full curves indicate the strongest and the weakest limits on the masses in the parameter space investigated. At $\lambda'_{131} = 0.1$, stop masses $M_{\tilde{t}} \lesssim 250\,\text{GeV}$ can be excluded, while masses $M_{\tilde{t}} \lesssim 275\,\text{GeV}$ are excluded at a Yukawa coupling of electromagnetic strength, i.e. $\lambda'_{131} = 0.3$.

The resulting limits projected on the $(M_{\tilde{t}}, \lambda'_{131})$–plane for $M_{\tilde{b}} = 100\,\text{GeV}$ are shown in figure 6.6. Again, the two full curves indicate the strongest and the weakest limits on $\lambda'_{131}$ in the parameter space investigated. Both figures show the same exclusion limits but in the lower diagram, the coupling $\lambda'_{131}$ is displayed in a logarithmic scale and the curve is smoothed by a fit. For $M_{\tilde{t}} = 200\,\text{GeV}$, couplings $\lambda'_{131} \gtrsim 0.02$ are ruled out and for $M_{\tilde{t}} = 275\,\text{GeV}$ the allowed domain is $\lambda'_{131} \lesssim 0.3$. The kink which can be seen at a stop mass of about $260\,\text{GeV}$ is caused by one event in the $jjj\not{P}_\perp$ channel. This event has a reconstructed mass of roughly $200\,\text{GeV}$. As soon as the stop mass is larger than about $260\,\text{GeV}$, it is not contained in the mass window any more, as can be seen from figures 5.11 and 5.13. Therefore, the event is not taken into account for the limit calculation at high stop masses.

The limits do not significantly depend on $\tan\beta$ or $M_2$, provided that $M_2 > 400\,\text{GeV}$, which has been checked by repeating the analysis with $\tan\beta = 2$ or $M_2 = 400\,\text{GeV}$. This can be seen by comparing the limits in figures 6.5 and 6.6 with those in figures 6.7 and 6.8. Here, the resulting exclusion limits are calculated with $\tan\beta = 2$ and $M_2 = 400\,\text{GeV}$. They differ only very slightly from the limits obtained for $\tan\beta = 10$ and $M_2 = 1000\,\text{GeV}$. For example, in the the $(M_{\tilde{t}}, M_{\tilde{b}})$–plane for $\lambda'_{131} = 0.3$, the strongest limit on the masses is a little worse at $M_{\tilde{b}} \approx 100\,\text{GeV}$.

The exclusion limits on the $\not\!\!R_p$ coupling $\lambda'_{131}$ obtained in this analysis are competitive to those in previous analyses in $\not\!\!R_p$ squark production by H1 [5]. Although the SUSY parameter space is different in both analyses, the qualitative comparison of single limit points can be used as a coarse consistency check. These points have to be in the mass region where the $\not\!\!R_p$ stop decay $\tilde{t} \to ed$ dominates $(M_{\tilde{t}} \approx M_{\tilde{b}} + M_W)$ since this NC DIS–like final state is also considered in the existing squark search.

## Comparison with the general search analysis

In the general search for new phenomena in $ep$ scattering at HERA [52, 71, 70], a model–independent search for deviations from the SM predictions has been performed. In that analysis, events are divided into exclusive event classes according to their final state. The invariant mass and the sum of transverse momentum distributions of all event classes are systematically investigated. A search for new physics signals using a novel statistical algorithm is performed. The statistical significance of the deviations observed in the data are quantified by the probability called $\hat{P}$. Its definition is given in [52].

In order to test the significance of the analysis procedure, a set of pseudo data samples has been investigated using a Monte Carlo technique. The prediction of a specific model for new physics (e.g. the resonant stop production at HERA) is added to the SM prediction. A detailed description of this procedure can be found in [71]. The production of stop quarks via the $\not\!\!R_p$ coupling $\lambda'_{131}$ is tested with $\lambda'_{131} = 0.1$ and $M_{\tilde{b}} = 100$ GeV, using the distributions of the scalar sum of transverse momenta $\sum P_T$ and the invariant mass $M_{all}$ of all objects.

In figure 6.9, the resulting diagrams are shown for the event classes $e$-$j$, $e$-$j$-$\nu$, $\mu$-$j$-$\nu$ and $j$-$j$-$j$-$\nu$ which correspond to the $ed$, $je\not\!\!P_\perp$ , $j\mu\not\!\!P_\perp$ and $jjj\not\!\!P_\perp$ channels, respectively, of the present analysis. The sensitivity for a stop quark decaying bosonically is decreasing with the stop mass, as expected. The exclusion limit at the $95\%$ CL as obtained in the present thesis is given by the hashed vertical line. For $M_{\tilde{t}} = 180$ GeV the sensitivity in the event classes resulting from a bosonic stop decay is very low, whereas the sensitivity in the $e$-$j$ event class is high. This behaviour can be explained by the characteristics of the branching ratios shown in figure 2.13. The branching ratio $BR_{\tilde{t}\to ed}$ is almost $100\%$ at $M_{\tilde{t}} = 180$ GeV and decreases rapidly with the stop mass.

Concluding, the results of the general search analysis show that HERA is sensitive to the production of stop quarks via the $\not\!\!R_p$ coupling $\lambda'_{131}$. These results support the exclusion limits which have been obtained in the present analysis.
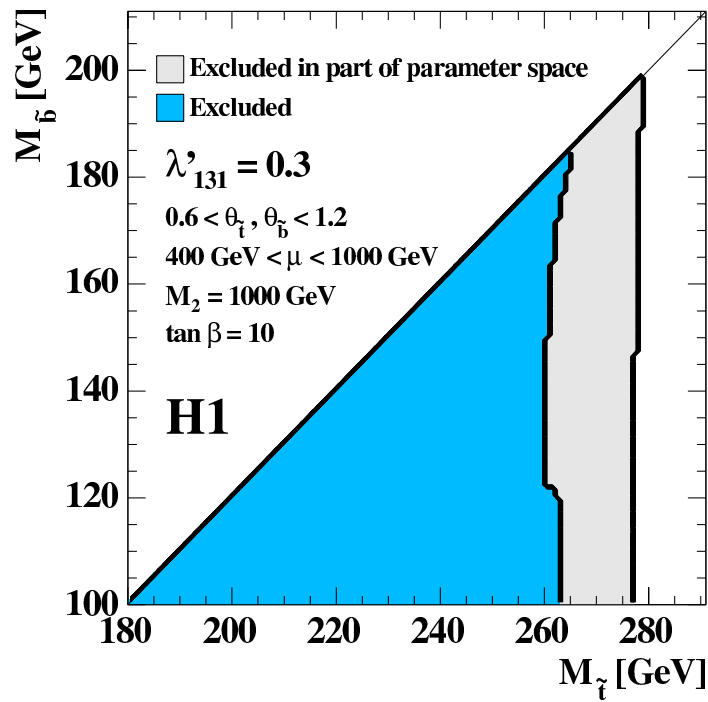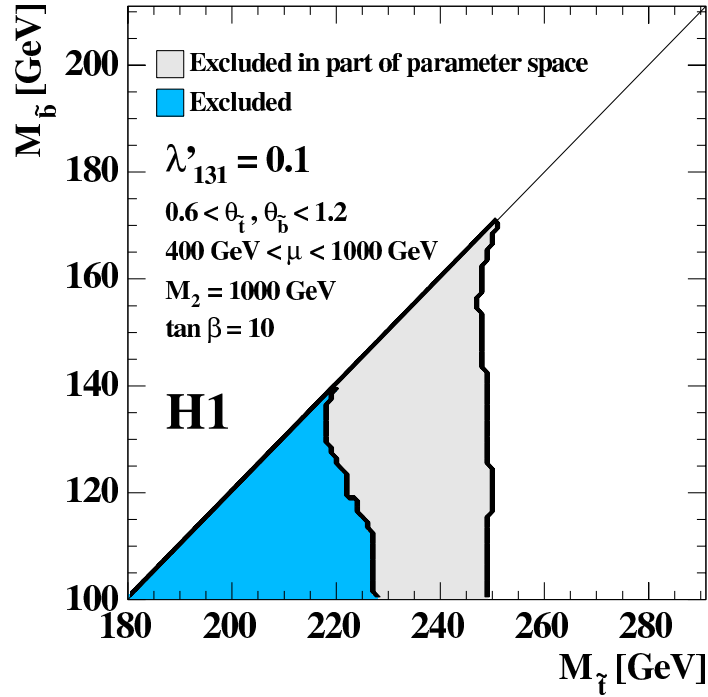
**Figure 6.5:** *The exclusion limits at $95\%$ CL in the $(M_{\tilde{t}}, M_{\tilde{b}})$–plane for a) $\lambda'_{131} = 0.1$ and b) $\lambda'_{131} = 0.3$ from a scan of the MSSM parameter space as indicated in the figures. The two full curves indicate the regions excluded in all or part of the SUSY parameter space investigated.*
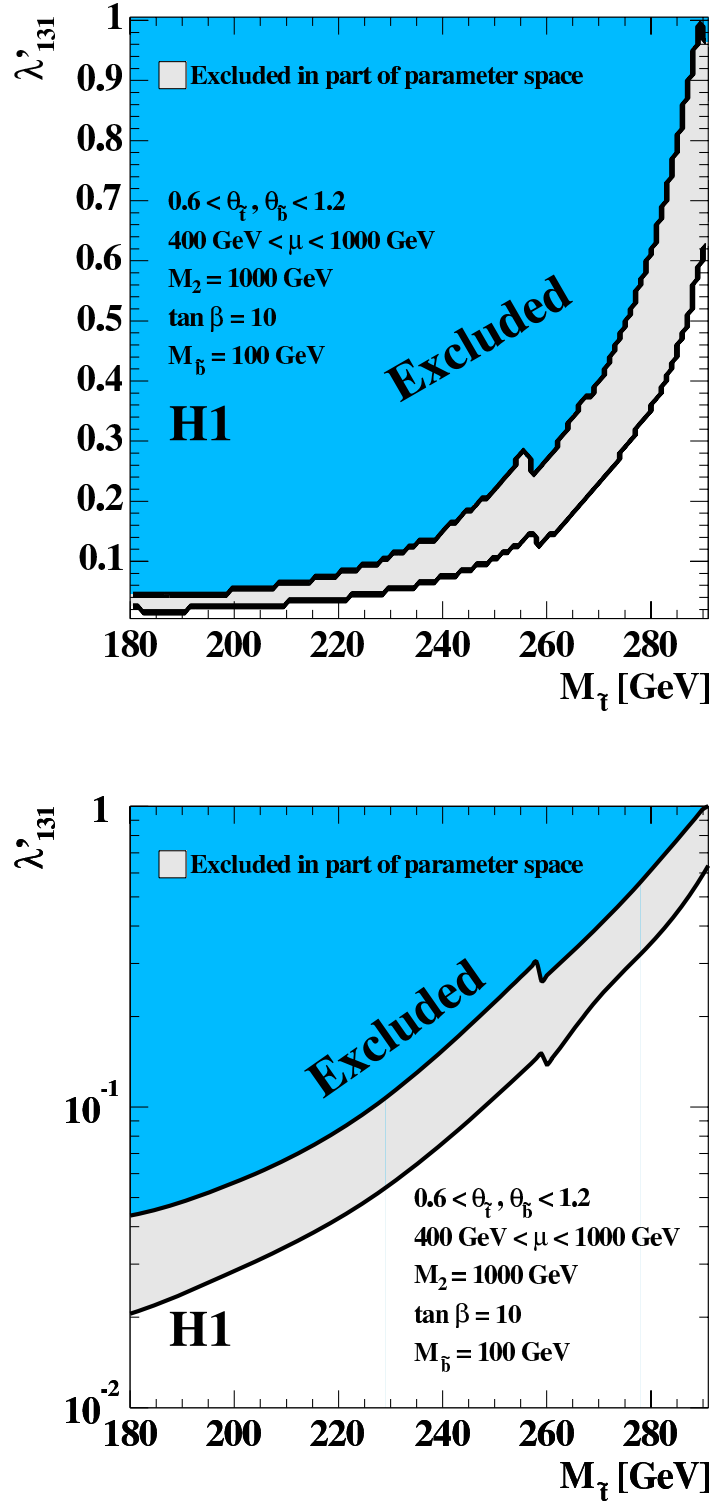
**Figure 6.6:** *The exclusion limits at $95\%$ CL on the $\not{R}_p$ coupling $\lambda'_{131}$ in linear scale (top) and logarithmic scale (bottom) as a function of the stop mass from a scan of the MSSM parameter space as indicated in the figure. The sbottom mass is set to $M_{\tilde{b}} = 100\,\text{GeV}$. The two full curves indicate the strongest and the weakest limits on $\lambda'_{131}$ in the parameter space investigated.*
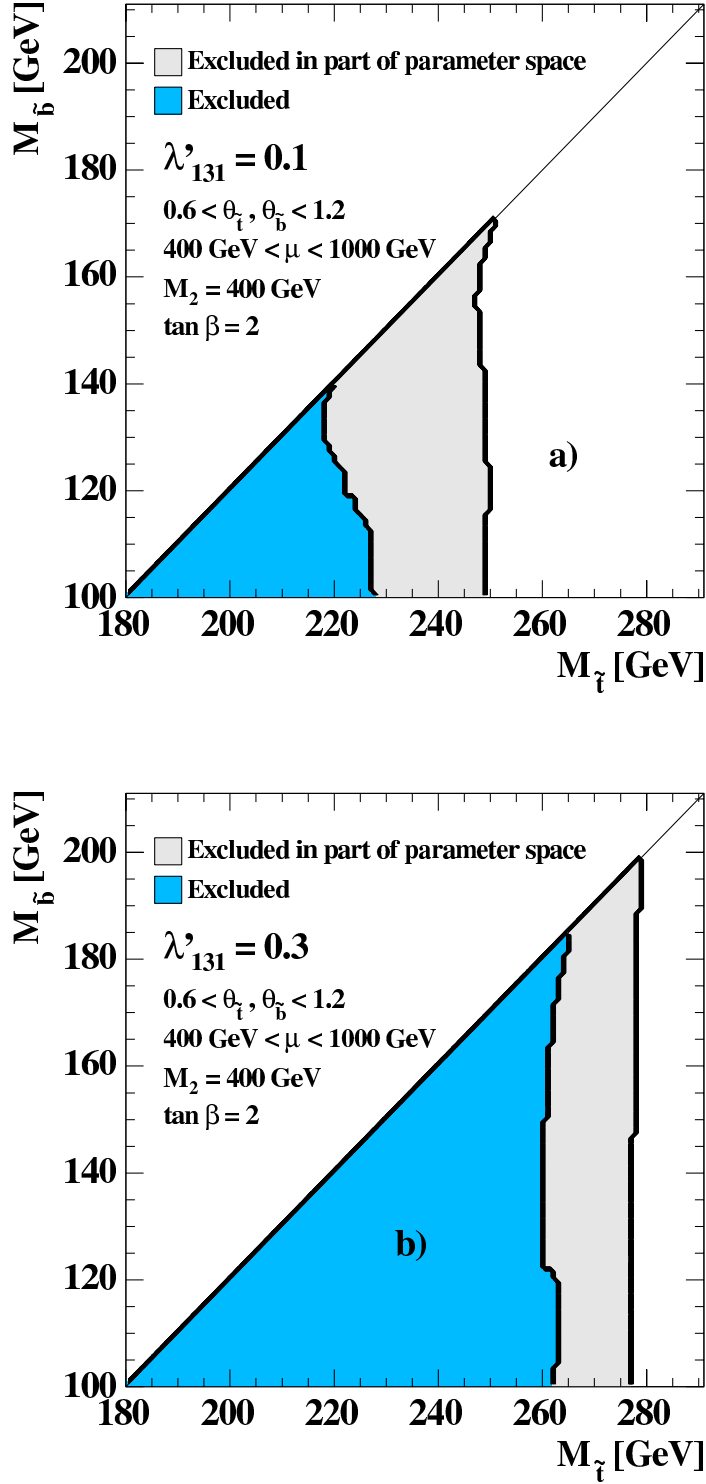
**Figure 6.7:** *The exclusion limits at* $95\%$ *CL in the* $(M_{\tilde{t}}, M_{\tilde{b}})$*–plane for a)* $\lambda'_{131} = 0.1$ *and b)* $\lambda'_{131} = 0.3$ *from a scan of the MSSM parameter space as indicated in the figures. The two full curves indicate the regions excluded in all or part of the SUSY parameter space investigated. Here, the parameters* $\tan\beta$ *and* $M_2$ *are set to* $\tan\beta = 2$ *and* $M_2 = 400$ *GeV.*
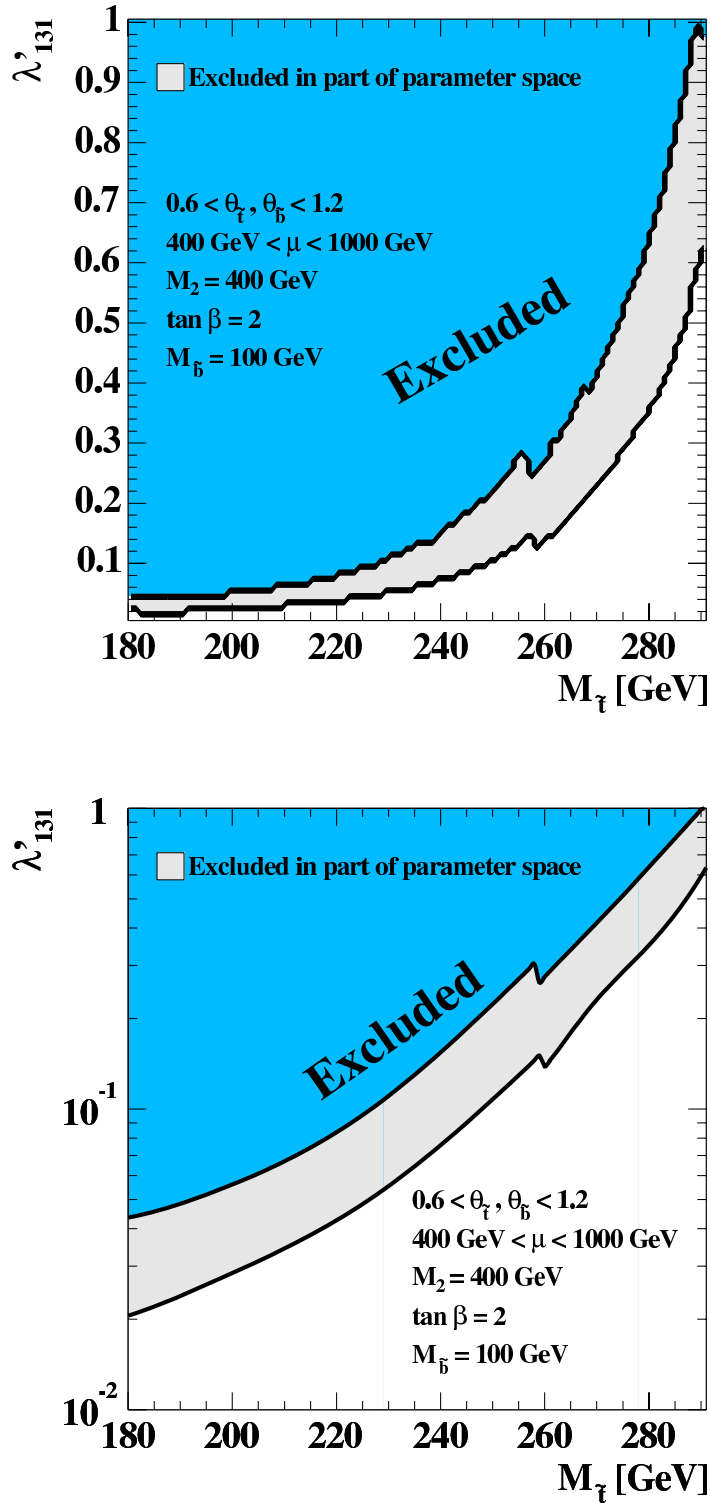
**Figure 6.8:** *The exclusion limits at $95\%$ CL on the $\not{R}_p$ coupling $\lambda'_{131}$ in linear scale (top) and logarithmic scale (bottom) as a function of the stop mass from a scan of the MSSM parameter space as indicated in the figure. The sbottom mass is set to $M_{\tilde{b}} = 100\,GeV$. The two full curves indicate the strongest and the weakest limits on $\lambda'_{131}$ in the parameter space investigated. Here, the parameters $\tan\beta$ and $M_2$ are set to $\tan\beta = 2$ and $M_2 = 400\,GeV$.*
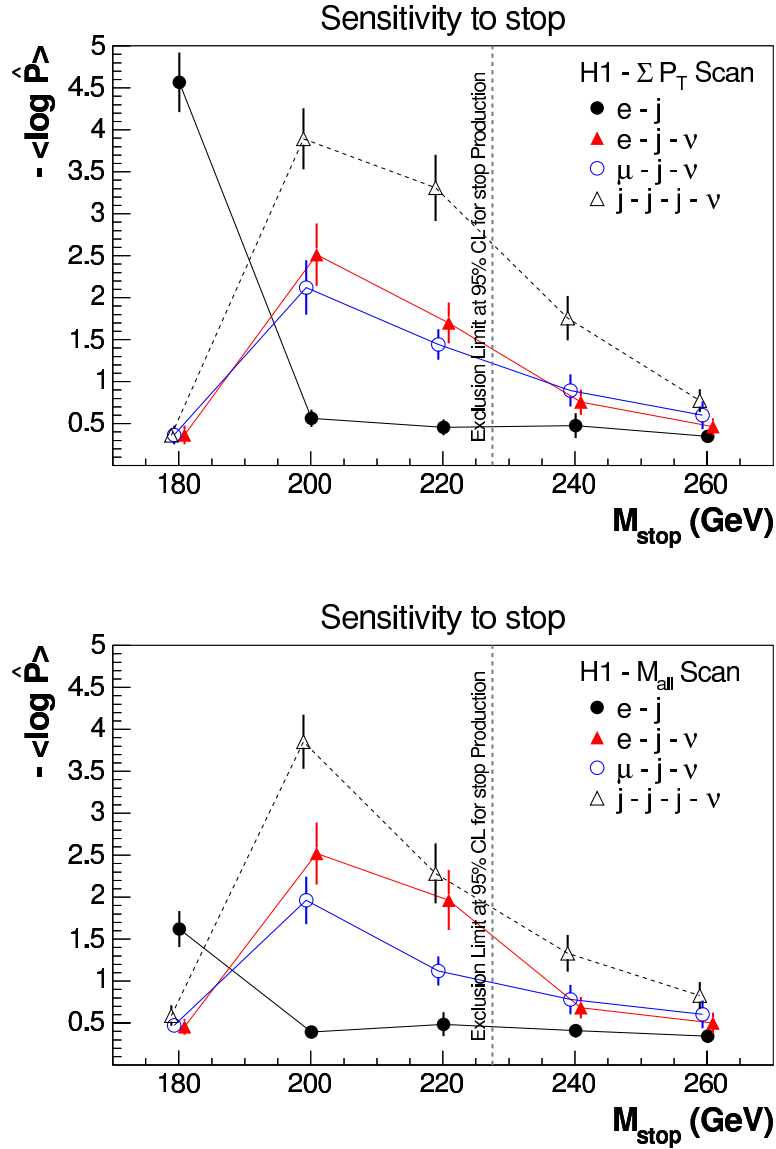
**Figure 6.9:** *The mean value of* $-\log \hat{P}$ *as a function of the stop mass. This variable is used in the general search for new phenomena in* $ep$ *scattering at HERA [52,71,70]. It is derived with MC experiments which include a stop signal with a mass* $M_{stop} \equiv M_{\tilde{t}}$*, and using the distributions of* $\sum P_T$ *(top) and* $M_{all}$ *(bottom). The* $\not{R}_p$ *coupling* $\lambda'_{131}$ *is set to* $0.1$ *and the sbottom mass is* $M_{\tilde{b}} = 100\,GeV$*. The plots are taken from [71]. The event classes* $e$*-*$j$*,* $e$*-*$j$*-*$\nu$*,* $\mu$*-*$j$*-*$\nu$ *and* $j$*-*$j$*-*$j$*-*$\nu$ *correspond to the* $ed$*,* $je\not{P}_\perp$ *,* $j\mu\not{P}_\perp$ *and* $jjj\not{P}_\perp$ *channels, respectively, of the present analysis.*

# 7
# Summary and Outlook

In this analysis, a search is performed for scalar top quarks resonantly produced in electron–proton scattering at HERA in $R$–parity violating supersymmetry. The most general Minimal Supersymmetric Standard Model is $R$–parity violating. This allows for the resonant production of supersymmetric particles at colliders. In particular, at HERA single squarks with masses up to the order of the centre–of–mass energy $\sqrt{s}$ can be produced in $e^{\pm}p$ collisions via the $R\!\!\!/_p$ Yukawa coupling $\lambda'$. The present analysis uses the $e^+p$ H1 data taken in the years 1994–2000 which correspond to a total integrated luminosity of about $106$ pb$^{-1}$.

The stop quarks which are produced resonantly in $e^+p$ collisions can decay bosonically into a sbottom quark and a $W$ boson, $\tilde{t} \to \tilde{b}W$. The subsequent $R\!\!\!/_p$ sbottom decay into SM particles, $\tilde{b} \to \bar{\nu}_e d$, and leptonic and hadronic $W$ decays are investigated. In addition, the direct $R\!\!\!/_p$ decay $\tilde{t} \to ed$ can occur. The $R$–parity conserving bosonic stop decays lead to three final state topologies considered in this analysis: the $je P\!\!\!/_\perp$ channel, the $j\mu P\!\!\!/_\perp$ channel and the $jjj P\!\!\!/_\perp$ channel. $R$–parity violating direct stop decays have topologies similar to those of NC DIS processes. The analysis is particularly interesting following the observation of events with isolated electrons or muons and missing transverse momentum at H1 [6] which have final state topologies similar to those of the $je P\!\!\!/_\perp$ or $j\mu P\!\!\!/_\perp$ channel.

In the $j\mu P\!\!\!/_\perp$ channel, a slight excess of events compared with the SM expectation is observed. Nevertheless, no evidence for stop production is found in the final state topologies under consideration, since the excess in the $j\mu P\!\!\!/_\perp$ channel is not supported by the other three channels analysed in the present thesis.

For the first time, direct constraints on stop quarks decaying bosonically are derived. Including the direct $R\!\!\!/_p$ stop decay, mass dependent limits on the coupling $\lambda'_{131}$ are obtained within the MSSM. For this purpose, the SUSY parameters $\mu$, $M_2$ and $\tan\beta$ which determine the gaugino masses are chosen such that fermionic squark decays via their usual gauge couplings into neutralinos, charginos or gluinos are kinematically forbidden. Moreover, a scan of the mixing angles

$\theta_{\tilde{t}}$ and $\theta_{\tilde{b}}$ is performed. In a large part of the MSSM parameter space, the existence of stop quarks coupling to an $e^+d$ pair with masses up to $275\,\mathrm{GeV}$ can be excluded at the $95\%$ CL for a strength of the Yukawa coupling of $\lambda'_{131} = \sqrt{4\pi\alpha_{em}} = 0.3$. Consistency checks show that the deduced exclusion limits are similar to those of previous analyses in squark production by H1 [5].

To give an outlook, the HERA collider has recently been upgraded in order to significantly increase the integrated luminosity of the HERA II data sample; the machine will operate until 2006/2007. The expected enhancement of statistics might be able to establish the slight excess in the $j\mu\not{P}_\perp$ channel, either it is caused by statistical fluctuations or it is a sign of new physics. Furthermore, the exclusion limits on stop production will be improved. In addition, at HERA II the electron beam is longitudinally polarised. Since in $e^+p$ scattering mainly up–type squarks can be produced, the longitudinal polarisation of right–handed positrons will increase the sensitivity to the production of stop quarks.

SUSY has not been discovered so far, but the search for supersymmetric particles will continue at the Large Hadron Collider (LHC). Moreover, the TESLA linear collider which might be build at DESY would be able to provide precise measurements of the properties of SUSY particles.

# List of Figures

# List of Tables

# Bibliography

[1] **Super–Kamiokande** Collaboration, Y. Fukuda *et. al.*,
*Evidence for oscillation of atmospheric neutrinos,*
*Phys. Rev. Lett.* **81** (1998) 1562–1567, [hep-ex/9807003]. 1

[2] **SNO** Collaboration, Q. R. Ahmad *et. al.*,
*Direct evidence for neutrino flavor transformation from neutral–current interactions in the Sudbury Neutrino Observatory,*
*Phys. Rev. Lett.* **89** (2002) 011301, [nucl-ex/0204008]. 1

[3] M. Hirsch, M. A. Diaz, W. Porod, J. C. Romao, and J. W. F. Valle,
*Neutrino masses and mixings from supersymmetry with bilinear $R$–parity violation: A theory for solar and atmospheric neutrino oscillations,*
*Phys. Rev.* **D62** (2000) 113008, [hep-ph/0004115]. 1

[4] **H1** Collaboration, C. Adloff *et. al.*,
*Searches at HERA for squarks in $R$–parity violating supersymmetry,*
*Eur. Phys. J.* **C20** (2001) 639–657, [hep-ex/0102050]. 2, 62

[5] **H1** Collaboration, A. Aktas *et. al.*,
*Search for squark production in $R$–parity violating supersymmetry at HERA,*
hep-ex/0403027. submitted to *Eur. Phys. J.* **C**. 2, 22, 55, 62, 79, 80, 94, 102, 106

[6] **H1** Collaboration, V. Andreev *et. al.*,
*Isolated electrons and muons in events with missing transverse momentum at HERA,*
*Phys. Lett.* **B561** (2003) 241–257, [hep-ex/0301030]. 2, 46, 61, 63, 67, 85, 101, 109

[7] T. Kon, T. Matsushita, and T. Kobayashi,
*Possible excess in charged current events with high–$Q^2$ at HERA from stop and sbottom production,*
*Mod. Phys. Lett.* **A12** (1997) 3143–3152, [hep-ph/9707355]. 2, 15, 21, 23, 29, 63

[8] C. Berger,
*Elementarteilchenphysik,*
Springer (2002).  3

[9] The LEP working group for Higgs boson searches
*Search for the standard model Higgs boson at LEP*
submitted to *Phys. Lett.* **B** (2003) CERN-EP/2003-011.  5

[10] **Particle Data Group** Collaboration, K. Hagiwara *et. al.,*
*Review of particle physics,*
*Phys. Rev.* **D66** (2002) 010001.  5

[11] R. P. Feynman,
*Very high–energy collisions of hadrons,*
*Phys. Rev. Lett.* **23** (1969) 1415–1417.  6

[12] H. Spiesberger *et. al.,*
*Radiative corrections at HERA,*
(1991). Contribution to Workshop on Physics at HERA, Hamburg, Germany.  7

[13] **H1** Collaboration, C. Adloff *et. al.,*
*Measurement and QCD analysis of neutral and charged current cross sections at HERA,*
*Eur. Phys. J.* **C30** (2003) 1–32, [hep-ex/0304003].  7, 42, 44, 53

[14] A. Arbuzov, D. Y. Bardin, J. Bluemlein, L. Kalinovskaya, and T. Riemann,
*HECTOR 1.00 - A program for the calculation of QED, QCD and electroweak corrections
to ep and lN deep inelastic neutral and charged current scattering,*
*Comput. Phys. Commun.* **94** (1996) 128–184, [hep-ph/9511434].  7

[15] U. Baur, J. A. M. Vermaseren, and D. Zeppenfeld,
*Electroweak vector boson production in high–energy e p collisions,*
*Nucl. Phys.* **B375** (1992) 3–44.  9, 28

[16] G. G. Ross,
*Grand Unified Theories,*
Benjamin & Cunnings (1985).  9

[17] S. P. Martin,
*A supersymmetry primer,*
(1997) [hep-ph/9709356].  10, 11, 14, 16

[18] S. Weinberg,
*Implications of dynamical symmetry breaking,*
*Phys. Rev.* **D13** (1976) 974–996.  10

[19] L. Susskind,
*Dynamics of spontaneous symmetry breaking in the Weinberg–Salam theory*,
*Phys. Rev.* **D20** (1979) 2619–2625. 10

[20] H. P. Nilles,
*Supersymmetry, supergravity and particle physics*,
*Phys. Rept.* **110** (1984) 1. 10

[21] H. E. Haber and G. L. Kane,
*The search for supersymmetry: probing physics beyond the Standard Model*,
*Phys. Rept.* **117** (1985) 75. 10

[22] E. Witten,
*Dynamical breaking of supersymmetry*,
*Nucl. Phys.* **B188** (1981) 513. 11

[23] J. Kalinowski and S. Pokorski,
*Higgs particle production at LEP in multidoublet scenarios with hierarchy of the vacuum expectation values*,
*Phys. Lett.* **B219** (1989) 116. 16, 91

[24] A. Bartl, W. Majerotto, and W. Porod,
*Squark and gluino decays for large* $\tan\beta$,
*Z. Phys.* **C64** (1994) 499–508. 16, 17

[25] C.-L. Chou and M. E. Peskin,
*Scalar top quark as the next–to–lightest supersymmetric particle*,
*Phys. Rev.* **D61** (2000) 055004, [hep-ph/9909536]. 16

[26] J. R. Ellis and S. Rudaz,
*Search for supersymmetry in toponium decays*,
*Phys. Lett.* **B128** (1983) 248. 16

[27] J. F. Gunion and H. E. Haber,
*Higgs bosons in supersymmetric models. 1*, *Nucl. Phys.* **B272** (1986) 1. 16

[28] Y. A. Golfand and E. P. Likhtman,
*Extension of the algebra of poincare group generators and violation of P invariance*,
*JETP Lett.* **13** (1971) 323–326. 18

[29] J. Wess and B. Zumino,
*Supergauge transformations in four–dimensions*,
*Nucl. Phys.* **B70** (1974) 39–50. 18

[30] G. Bhattacharyya and P. B. Pal,
*New constraints on R–parity violation from proton stability,*
*Phys. Lett.* **B439** (1998) 81–84, [hep-ph/9806214]. 18

[31] S. Weinberg,
*Supersymmetry at ordinary energies. 1. Masses and conservation laws,*
*Phys. Rev.* **D26** (1982) 287. 18

[32] R. Barbier *et. al.,*
*R-parity violating supersymmetry,* hep-ph/0406039. 18

[33] G. R. Farrar and P. Fayet,
*Phenomenology of the production, decay, and detection of new hadronic states associated with supersymmetry,*
*Phys. Lett.* **B76** (1978) 575–579. 19

[34] **H1** Collaboration, S. Aid *et. al.,*
*A search for selectrons and squarks at HERA,*
*Phys. Lett.* **B380** (1996) 461–470, [hep-ex/9605002]. 19

[35] **ZEUS** Collaboration, J. Breitweg *et. al.,*
*Search for selectron and squark production in e+ p collisions at HERA,*
*Phys. Lett.* **B434** (1998) 214–230, [hep-ex/9806019]. 19

[36] J. Butterworth and H. K. Dreiner,
*R–parity violation at HERA,*
*Nucl. Phys.* **B397** (1993) 3–34, [hep-ph/9211204]. 20

[37] **ALEPH** Collaboration, A. Heister *et. al.,*
*Search for supersymmetric particles with $R$–parity violating decays in $e^+e^-$ collisions at $\sqrt{s}$ up to 209 GeV,*
*Eur. Phys. J.* **C31** (2003) 1–16, [hep-ex/0210014]. 24, 87

[38] H. Jung,
*Hard diffractive scattering in high-energy e p collisions and the Monte Carlo generation RAPGAP,*
*Comp. Phys. Commun.* **86** (1995) 147–161. 28

[39] T. Sjostrand,
*A model for initial state parton showers,*
*Phys. Lett.* **B157** (1985) 321. 28

[40] A. Kwiatkowski, H. Spiesberger, and H. J. Mohring,

*HERACLES: An event generator for $ep$ interactions at HERA energies including radiative processes: version 1.0,*
Comp. Phys. Commun. **69** (1992) 155–172.  28

[41] **CTEQ** Collaboration, H. L. Lai *et. al.*,
*Global QCD analysis of parton structure of the nucleon: CTEQ5 parton distributions,*
Eur. Phys. J. **C12** (2000) 375–392, [`hep-ph/9903282`].  28

[42] G. A. Schuler and H. Spiesberger,
*DJANGO: The Interface for the event generators HERACLES and LEPTO,*
(1991). In *Hamburg, Proceedings, Physics at HERA, vol. 3* 1419-1432.
(see High Energy Physics Index 30 (1992) No. 12988).  28

[43] G. Gustafson and U. Pettersson,
*Dipole formulation of QCD cascades,*
Nucl. Phys. **B306** (1988) 746.  28

[44] L. Lonnblad,
*ARIADNE version 4: A Program for simulation of QCD cascades implementing the color dipole model,*
Comput. Phys. Commun. **71** (1992) 15–31.  28

[45] T. Sjostrand *et. al.*,
*High–energy–physics event generation with PYTHIA 6.1,*
Comput. Phys. Commun. **135** (2001) 238–259, [`hep-ph/0010017`].  28

[46] M. Gluck, E. Reya, and A. Vogt,
*Parton structure of the photon beyond the leading order,*
Phys. Rev. **D45** (1992) 3986–3994.  28

[47] K.-P. O. Diener, C. Schwanenberger, and M. Spira,
*Photoproduction of W bosons at HERA: QCD corrections,*
Eur. Phys. J. **C25** (2002) 405–411, [`hep-ph/0203269`].  28

[48] K.-P. O. Diener, C. Schwanenberger, and M. Spira,
*Photoproduction of W bosons at HERA: Reweighting method for implementing QCD corrections in Monte Carlo programs,*
(2003) [`hep-ex/0302040`].  28

[49] T. Abe,
*GRAPE–Dilepton (Version 1.1): A generator for dilepton production in e p collisions,*
Comput. Phys. Commun. **136** (2001) 126–147, [`hep-ph/0012029`].  28

[50] C. Berger and P. Kandel,
*Monte Carlo Generators for HERA Physics.*
Proceedings, Workshop, Hamburg, Germany.  29

[51] S. Kawabata,
*A new Monte Carlo event generator for high–energy physics,*
*Comput. Phys. Commun.* **41** (1986) 127.  29

[52] **H1** Collaboration, A. Aktas *et. al.*,
*General search for new phenomena in $ep$ scattering at HERA,*
(2004). to be submitted to *Phys. Lett.* **B.**  29, 41, 44, 47, 52, 54, 61, 94, 99, 107

[53] S. Caron,
*Jets in photoproduction at HERA.* PhD thesis.
RWTH Aachen, Germany, 2002, DESY-THESIS-2002-035,
also available at http://www-h1.desy.de/publications/thesis_list.html.  29, 46, 53

[54] S. Katsanevas and P. Morawitz,
*SUSYGEN 2.2: A Monte Carlo event generator for MSSM sparticle production at e+ e-colliders,*
*Comput. Phys. Commun.* **112** (1998) 227–269, [hep-ph/9711417].  29, 90

[55] N. Ghodbane,
*SUSYGEN 3: An event generator for linear colliders,*
(1999) [hep-ph/9909499].  29, 90

[56] V. N. Gribov and L. N. Lipatov,
*Deep inelastic e p scattering in perturbation theory,*
*Yad. Fiz.* **15** (1972) 781–807.  29

[57] T. Sjostrand,
*PYTHIA 5.7 and JETSET 7.4: Physics and manual,*
(1995) [hep-ph/9508391].  29

[58] J. R. Schneider, P. Soding, G. A. Voss, A. Wagner, and B. H. Wiik,
*The Deutsches Elektronen Synchrotron,*
*Europhys. News* **25** (1994) 91–105.  33

[59] **H1** Collaboration, I. Abt *et. al.*,
*The H1 detector at HERA,*
*Nucl. Instrum. Meth.* **A386** (1997) 310–347.  33, 34

[60] **ZEUS** Collaboration,
*The ZEUS detector: Status report 1993,*
(1993). ZEUS-STATUS-REPT-1993.  33

[61] **HERMES** Collaboration.
     http://www-hermes.desy.de.  33

[62] **HERA–B** Collaboration.
     http://www-hera-b.desy.de.  33

[63] **H1** Collaboration, I. Abt *et. al.*,
     *The Tracking, calorimeter and muon detectors of the H1 experiment at HERA*,
     *Nucl. Instrum. Meth.* **A386** (1997) 348–396.  34

[64] **H1 Calorimeter Group** Collaboration, B. Andrieu *et. al.*,
     *The H1 liquid argon calorimeter system*,
     *Nucl. Instrum. Meth.* **A336** (1993) 460–498.  34

[65] **H1 Calorimeter Group** Collaboration, B. Andrieu *et. al.*,
     *Results from pion calibration runs for the H1 liquid argon calorimeter and comparisons
     with simulations*,
     *Nucl. Instrum. Meth.* **A336** (1993) 499–509.  37

[66] **H1 Calorimeter Group** Collaboration, B. Andrieu *et. al.*,
     *Electron / pion separation with the H1 LAr calorimeters*,
     *Nucl. Instrum. Meth.* **A344** (1994) 492–506.  37

[67] **H1 Calorimeter Group** Collaboration, B. Andrieu *et. al.*,
     *Beam tests and calibration of the H1 liquid argon calorimeter with electrons*,
     *Nucl. Instrum. Meth.* **A350** (1994) 57–72.  37

[68] **H1** Collaboration,
     *Technical proposal to upgrade the backward scattering region of the H1 detector*,
     (1993). DESY-PRC-93-02.  38

[69] **H1 SPACAL Group** Collaboration, R. D. Appuhn *et. al.*,
     *The H1 lead/scintillating–fibre calorimeter*,
     *Nucl. Instrum. Meth.* **A386** (1997) 397–408.  38

[70] G. Frising,
     *Rare phenomena and $W$ production in electron–proton scattering at HERA*. PhD thesis.
     RWTH Aachen, Germany, 2003,
     also available at http://mozart.physik.rwth-aachen.de/Diplom-Doktor.html.  41, 44, 45,
     46, 47, 52, 61, 94, 99, 107

[71] M. Wessels,
     *General search for new phenomena in $ep$ scattering at HERA*. PhD thesis.
     RWTH Aachen Germany, 2004, (in preparation)

to be available at http://mozart.physik.rwth-aachen.de/Diplom-Doktor.html.  41, 44, 45, 53, 61, 94, 99, 107

[72] **H1** Collaboration,
*QBGFMAR: An updated PHAN package for cosmic and halo muon topological rejection in high $P_T$ physics analysis,*
(1998). H1 internal note-556.  42

[73] B. Leissner,
*Muon pair production in electron proton collisions.* PhD thesis.
RWTH Aachen, Germany, 2002, DESY-THESIS-2002-049,
also available at http://www-h1.desy.de/publications/thesis_list.html.  42, 45, 46

[74] M. Stoye,
*Untersuchung von Endzustanden mit mehreren Elektronen in der Elektron–Proton–Streuung,* Master's thesis.
RWTH Aachen, Germany, 2003,
also available at http://mozart.physik.rwth-aachen.de/Diplom-Doktor.html.  44

[75] U. Bassler,
*QESCAT − e identification software in H1PHAN,*
H1 internal software package.  44

[76] H. Albrecht, M. Erdmann, and P. Schleper,
*A guide to H1PHAN, an H1 physics analysis package,*
(1997). H1 internal software manual.  44

[77] P. Bruel,
*Recherche d'interactions au–delà du Modelè Standard à HERA.* PhD thesis.
Université Paris, France, 1998,
also available at http://www-h1.desy.de/publications/thesis_list.html.  44

[78] V. Blobel,
*The BOS System, Dynamic memory management,*
(1987). University of Hamburg.  44

[79] A. Aktas *et. al.,*
*The H1 OO physics analysis project,*
(2003). H1 internal software manual.  46

[80] S. D. Ellis and D. E. Soper,
*Successive combination jet algorithm for hadron collisions,*
*Phys. Rev.* **D48** (1993) 3160–3166, [hep-ph/9305266].  46

[81] S. Catani, Y. L. Dokshitzer, M. H. Seymour, and B. R. Webber,
*Longitudinally invariant K(t) clustering algorithms for hadron hadron collisions*,
*Nucl. Phys.* **B406** (1993) 187–224.  46

[82] A. Blondel and F. Jacquet,
*Detection of the charged current event–method II*,
Proceedings of the study of an $ep$ facility for europe,
ed. U. Amaldi, DESY report 79-48 (1979) 391.  49

[83] B. Heinemann,
*Measurement of charged current and neutral current cross sections in positron proton collisions at $\sqrt{s} \approx 300$ GeV*. PhD thesis.
University of Hamburg, Germany, 1999, DESY-THESIS-1999-046,
also available at http://www-h1.desy.de/publications/thesis_list.html.  49, 51, 52, 80

[84] J. Scheins,
*Suche nach Kontakt–Wechselwirkungen und Gravitoneffekten in der tief–inelastischen Streuung bei HERA*. PhD thesis.
RWTH Aachen, Germany, 2001,
also available at http://mozart.physik.rwth-aachen.de/Diplom-Doktor.html.  50

[85] **H1** Collaboration, C. Adloff *et. al.*,
*Diffraction dissociation in photoproduction at HERA*,
*Z. Phys.* **C74** (1997) 221–236, [hep-ex/9702003].  52

[86] J. Ebert *et. al.*,
*HFS – a software package to cope with the Hadronic Final State*,
H1 internal software package.  52

[87] **H1** Collaboration, A. Aktas *et. al.*,
*Muon pair production in e p collisions at HERA*,
*Phys. Lett.* **B583** (2004) 28–40, [hep-ex/0311015].  53, 54

[88] J. Rauschenberger,
*Prozesse des geladenen Stromes in tief–unelastischer Positron–Proton Streuung bei HERA.*
PhD thesis.
University of Hamburg, Germany (2002)
also available at http://www-h1.desy.de/publications/thesis_list.html.  53

[89] **H1** Collaboration, C. Adloff *et. al.*,
*Measurement of dijet cross sections in photoproduction at HERA*,
*Eur. Phys. J.* **C25** (2002) 13–23, [hep-ex/0201006].  54

[90] **H1** Collaboration, C. Adloff *et. al.*,
*Measurement of neutral and charged current cross–sections in positron proton collisions at large momentum transfer,*
*Eur. Phys. J.* **C13** (2000) 609–639, [hep-ex/9908059].  62

[91] J. Haller,
*Search for squark production in $R$–parity violating supersymmetry at HERA.* PhD thesis.
University of Heidelberg, Germany (2003)
DESY-THESIS-2003-035,
also available at http://www-h1.desy.de/publications/thesis_list.html.  80

[92] **H1** Collaboration, C. Adloff *et. al.*,
*Search for new physics in $e^{\pm}q$ contact interactions at HERA,*
*DESY-03-052, accepted by Phys. Lett.* **B** (2003) [hep-ex/0305015].  80

[93] **H1** Collaboration, A. Aktas *et. al.*,
*Search for single top quark production in e p collisions at HERA,*
*Eur. Phys. J.* **C33** (2004) 9–22, [hep-ex/0310032].  87

[94] T. Junk,
*Confidence level computation for combining searches with small statistics,*
*Nucl. Instrum. Meth.* **A434** (1999) 435–443, [hep-ex/9902006].  87, 89

[95] **DELPHI** Collaboration, P. Abreu *et. al.*,
*Search for spontaneous $R$–parity violation at $\sqrt{s} = 183$ GeV and $189$ GeV,*
*Phys. Lett.* **B502** (2001) 24–36, [hep-ex/0102045].  87

[96] **L3** Collaboration, P. Achard *et. al.*,
*Search for $R$–parity violating decays of supersymmetric particles in $e^{+}e^{-}$ collisions at LEP,*
*Phys. Lett.* **B524** (2002) 65–80, [hep-ex/0110057].  87

[97] **OPAL** Collaboration, G. Abbiendi *et. al.*,
*Search for $R$–parity violating decays of scalar fermions at LEP,*
*Eur. Phys. J.* **C33** (2004) 149–172, [hep-ex/0310054].  87

[98] E. Gross and A. Klier,
*Higgs statistics for pedestrians,*
(2002) [hep-ex/0211058].  88, 89, 106

[99] T. Junk,
*A fast probability sum for the likelihood ratio method of combining search limits*
http://thomasj.home.cern.ch/thomasj/searchlimits/ecl.html.  89

# Acknowledgements

I would like to thank all those I was working with and who supported me during my research time in Hamburg.

My special thanks go to my supervisor Prof. Dr. Christoph Berger for the possibility to work on this thesis at the H1 collaboration and for his advice and interest.

I want to thank Prof. Dr. Wolfgang Braunschweig for acting as second referee of this thesis.

I am thankful to Dr. Hans-Ulrich Martyn for his guidance throughout this analysis and for his enthusiasm and patience in many discussions. In addition, I am grateful to him for being my co–editor and supporting me during the publication procedure of this analysis.

Furthermore, I would like to thank:

Emmanuelle Perez for her help and the useful input she gave to establish this analysis.

Gilles Frising and Martin Wessels for their great collaboration and assistance regarding the technical aspects of the analysis.

Thomas Kluge, Christiane Risler and Carsten Krauss for proofreading this thesis.

Carlo Duprel, Boris Leißner, Sascha Caron, Jürgen Scheins, Thomas Kluge, Markus Hamann, Adil Aktas and Andrew Mehta for helpful discussions and tips.

All colleagues of the H1 collaboration for the friendly atmosphere and for operating and maintaining the H1 detector.

Kathrin, Nicole, Janna, Jana, Moni, Verena, Uta, Heike, Dagmar, Sandra, Anne, Michi, Corinna, Heike, Katharina, Petra, Wicki, Uli, Carsten and Kai for being a great team. I enjoyed the funny times we had in the diverse gyms of Hamburg.

Jens Pucknat for his patience and for the good times we enjoyed together.

My family for supporting me all the time.

# Curriculum Vitae

## Persönliche Daten

| | |
|---|---|
| **Name** | Anja Vest |
| **Geburtsdatum** | 15.09.1974 |
| **Geburtsort** | Mönchengladbach |
| **Nationalität** | deutsch |

## Bildungsweg

| | |
|---|---|
| 08.1980 – 06.1984 | Kath. Grundschule St. Anna, Mönchengladbach |
| 08.1984 – 06.1993 | Gymnasium Am Geroweiher, Mönchengladbach |
| 06.1993 | Abitur |
| 10.1993 – 01.2001 | Studium der Physik an der RWTH Aachen |
| 09.1997 – 07.1998 | Studium der Physik an der Università di Trieste, Italien |
| 10.1999 – 11.2000 | Anfertigung der Diplomarbeit bei Prof. Dr. Berger am I. Physikalischen Institut der RWTH Aachen |
| 11.2000 | Abgabe der Diplomarbeit mit dem Titel „Simulation der Graviton–Produktion am Next Linear Collider " |
| 11.01.2001 | Diplom in Physik |
| 05.2001 – 07.2004 | Promotion bei Prof. Dr. Berger am I. Physikalischen Institut der RWTH Aachen im Rahmen der H1 Kollaboration am DESY, Hamburg |
| 05.2004 | Abgabe der Dissertation mit dem Titel „Search for bosonic stop decays in $R$–parity violating supersymmetry in $e^+p$ collisions at HERA " |
| 29.07.2004 | Ablegung der mündlichen Prüfung und Abschluss der Promotion |